San Jose State University
SJSU ScholarWorks

Master's Theses | Master's Theses and Graduate Research

1997

Interdiffusion in copper nickel bilayers

Tim Westmore
San Jose State University

Follow this and additional works at: https://scholarworks.sjsu.edu/etd_theses

Recommended Citation
Westmore, Tim, "Interdiffusion in copper nickel bilayers" (1997). *Master's Theses*. 1532.
DOI: https://doi.org/10.31979/etd.hebg-se7e
https://scholarworks.sjsu.edu/etd_theses/1532

This Thesis is brought to you for free and open access by the Master's Theses and Graduate Research at SJSU ScholarWorks. It has been accepted for inclusion in Master's Theses by an authorized administrator of SJSU ScholarWorks. For more information, please contact scholarworks@sjsu.edu.

INFORMATION TO USERS

This manuscript has been reproduced from the microfilm master. UMI films the text directly from the original or copy submitted. Thus, some thesis and dissertation copies are in typewriter face, while others may be from any type of computer printer.

The quality of this reproduction is dependent upon the quality of the copy submitted. Broken or indistinct print, colored or poor quality illustrations and photographs, print bleedthrough, substandard margins, and improper alignment can adversely affect reproduction.

In the unlikely event that the author did not send UMI a complete manuscript and there are missing pages, these will be noted. Also, if unauthorized copyright material had to be removed, a note will indicate the deletion.

Oversize materials (e.g., maps, drawings, charts) are reproduced by sectioning the original, beginning at the upper left-hand corner and continuing from left to right in equal sections with small overlaps. Each original is also photographed in one exposure and is included in reduced form at the back of the book.

Photographs included in the original manuscript have been reproduced xerographically in this copy. Higher quality 6" x 9" black and white photographic prints are available for any photographs or illustrations appearing in this copy for an additional charge. Contact UMI directly to order.

UMI

A Bell & Howell Information Company
300 North Zeeb Road, Ann Arbor MI 48106-1346 USA
313/761-4700 800/521-0600

INTERDIFFUSION IN COPPER NICKEL BILAYERS

A Thesis

Presented to

The Faculty of the Department of Materials Engineering

San Jose State University

In Partial Fulfillment

of the Requirement for the Degree

Master of Science

by

Tim Westmore

August 1997

UMI Number: 1386233

Copyright 1997 by
Westmore, Tim

All rights reserved.

UMI Microform 1386233
Copyright 1997, by UMI Company. All rights reserved.

This microform edition is protected against unauthorized
copying under Title 17, United States Code.

UMI
300 North Zeeb Road
Ann Arbor, MI 48103

© 1997

Tim Westmore

ALL RIGHTS RESERVED

APPROVED FOR THE DEPARTMENT OF MATERIALS ENGINEERING

Dr. Emily L. Allen

Dr. John E.E. Baglin

Dr. Peter Gwozdz

APPROVED FOR THE UNIVERSITY

ABSTRACT

INTERDIFFUSION IN COPPER NICKEL BILAYERS

by Tim Westmore

Magnetic sensors contain layers of permalloy and copper. The films each have a thickness of less than 100 nm and the magnetic response of the structures depends critically on avoiding contamination from diffusion. This thesis is an investigation on interdiffusion in copper nickel bilayers. Measurements, by Rutherford Backscattering Spectrometry (RBS), Auger Electron Spectroscopy (AES), and X-Ray Diffraction (XRD), show that mass transport does take place at temperatures of 225 °C to 400 °C.

The observed diffusion along short circuit paths is much faster than in previous reports of grain boundary diffusion by other researchers. An explanation for this anomaly is the possible differences in internal structure of the polycrystalline films (dislocation density, grain boundary volume, porosity). In addition, the rates of copper transport into nickel grains far exceed expectations. Along with the peaks for copper and nickel, the diffraction patterns reveal a third alloy peak. It is a consequence of lattice diffusion and is evident when the heat treatment temperature is at 350 °C and 400 °C.

ACKNOWLEDGMENTS

Many people have provided both assistance and support during this thesis; each of their different contributions made it possible to complete this work. The author wishes to express great appreciation and gratitude to Emily Allen, Vaughn Deline, Andrew Kellock, Peter Gwozdz, Joyce Lawrence, Dolores Miller, Manfredo Tabacniks, Mike Toney, and Charles Wade. The author also extends great appreciation to his family for their patience and understanding. A special acknowledgment goes to John Baglin whose invaluable guidance and knowledge made this thesis possible. Funding for part of this work came from the National Science Foundation and the IBM Almaden Research Center.

CONTENTS

TITLE i

COPYRIGHT ii

SIGNATURES iii

ABSTRACT iv

ACKNOWLEDGMENTS v

CONTENTS vi

LIST OF TABLES viii

LIST OF FIGURES ix

1.0 INTRODUCTION 1
- 1.1 Application 1
- 1.2 Purpose 4
- 1.3 Objective 6
- 1.4 Figures 7

2.0 PREVIOUS WORK 10
- 2.1 Diffusion 10
- 2.2 Thin Film Diffusion 15
- 2.3 Copper and Nickel Diffusion 16
- 2.4 Figures 22

3.0 EXPERIMENT 24
- 3.1 Outline 24
- 3.2 Thin Film Deposition 25
  - 3.2.1 Pre-Deposition Clean
  - 3.2.2 Deposition
- 3.3 Heat Treatment 27
- 3.4 Rutherford Backscattering Spectrometry 29
- 3.5 RBS Simulations 30
- 3.6 Auger Electron Spectroscopy 36
- 3.7 X-Ray Diffraction 39
- 3.8 Figures 40

4.0 RESULTS 49
- 4.1 Physical Observations 49
- 4.2 RBS Measurements 50
  - 4.2.1 Copper on Nickel Structure
  - 4.2.2 Nickel on Copper Structure
  - 4.2.3 Contamination
  - 4.2.4 Summary of RBS Measurements
- 4.3 Auger Electron Spectroscopy 56

4.3.1 Surface Survey
4.3.2 Depth Profile
4.3.3 Summary of AES Measurements
4.4 X-Ray Diffraction 59
4.4.1 Copper on Nickel Structure
4.4.2 Nickel on Copper Structure
4.4.3 Summary of XRD Measurements
4.5 Figures 66
5.0 DISCUSSION 89
5.1 Qualitative Description of Results 89
5.1.1 Mass Transport
5.1.2 X-Ray Diffraction
5.2 Diffusion Models 94
5.2.1 Grain Boundary Volume Fraction
5.2.2 Diffusion into a Sphere
5.3 Quantitative Discussion 98
5.3.1 Grain Boundary Diffusion
5.3.2 Diffusion in the Lattice
5.3.3 Activation Energy
5.4 Applicaton to Head Structures 105
5.5 Sources of Error 107
5.5.1 Removal of AES Copper Overlap
5.5.2 RBS Simulations
5.6 Figures 110
6.0 CONCLUSIONS 117
7.0 REFERENCES 119
APPENDIX I: RUTHERFORD BACKSCATTERING SPECTROMETRY 121
APPENDIX II: AUGER ELECTRON SPECTROSCOPY 131
APPENDIX III: X-RAY DIFFRACTION 141

LIST OF TABLES

1 Lattice Diffusion for Copper and Nickel in Single Crystals
2 Grain Boundary Diffusion for Copper and Nickel Thin Films
3 Permeation Distances for Nickel Diffusion in Copper
4 Thin Film Deposition Conditions
5 Heat Treatment Time Temperature Matrix
6 Typical Conditions for RBS Measurements
7 Typical Conditions for AES Surface Surveys
8 Typical Conditions for AES Depth Profiles
9 Element Energy Window Scans for AES Depth Profiling
10 RBS Simulation Estimates for Diffusion Concentrations, Copper on Nickel
11 RBS Simulation Estimates for Diffusion Concentrations, Nickel on Copper
12 Diffusing Element Concentrations from AES, Copper on Nickel Structure
13 As Deposit Copper Peak Identification for Copper on Nickel
14 As Deposit Nickel Peak Identification for Copper on Nickel
15 XRD Changes with Heat Treatment, (111) Copper, Copper on Nickel Structure
16 XRD Changes with Heat Treatment, (111) Nickel, Copper on Nickel Structure
17 As Deposit Copper Peak Identification for Nickel on Copper
18 As Deposit Nickel Peak Identification for Nickel on Copper
19 XRD Changes with Heat Treatment, (111) Copper, Nickel on Copper Structure
20 XRD Changes with Heat Treatment, (111) Nickel, Nickel on Copper Structure

LIST OF FIGURES

1 Disk Drive Components
2 Thin Film Structure of Recording Disk Media
3 Thin Film Structure of a Giant Magnetoresistive Head
4 Schematic of Diffusion Kinetic Regimes
5 Auger Transition Energies for Copper
6 Auger Transition Energies for Nickel
7 Schematic of Thin Film Structures
8 Schematic of Heat Treatment Furnace
9 RBS Simulation of a Copper on Nickel Thin Film Structure
10 RBS Simulation of a Nickel on Copper Thin Film Structure
11 RBS Simulation of Equal Mass Transport in Copper on Nickel Films
12 RBS Simulation of Equal Mass Transport in Nickel on Copper Films
13 RBS Simulation of Inhomogeneous Concentrations in Copper on Nickel Films
14 RBS Simulation of Inhomogeneous Concentrations in Nickel on Copper Films
15 RBS Simulation of Unequal Mass Transport in Copper on Nickel Films
16 RBS Measurement of Thickness Variation Across a Sample
17 RBS Measurement Showing Yield Increase for Copper on Nickel
18 RBS Measurement Showing Inhomogeneous Diffusion of Copper into Nickel
19 RBS Simulation of Measurement for Copper on Nickel, 225 °C
20 RBS Simulation of Measurement for Copper on Nickel, 400 °C
21 RBS Simulation Structure for Figure 20
22 Diffusant Concentrations from RBS Simulations, Copper on Nickel Structure
23 RBS Measurement Showing Yield Decrease for Nickel on Copper
24 RBS Simulation of Measurement for Nickel on Copper, 225 °C
25 RBS Simulation of Measurement for Nickel on Copper, 400 °C
26 RBS Simulation Structure for Figure 25
27 Diffusant Concentrations from RBS Simulations of Nickel on Copper
28 AES Surface Surveys for Copper Nickel Bilayers Post Deposition

29 AES Overlay for Nickel on Copper Before and After Heat Treatment
30 AES Overlay for Copper on Nickel Before and After Heat Treatment
31 AES Depth Profile for 225 °C Heat Treatment
32 AES Depth Profile for 400 °C Heat Treatment
33 Nickel Concentration from AES Measurements for Nickel into Copper
34 Copper Concentration from AES Measurements for Copper into Nickel
35 X-Ray Diffraction Patterns of Post Deposition Samples
36 XRD Pattern Overlay for 8 Hour Heat Treatments, Copper on Nickel
37 XRD Pattern Overlay for 8 Hour Heat Treatments, Nickel on Copper
38 AES Concentration Profiles for 8 Hour Heat Treatments
39 RBS Overlay Measurement Spectra for 250 °C Heat Treatments
40 RBS Overlay Measurement Spectra for Different Times and Temperatures
41 RBS Overlay Measurement Spectra for 225 °C Heat Treatments
42 XRD Grain Size Changes with Temperature
43 Schematic of Grain Structure
44 Lattice Diffusion Saturation

1.0 INTRODUCTION

1.1 APPLICATION

In the disk drive technology there are several important components that include the storage disk and the recording head (Figure 1). Disks consist of sputtered films on a rigid substrate (aluminum or glass) and have a magnetic layer that is capable of storing digital information (Figure 2). There are also multiple thin films in a recording structure (Figure 3). Magnetic layers of a merged recording head permit the writing to and reading from a disk. This process takes place by changing or sensing the magnetization of the disk's magnetic layer. For the thin film structures in both the disk and head, the structure property relationships govern their performance and reliability

Among the materials in use for magnetic recording sensors are copper, iron, nickel, cobalt, tantalum, and manganese [1, 2, 3]. A sensor structure consists of thin films of these elements, made using either sputtering or evaporation deposition methods. Individual layers are either single element, binary, or ternary metal films and are normally polycrystalline. Temperatures may exceed 200 °C during post deposition processing steps such as photoresist curing. High current densities, that occur during device operation, could also create large temperature gradients or cause electromigration.

Any thin film is susceptible to low temperature diffusion because of its high density of defects [4]. Diffusion occurs primarily due to vacancies, dislocations, and/or grain boundaries. For thin films at low temperatures, short circuit diffusion paths (grain boundaries, dislocations) will dominate atomic movement because they are faster

(favorable energetically) than vacancy diffusion mechanisms. If fast path diffusion does take place, during processing and/or operation, it may lead to a degradation in performance of the thin film structure.

If lattice diffusion takes place between two films the lattice parameters will likely also change. The differences in atomic size, lattice size, and/or crystal structure will cause changes in the cell dimensions that may lead to inhomogeneous stress. Stress, in turn, may enable field assisted diffusion or result in loss of adhesion between the film and adjacent layers or substrate.

Huang [5] describes the changes in magnetoresistance of a spin-valve structure that includes copper and permalloy ($Ni_{80}Fe_{20}$). Magnetoresistance is a measure of the relative change in resistance (or resistivity) with the magnetization of the permalloy layer. Specular reflections of x-rays can examine the changes at boundaries between layers. Using this x-ray technique, and appropriate models, it was possible to measure the width of interface regions in multiple layer structures [5]. The authors report a large decrease in magnetoresistance that coincides with apparent intermixing between the copper and permalloy layers. The interfacial mixing, seen as an increase in its width, occurs at annealing temperatures of greater than 200 °C.

Shih [6] reports on interdiffusion in a copper nickel thin film couple. Rutherford Backscattering Spectrometry (RBS) measurements show atomic movement between the layers occurs at temperatures as low as 150 °C. There is an increase in the electrical resistivity of the copper nickel structure after annealing at 300 °C and above. The authors

attribute this change to atomic movement of nickel into copper seen in the back scatter spectra. Copper nickel has a high coefficient of resistivity with the atomic percentage of nickel.

The equilibrium phase diagram [7] for copper nickel shows complete solubility at all ranges of composition. However, existing data on lattice diffusion does not suggest that reactions in the above systems will occur at temperatures as low as 150 °C (Section 2.0). The defect volume to total volume ratio is much higher in thin films than for bulk materials. This suggests that short circuit diffusion mechanisms play an increasingly important role for thin films at low temperatures. This paper focuses on a particular system to investigate fast path diffusion mechanisms.

1.2 PURPOSE

The improvements that take place in magnetic storage include higher recording densities and/or faster recording speeds. Evaluation of existing and new technology is an important activity to keep up with enhancements or to advance development. It is always necessary to understand the ability of the current technology to survive severe applications. Important performance issues include functionality and reliability.

The metal layers currently in use for recording heads each have a thickness of less than 10 nm [8]. Therefore, they are vulnerable to contamination arising from slight amounts of interdiffusion. Designing sensors for a higher recording density will require even thinner films. Quantitative predictions of the diffusion kinetics and of the interactions in the thin film structure will provide insight about possible windows of processing and operation. It can also help to determine if there is a need to develop a separate structure for a more rigorous application.

For a magnetic recording structure consisting of permalloy (iron-nickel) and copper films, a stable boundary between the two may extend the possible operating region. Greater permissible operating temperatures will permit higher current densities for greater speeds and recording densities. However, interactions between the different layers can reduce the performance or reliability of the magnetic permalloy layer Such processes may include grain boundary diffusion at processing or operating temperatures, roughening between the layers, or reactions that result in the nucleation of another phase.

Many workers [2, 5, 9] investigating the impact of elevated temperatures on sensor structures have found a decrease in the magnetoresistance criterion. Their measurements attribute this to a roughening of the interface layers between the permalloy and copper films. Diffusion is a probable cause of the roughening since the interface thickness increases with heat treatment temperature, in the range of 200 °C to 400 °C. A quantitative understanding of the mass transport that occurs in this temperature range is necessary.

1.3 OBJECTIVE

This work is part of a larger investigation into the reactions within a complete magnetic recording structure. Such structures contain several different layers including binary and ternary films. The reactions that take place in the whole system, at elevated temperatures, are complex. It is also possible that some reactions will influence others, stimulate another process that would not otherwise occur, or even inhibit reactions.

As a prerequisite to investigating the copper and permalloy (ternary) structure, it is first necessary to explore the constituent binary systems. There are three binary configurations possible: copper and nickel; copper and iron; and nickel and iron. The experiments in this work will help to determine the interactions that take place in a copper and nickel thin film couple. The objective is to characterize any atomic movements, that occur during heat treatment, and attempt to resolve any reactions. The overall goal is to model the reactions and to determine acceptable processing and operating conditions.

This work used RBS, Auger Electron Spectroscopy (AES), and X-Ray Diffraction (XRD). The three techniques complement each other by providing both independent and supporting results. AES and RBS determine the distributions of copper and nickel in the films. Comparing the RBS measurements with those from AES supports interpretations of the results from both techniques. XRD provides data on grain size and phase; neither RBS nor AES is capable of measuring grain size nor providing an absolute determination of phase.

1.4 FIGURES

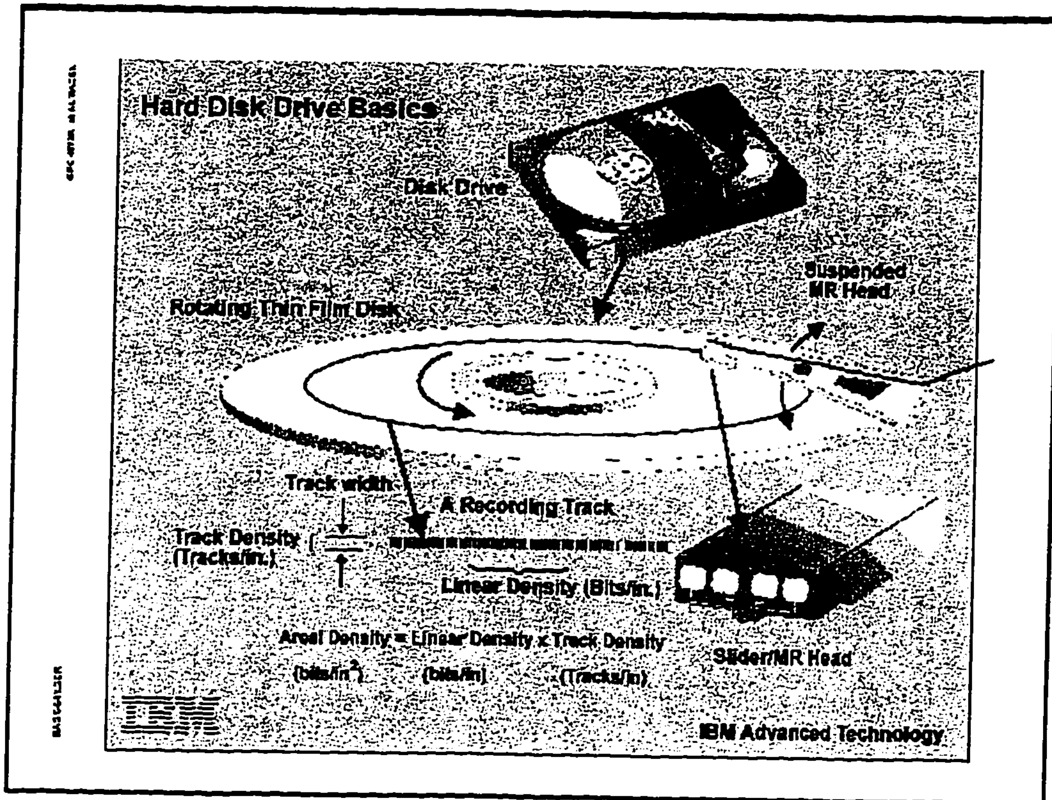

Figure 1: Disk Drive Components

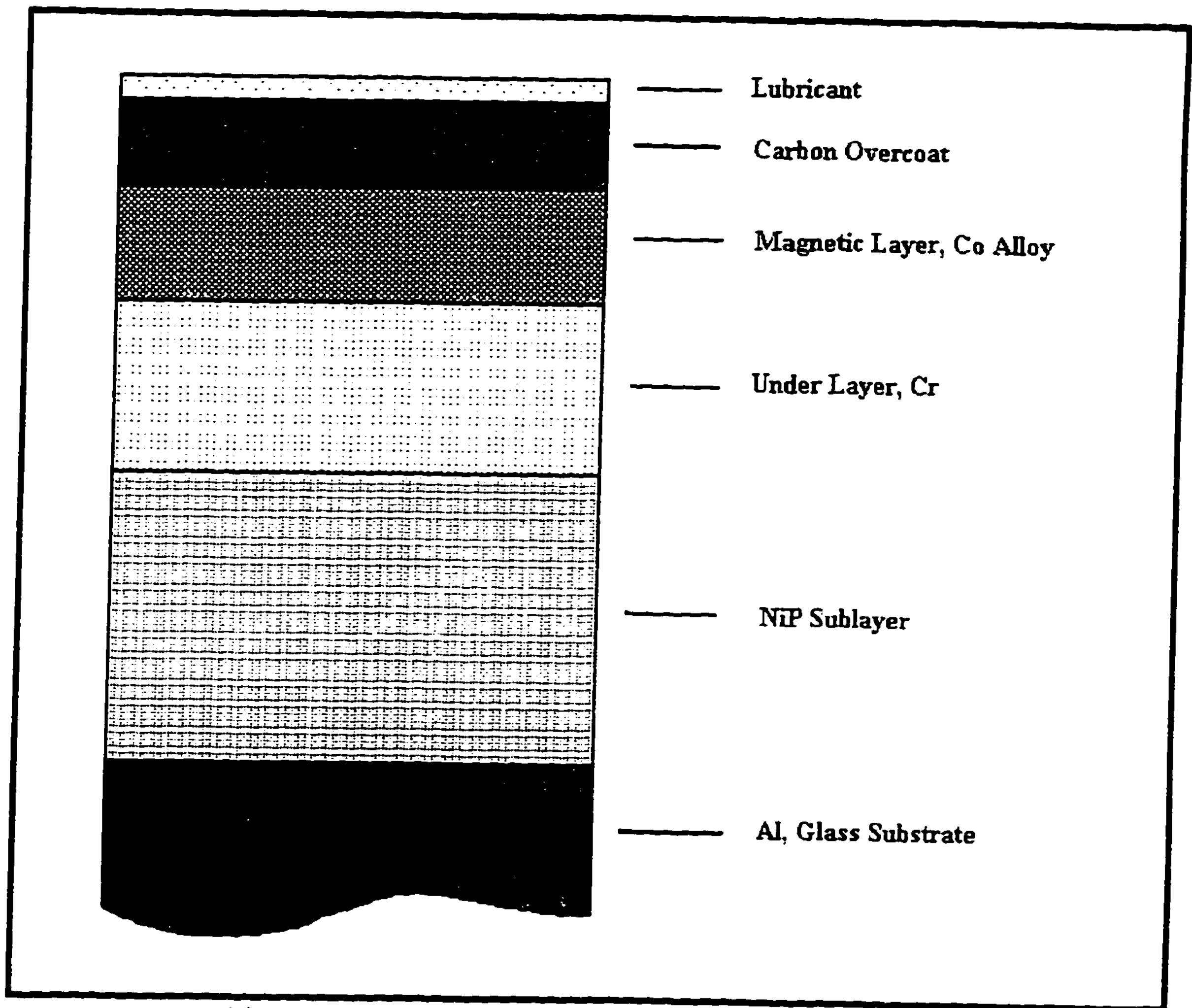

Figure 2: Thin Film Structure of Recording Disk Media

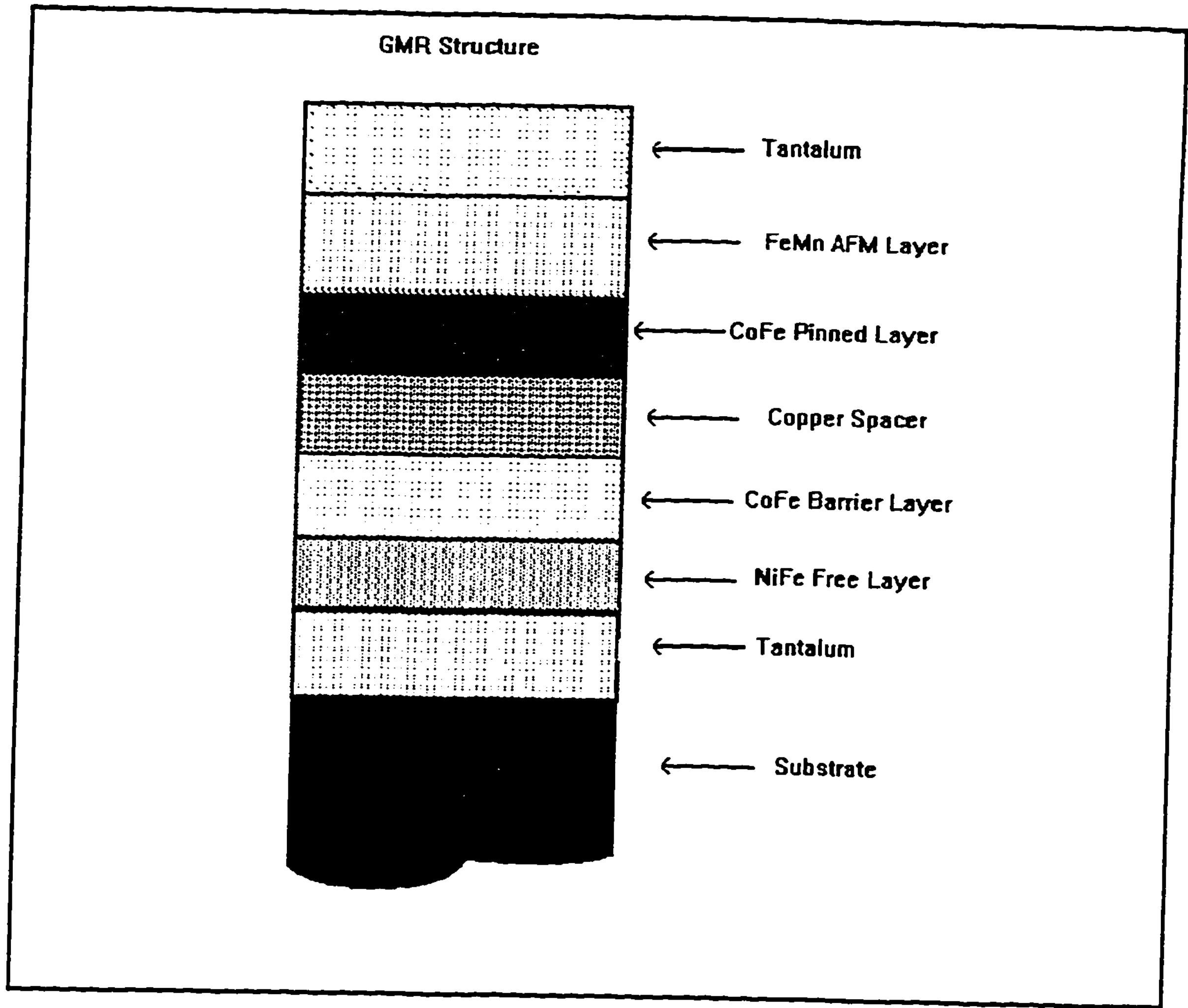

Figure 3: Thin Film Structure of a Giant Magnetoresistive Head

2.0 PREVIOUS WORK

2.1 DIFFUSION

Diffusion is a phenomenon where mass transport occurs at the atomic level. One result is a homogeneous distribution of a solute element throughout the matrix of its solvent. An everyday example of diffusion is a drop of ink in a glass of clear water. Initially, the ink drop has a distinct boundary and within it is dark and concentrated. The water is clear everywhere else except for the ink drop. Eventually, as a result of Brownian-like motion, the ink molecules evenly disperse throughout the water. The ink no longer has a distinct boundary and the water has taken on a darker color. As a representation of a low ink concentration, the final color of the water is much lighter than the original ink drop. Although this description of mass transport is for a liquid system, diffusion does take place in the solid state.

In polycrystalline materials, grain growth may occur as a result of mass transport when atoms from smaller grains move to a larger grain. Many other reactions also occur through diffusion: with the formation of a new phase, atomic transport facilitates both nucleation and growth. Atoms travel to the point of coalescence to permit reaching a critical nucleus size. After nucleation, atoms again travel to the edges of the new phase and allow the crystallite growth to continue.

In the lattice of a single crystal or within an individual grain, diffusion will occur by position exchange mechanisms such as between atoms. There are a number of possible mechanisms, although not all are energetically favorable. It is difficult for an atom to

squeeze between atoms on neighboring lattice points. An atom from one lattice point may move to an interstitial position. Diffusion may then take place by jumps from one interstitial site to another. If the crystal contains vacancies a favorable process is an exchange between an atom and a vacancy. Polycrystalline materials contain other defects such as dislocations and grain boundaries. These defects promote diffusion and migration along the grain boundaries is the fastest. The atom-vacancy exchange mechanism produces the slowest diffusion while the rate along dislocations is intermediate [10]

There is a necessary driving force to induce diffusion, the most common being a chemical potential gradient. This typically occurs as an abrupt or small variation in composition. Non-equilibrium concentrations of defects can also provide the motive for diffusion. Other stimuli include electromigration and stress; both are particularly apparent in thin films. The relative current densities in metallic thin films, for integrated circuit applications, can exceed 10^6 A/cm^2 [11]. Electrons can impart momentum onto atoms causing a form of field assisted diffusion. Stress, in thin films or bulk materials, can manifest itself as creep.

In metallic solids there are a number of pre-conditions for a vacancy exchange mechanism to occur. One requisite is the presence of vacancies in the material and another is the ability for both the vacancy and the atom to move around neighboring atoms. The first requirement means that the solid is at a temperature greater than absolute zero; all real world metals contain vacancies as a result of thermal energy. The second requisite means that a source of energy must exist to help atoms "push" their way between lattice

positions from one lattice or interstitial point to another. The energy requirement for a vacancy exchange is not as demanding as for an atom-with-atom exchange mechanism and the source may occur as thermal energy (lattice vibrations). At or above certain temperatures there is sufficient energy to aid atomic movement. Below this temperature the number of atoms possessing enough energy to make an exchange is very low. As a result, diffusion from such a mechanism is very slow or non-existent. The activity necessary for diffusion to ensue is its activation energy; diffusion is a thermally activated process.

For mass transport along dislocations and grain boundaries, the activation energy is less than that for the vacancy exchange mechanism. Dislocations and grain boundaries are regions within a material where the atomic packing is less dense. Thus, there is less obstruction to atomic movement along these defect paths. In particular, atoms in grain boundaries do not necessarily bond to other atoms. As such, there is no energy requirement to facilitate mass transport by breaking atomic bonds.

Equations 1 and 2 are Fick's laws for the mathematical description of diffusion in one dimension [12]. In the equations, J is the flux of atoms, C is concentration, and x is a linear dimension. The diffusivity or diffusion coefficient D includes the factors that influence the diffusion process [13]. It takes the form of Equation 3 where D_o is the pre-exponential factor, Q is the activation energy, T is temperature, and k is Boltzmann's constant. The diffusivity depends on many factors such as crystalline orientation, surface energy, chemical energy, crystal structure, defect structure, and possibly composition.

$$J = -D\left(\frac{\partial C}{\partial x}\right) \quad (1)$$

$$\frac{\partial C}{\partial t} = -\frac{\partial C}{\partial x}\left(D \cdot \frac{\partial C}{\partial x}\right) \quad (2)$$

$$D = D_o \cdot e^{\left(\frac{-Q}{k \cdot T}\right)} \quad (3)$$

At any given temperature, diffusion may take place along defect paths, in the lattice, or along both circuits simultaneously. Since thermal energy provides a means of overcoming the activation energy for mass transport mechanisms, not all mechanisms will occur to the same extent. (From Equation 3, there are different diffusivities due to different activation energies, among other factors.) One scenario is diffusion occurring along grain boundaries and from an interface or grain boundary into the grain. At relatively low temperatures, mass transport within the grain is either very slow or does not take place. Thus, atomic movement will occur until all the grain boundary volume is full of diffusing species. At higher temperatures, diffusion within the grain will increase and present an exit path for diffusing species in the boundaries. Therefore, grain boundary diffusion will continue, acting as a source of diffusant to the grains. The diffusion will go on until the driving force no longer exists, for example after eliminating concentration gradients within the grain.

Following the classifications of Harrison [14], there are three kinetic regimes for diffusion in an idealized polycrystalline structure (Figure 4). In Type A kinetics there is

extensive diffusion in the bulk and along short circuits. No significant concentration difference exists between the lattice and defects (grain boundaries) and the diffusivities for the bulk and short circuits are similar. At the other extreme of Type C kinetics, the diffusivity along short circuits is high but there is very little or no lattice diffusion. An intermediate regime is Type B kinetics that involves a complicated reaction. Diffusion along the short circuits takes place but these paths are relatively far apart. Thus diffusion in the bulk will lead to complex concentration profiles. The idealized Harrison model is for only one layer of grains where the boundaries extend from one interface to the other.

It is possible to also delimit the kinetic regimes by time or temperature. For very long diffusion times mass transport may result in atoms moving across many separate grains and short circuits. This is a description of Type A kinetics and measurements will yield a combined diffusivity for bulk and short circuit paths. Assuming a lower activation energy along short circuits, such diffusion is likely to continue and dominate at lower temperatures. Experiments where only short circuit diffusion occurs will yield information about the diffusivity along such paths. Other possible ways to describe the kinetic regimes include grain sizes (diffusion distances), extent of leakage between the grains and grain boundaries, or diffusivity.

2.2 THIN FILM DIFFUSION

Diffusion in thin films is more complex than in bulk materials because of the higher volume ratio of defects to grains. In polycrystalline films, defects occupy a proportionately larger volume than in bulk materials [15]. Mass transport along defect paths is more rapid than in the bulk lattice [10]. The result is that diffusion even at low temperatures is significant in thin films. Additional complications [15] include the proximity of free surfaces, film stresses, poor thermal stability, and the sensitivity of film properties to small changes in structure.

It is difficult to extrapolate from the diffusion response of bulk materials at high temperatures to describe the behavior of thin films at lower temperatures [16]. At high temperatures, one diffusion mechanism will tend to dominate the mass transport. In thin films, more than one diffusion mechanism may have an effect, as a result of defects, and this complicates the results.

2.3 COPPER AND NICKEL DIFFUSION

There are several studies of copper and/or nickel diffusion including work for single crystals and thin films. Some of the earliest efforts include a study of nickel diffusion in bulk single crystal copper. An investigation by Mackliet [17] uses radioactive tracers and sectioning techniques to report values for activation energy and diffusivity (Table 1). These results are for lattice diffusion in single crystals at temperatures that exceed 600 °C and apply to mechanisms that occur in bulk material or within the grains of thin polycrystalline films. Other workers, using a similar tracer-sectioning technique [18] or by a resistometric method [19], obtained comparable results (Table 1). In the latter study, the resistometric method [20] relates electrical resistivity to diffusion.

Solute/ Solvent	Activation Energy, eV/atom	D_o, Pre-Exponential, cm^2/sec	Anneal Temperature, °C	Analysis Method	Reference
Ni/Cu	2.45	2.7	740-1075	Tracer/ Sectioning	[17]
Ni/Cu	2.47	3.8	695-1061	Tracer/ Sectioning	[18]
Ni/Cu	2.45	1.95	780-1037	Resistometric	[19]
Cu/Ni	2.64	0.27	775-1050	Thin Film, Microprobe	[21]

Table 1: Lattice Diffusion for Copper and Nickel in Single Crystals

Helfmeier and Feller-Kniepmeier studied the diffusion of copper into single crystals of nickel [21]. Their methodology to examine mass transport was to measure concentration gradients, with an electron microprobe, on ground samples of thick copper

layers (>1 μm) on single crystals of nickel. The copper deposition method was vacuum evaporation and heat treatment temperatures ranged from 775 °C to 1050 °C. The authors report an activation energy and pre-exponential factor of 2.64 eV and 0.27 cm^2/sec, respectively. Their results agree with other workers using different experimental techniques (referenced in the same paper). In addition, Helfmeier and Feller-Kniepmeier made comparisons with polycrystalline films and found there were significant differences in the diffusion behavior near both grain boundaries and twins.

For thin film structures, Suni has investigated diffusion in copper and nickel bilayers [16]. The film deposition method was electron beam evaporation and their temperature of study was above 400 °C. The RBS results show that a transformation, from a bilayer structure to a single layer, takes place during vacuum annealing. The mixing is significant at temperatures of 500 °C and above. Resistivity and x-ray diffraction measurements support a conclusion of solid solution mixing.

Lewis and Ho [22] investigate the interdiffusion in copper and nickel thin films using AES. The film deposition method was evaporation and annealing took place in a helium ambient at temperatures between 300 °C and 600 °C. The results show fast diffusion of the underlayer elements (copper or nickel) through the thin capping films (nickel or copper) and faster kinetics for nickel diffusion into copper. A summary of their results appears in Table 2.

Lewis and Ho [22] also reference the work by Suni [16] and describe, as an impediment of the technique, the difficulty for RBS to distinguish copper and nickel. With

the small difference in mass, the back scatter peaks overlap and hide potential spectrum changes that result from low levels of atomic movement. However, with an appropriate design of the film structure (thickness), it may still prove worthwhile to use RBS in conjunction with other measurement techniques. A discussion appears in Section 3.0 about the applicability of RBS to measure diffusion in copper nickel structures.

Solute/ Solvent	Activation Energy, eV/atom	D_o, Pre-Exponential, cm^2/sec	Anneal Temperature, °C	Analysis Method	Reference
Cu/Ni	1.31	7.6×10^{-5}	280-405	AES	[23]
Cu/Ni	1.56	4.0×10^{-6}	300-500	AES	[22]
Ni/Cu	1.46	4.2×10^{-2}	280-405	AES	[23]
Ni/Cu	1.55	6.3×10^{-4}	300-500	AES	[22]

Table 2: Grain Boundary Diffusion for Copper and Nickel in Thin Films

Also using AES and depth profiling, Lefakis obtained activation energies and diffusion coefficients for diffusion in copper and nickel thin films [23]. Table 2 contains a summary of the results. The analysis uses the Whipple-Suzuoka model [24] to determine the grain boundary diffusion in a Type B kinetics regime. Lefakis reports that both lattice and grain boundary diffusion occur simultaneously at 280 °C to 405 °C.

A difficulty in the Lefakis report is the large uncertainty in the results. The authors discuss possible reasons and include questions about the kinetic regime of the diffusion process. Also, the Whipple-Suzuoka model applies to stationary grain boundaries that extend from interface to interface. Neither of these circumstances existed for the

experiment yet no differences were in evidence between small and large deviations from the boundary conditions.

There are difficulties in using AES to measure diffusion in copper and nickel thin film structures. The Auger transition energies for copper are at 920 eV, 849 eV, 840 eV, 776 eV, 731 eV and 718 eV (Figure 5). Most of the copper transitions overlap those for nickel at 848 eV, 783 eV, and 716 eV (Figure 6). The lower energy transitions (<700 eV) are impracticable to measure because they require excessively long integration times. Therefore, a nickel signal, for a sample with both copper and nickel, is the combined result of Auger transitions from two elements. Without compensating for this overlap there is confusion in the nickel result when copper is present. It is possible that the large uncertainty in the results of Lefakis is due to not removing the copper contribution from the nickel signal.

In previous work by Ho, a co-author with Lefakis, there is reference to a paper by Tarng and Wehner [25]. This work is a study of using AES to investigate copper nickel alloys. The authors submit that the nickel Auger transition at 720 eV does "not overlap with other peaks." This is clearly not the case (Figures 5 and 6). Even though the copper transition near 720 eV is small, the worst case scenario occurs in the regime of most interest when low levels of nickel are moving in a copper matrix.

There are ways to get rid of the mixture of two transitions in the Auger data. For copper and nickel, the algorithm involves measuring the ratio between the two element signals when only copper is present in the sample. Then eliminating the copper

contribution when nickel is present by subtracting a fraction of the copper signal found with the pre-determined ratio. In this work, the approach was to use an untested algorithm to reduce the data and eliminate the overlap between copper and nickel Auger signals. More discussion of this appears in Appendix II.

Other works on mass transport in copper and nickel thin film structures include Tsakalakos and Hilliard [26] and Klöber [27]. The first report describes diffusion for composition modulated thin films in the temperature range of 375 °C to 450 °C. The authors arrive at an activation energy of 2.8 eV for "interdiffusivity." The result is from x-ray diffraction intensity decays and mathematical modeling. Klöber reports on diffusion in porous nickel layers on copper tin substrates. The report arrives at an activation energy and diffusivity of 0.85 eV and 3.2 x 10^{-3} cm^2/sec, respectively.

Klöber's work explores diffusion along a different short circuit path than dislocations and grain boundaries. Internal free surfaces such as pores are similar to very large grain boundaries or external surfaces; their capacity is high and their resistance to mass transport is low. The deposition in Klöber's work is by a galvanic technique to produce the porous film. The internal structure of a thin film, its dislocation density, grain boundary volume, and porosity, depends on the deposition method and conditions.

Using some of the diffusion results above (Tables 1 and 2), and an expression defining the permeation distance ($\sqrt{D \cdot t}$), it is possible to make comparisons between short circuit and lattice diffusion. The equation for permeation distance is a characteristic length of diffusion and does not represent the ultimate distance an atom will travel. It is

the effective distance the solute travels. This exercise provides initial estimates on the extent of diffusion as well as a means to compare different diffusion mechanisms. A summary of the estimates appears in Table 3. The permeation distance from grain boundary diffusion of nickel in copper is greater than 1 μm after 8 hours at 400 °C. This is greater than the 19 Å from lattice diffusion only. For comparison, the permeation distance of copper along internal free surfaces in nickel films [27] is approximately 63 μm after 8 hours at 400 °C and over 4 μm after 8 hours at 225 °C.

Temperature, °C	Time, hours	Diffusion Path	Ref.	D_o, Pre-Exponential, cm^2/sec	Activation, Energy, eV	Permeation Distance, Å
225	8	Lattice	[17]	2.7	2.45	<1
225	8	Boundary	[23]	4.2×10^{-2}	1.46	142
400	8	Lattice	[17]	2.7	2.45	19
400	8	Boundary	[23]	4.2×10^{-2}	1.46	11,386

Table 3: Permeation Distance Calculations for Nickel Diffusion in Copper

The previous work on diffusion for copper and nickel thin film structures qualitatively show that mass transport of both elements takes place. Furthermore, diffusion will occur at temperatures similar to processing and operating conditions. There is also evidence that nickel will move faster than copper. The earlier studies do report values for activation energy and diffusivity. However, there is some uncertainty in the results for diffusion in thin films and a large variation between different groups (Table 2). It remains for this study to either reinforce the results of former workers or add more insight into interactions that take place in a copper and nickel thin film couple.

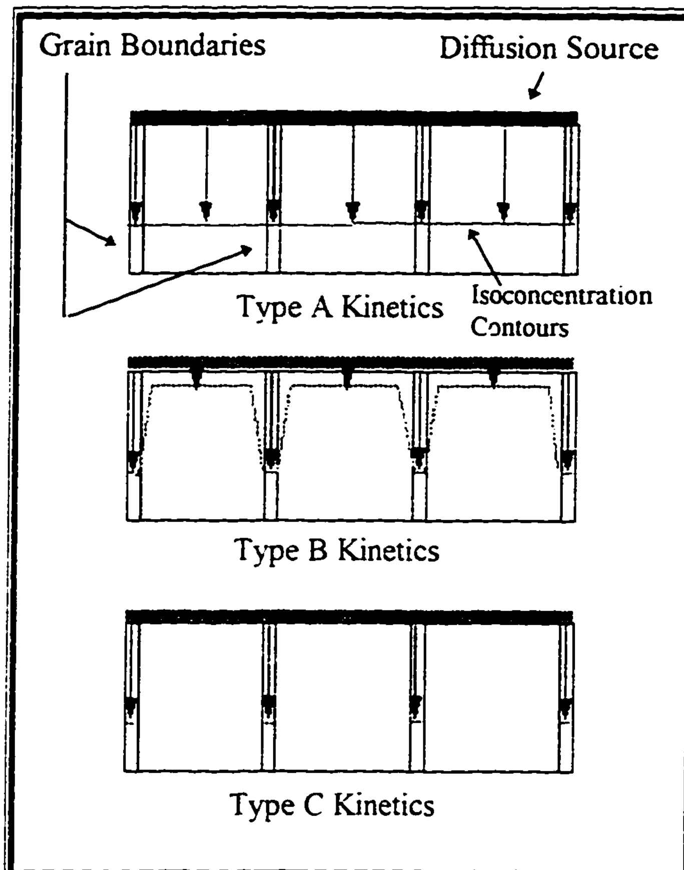

Figure 4: Schematic of Diffusion Kinetic Regimes

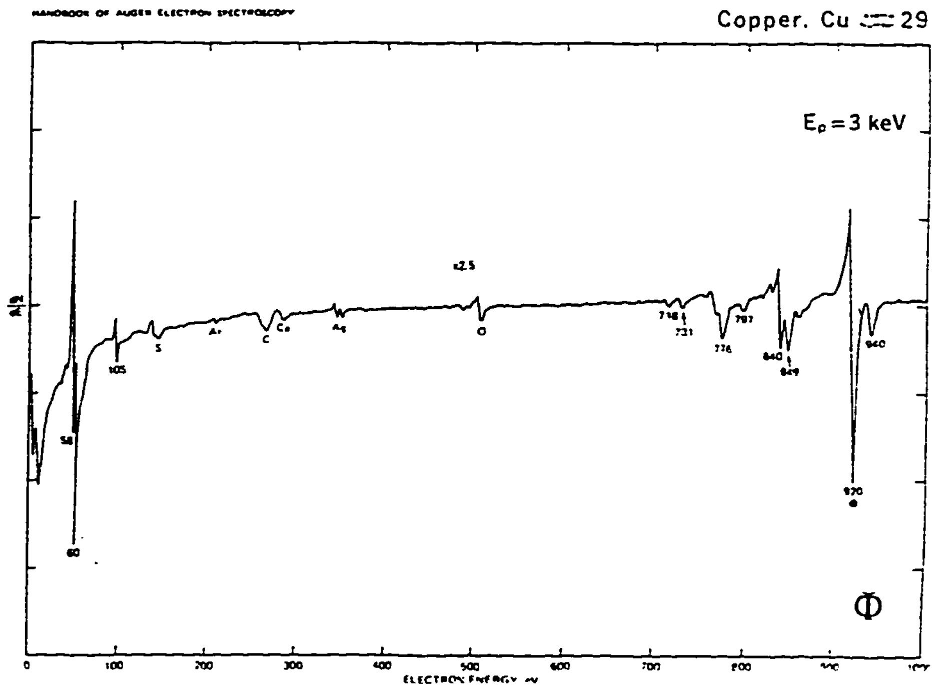

Figure 5: Auger Transition Energies for Copper [30]

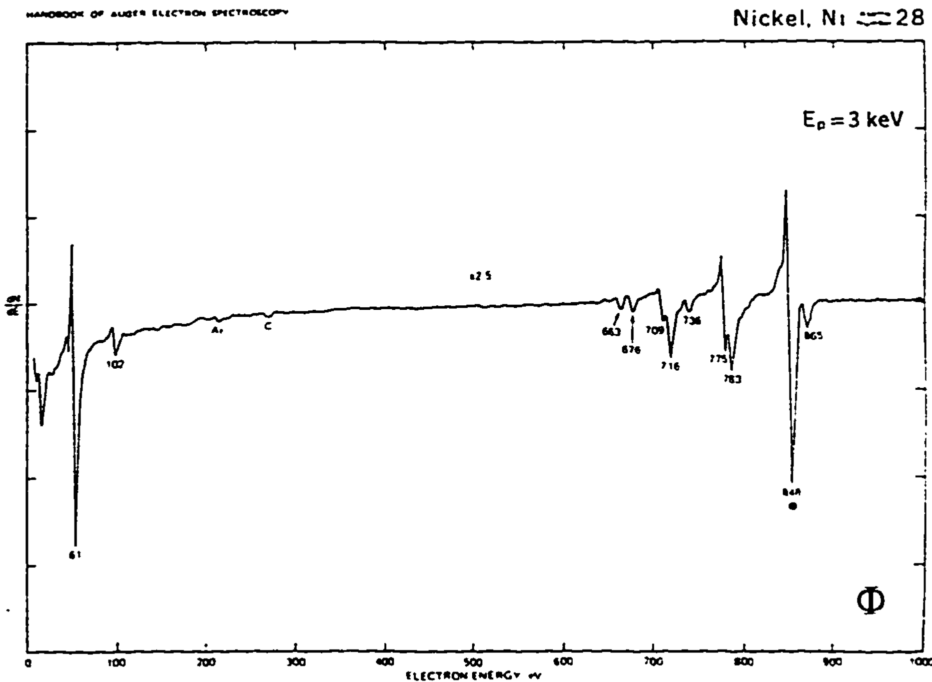

Figure 6: Auger Transition Energies for Nickel [30]

3.0 EXPERIMENT

3.1 OUTLINE

To determine if mass transport occurs and to measure the interactions in copper and nickel bilayers, this experiment used the following procedures. Substrate preparation included thermal oxidation of silicon substrates and then cleaning before film deposition (Figure 7). Heat treatment and then measurement by RBS, AES, and XRD followed film deposition. RBS and AES measure the distribution of elements in the sample and are complementary techniques. XRD patterns help to determine the phases present in the films and lead to the determination of grain size. This work employed an algorithm to remove the overlap between copper and nickel in AES depth profiling. Development of this algorithm was by the author with help from Dr. Vaughn Deline (IBM).

The substrates are <100>, 1 " diameter silicon wafers, lightly doped with boron to 8-12 Ω-cm. To prevent reactions between the metal film and silicon, there is a thermal oxide on the wafer surface at a thickness of 800 Å (approximate). The oxidation took place in room air at 1100 °C using a horizontal furnace (SJSU IC Laboratory).

Film deposition took place at the IBM Almaden Research Center. After film deposition, each substrate was broken into three pieces: one half of each wafer remains in the post deposition (parent) condition while two quarters (child samples) provide the material for heat treatment. Heat treatment and measurement of the films also took place at IBM's Almaden Research Center.

3.2 THIN FILM DEPOSITION

3.2.1 Pre-Deposition Clean

This is a general purpose cleaning technique to remove particles from the wafer surface.

1. Dip in a sulfuric acid plus ammonium persulfate mix (1:1) for >5 minutes.

2. Rinse in aspirated de-ionized water for >5 minutes.

3. Rinse in flowing de-ionized water to a resistivity of >7.0 MΩ-cm.

4. Dry in IPA vapor, at the vapor temperature, for 2 minutes.

5. Dry in nitrogen at 105 °C for >2 minutes.

3.2.2 Deposition

The film deposition method is sputtering with argon gas. The plasma energy is RF for nickel and DC magnetron for copper. Sample preparations are for both deposition sequences (copper on nickel and nickel on copper). The top metal film is the overlayer and the metal film below the overlayer is the underlayer (Figure 7). Table 4 illustrates the typical deposition conditions; it was necessary to adjust the power during deposition to maintain the deposition rate at approximately 3 Å/sec. The target thickness for both copper and nickel was 800 Å each. The base pressure of the chamber before deposition was better than 5×10^{-7} Torr.

PARAMETER	COPPER	NICKEL
CHAMBER PRESSURE, mTorr	2.2	2.2
ARGON SOURCE PRESSURE, μm Hg	50.0	50.0
TARGET CLEAN TIME, min	>5	>5
TARGET CLEAN POWER, W	50	50
DEPOSITION POWER, W	180-182	248-280
BIAS VOLTAGE, V	-238	--
DEPOSITION RATE, Å/sec	3.0 ± 0.3	3.0 ± 0.3

Table 4: Thin Film Deposition Conditions

3.3 HEAT TREATMENT

The heat treatment furnace uses flowing helium that has been gettered over titanium. There are two titanium getter furnaces in the flow path before the heat treatment furnace. Each titanium furnace is at a temperature of 800 °C (Figure 8). The 160 cm furnace tube is closed at both ends except to allow ingress and egress of helium. The process cycle starts with a 40 minute soak in the load section of the tube. This allows sufficient time to eliminate any oxygen from the heat treatment atmosphere. A push into the hot zone follows the soak; the push distance is 55 cm with a travel time of 30 seconds. The preset furnace temperatures and times for heat treatment are in Table 5. The pull cycle has the same distance and time as the push cycle. Before removing, the samples remain in the load section to cool for a minimum of 25 minutes.

TEMPERATURE, °C TIME, hours	225	250	300	350	400
1				x	x
2			x	x	
4		x	x	x	
8	x	x	x	x	x
16	x	x	x		
32	x	x			
64	x				

Table 5: Heat Treatment Time Temperature Matrix

There are two possible extreme outcomes from the heat treatment process. At all temperatures and times, one result is any reaction will go to completion The second

outcome is the other extreme where the heat treatment conditions do not allow the reaction to sufficiently progress. In both cases, any measurements may not resolve differences in the final conditions. Therefore, the choice of heat treatment conditions, and thickness of each film, was designed to afford measurable differences after processing.

3.4 RUTHERFORD BACKSCATTERING SPECTROMETRY

The RBS technique measures the energy and direction of helium ions scattered by matter in the target material. These properties identify and locate the scattering atom within the film structure. The principles and details of the measurement technique are in the next section and Appendix I.

In this experiment. the purpose of RBS was to measure changes in the distribution of constituent elements as a result of heat treatment. Low beam currents reduce the impact of pulse pile up RBS measurements (see Appendix I). Table 6 outlines the typical conditions for the RBS measurements. The measurements produce a spectrum of back scattering yield (number of detectable back scattering events) versus energy. The difference in spectra of samples in their various conditions is evidence of mass transport. The specific differences can determine the direction and extent of mass transport.

Collected Charge, μC	40
Beam Energy, MeV	2.3
Beam Current, nA	6-10
Detector Angles, °	120, 170
Sample Tilt, °	0, 7
Dead Time, %	<5
Chamber Pressure, Torr	$<5 \times 10^{-6}$

Table 6: Typical Conditions for RBS Measurements

3.5 RBS SIMULATIONS

The back scattering process relies on the assumptions that the collisions of the primary ions with the target material are elastic. Calculating changes in energy and momentum of the incident ions determines the energy and direction of back scattered particles. This is a simplified approach as it does not take into account many details (see Appendix I). However, it is possible to simulate a back scatter spectrum using very simple rationales.

The Rutherford Universal Manipulation Program (RUMP) is a DOS application [29] that simulates back scatter spectra for different measurement conditions and film arrangements. It is a useful tool to help design a structure that will provide the most information or to determine in advance how the spectra may change. The thickness of the copper and nickel layers is an important variable that determines what information there is to gain from a back scatter spectrum. There is also the necessity to use a structure with sufficient thickness such that there are measurable changes after heat treatment.

Figures 9 and 10 illustrate simulations for the chosen structure and RBS condition. A typical spectrum (Figure 9) for copper on nickel consists of three distinct regions of back scatter counts versus energy, shown as a black line. The colored lines represent simulations of the individual back scattering spectra for copper and nickel. The RBS measurement is the sum of these two spectra.

Starting at the high energy side, the first peak represents the copper overlayer. The front of the peak starts at the energy of ions back scattered from the surface of the copper

The helium ions will also traverse the copper layer in the forward and scattering direction. In doing so, ions lose energy through ionization that results in broadening of the peak. The energy distribution is from scattering events throughout the depth of the copper film. The peak area then represents the areal density of copper or, with accurate knowledge of film density and ion counting, the thickness of the film.

The second peak occurs by back scattering from the nickel underlayer. Similar arguments apply to the width of the nickel peak as apply to copper. However, the helium ions lose energy by having to cross through the overlayer twice. Therefore, the nickel signal displaces to lower energies than its surface position. A slight overlap of back scatter energies from both copper and nickel causes a valley between the copper and nickel signals. A change in the thickness of the overlayer changes the energy but the width of the valley remains essentially the same

The remaining region of the spectrum represents back scattering from the silicon substrate and its oxide layer. Since the substrate is very thick, and detectable scattering does not occur far below 1 μm, the energy counts eventually drop off to zero. The energy lost through traversing the copper and nickel also displaces the position of the silicon peak. Since the back scatter energy of oxygen in the SiO_2 is below that of silicon, the oxide peak appears as a "bump" in the middle of the substrate signal. The silicon from the SiO_2 appears at the high energy side of the substrate signal. However, the oxide thickness is small enough that it is not easy to differentiate the two silicon signals.

For the nickel on copper structure there is an overlap peak (Figure 10) instead of a valley. This is because the difference in the back scatter energies is smaller when nickel is the overlayer. All the same details apply to the position and width of the peaks from each element. If the copper and nickel layers have the same thickness for either deposition sequences, the position of the substrate signal remains the same, despite the order of the metal layers. There is still the same mass of material for the ions to cross before reaching the substrate.

The simulations in Figures 9 and 10 are for metal layers with a thickness 800 Å each. This is the target thickness for deposition and it provides adequate regions on either side of the overlap region in the RBS spectra. These regions are the flat top parts of back scattering from the metal layers (Figures 9 and 10) and should make it easier to visibly see changes in the spectra (discussed next). The 800 Å thickness is larger than the permeation distance for the shortest time, lowest temperature heat treatment (Table 3). It is also smaller than the permeation distance from the longest time, highest temperature heat treatment (Table 3).

Figures 11 to 15 are plots from RUMP simulations that show just the metal layers; they also reflect changes that can occur during heat treatment. Figure 11 shows a simple outcome where mass transport extends evenly throughout the two layers in the copper on nickel deposition sequence. The starting model for this is two layers that are pure and represent the post deposition condition. Their RBS spectrum is similar to Figure 9. The comparison simulation is simply two layers with a small concentration of the diffusing

element. The diffusing element has a continuous concentration throughout the thickness of the layer into which it diffuses. There are three significant differences in Figure 11 evident between the post deposition spectrum (black solid line) and heat treatment spectrum (red solid line). The back scattering yield of the valley region between the metal peaks increases. Also, the yield at the low energy side of the nickel peak and at the high energy side of the copper peak decreases. The broken lines show the yield for individual elements from the heat treatment simulation; the signal from both elements now extends into the matrix of the opposite layer (compare with Figure 9).

Figure 12 is for the opposite deposition sequence of nickel on copper and is the equivalent plot of Figure 11. The most obvious difference between the spectra of the post deposition (black lines) and heat treatment (red lines) simulations is a decrease in the yield of the overlap peak. Less obvious but still visible is the change in yield at the high energy side of the nickel signal. This difference occurs because the back scatter energy of copper, at the same depth within the thin film structure, is higher than that of nickel. There is a similar change representing nickel at the back side of the thin film structure as seen at the low energy side of the copper peak.

Figures 13 and 14 show the same simulations as Figures 11 and 12 except there is a variation in composition of diffusant throughout the solvent layer thickness. The model for this simulation is several layers with different compositions. The diffusing element composition decreases the greater the distance away from its original layer. The solid lines represent simulations of the RBS measurement for the post deposition (black) and post

heat treatment (red) conditions. The broken lines are the simulations of the individual elements in the condition that represents heat treatment. For the copper on nickel deposition sequence (Figure 13), the high energy side of the nickel peak and the low energy side of the copper peak show clear reductions in yield. This applies to the heat treatment representation (solid red lines). These changes represent the varying concentrations of one element in the matrix of the other element where the concentration starts out higher at the interface. In the opposite deposition sequence, the overlap peak is broader after inhomogeneous mass transport (Figure 14). Comparing Figures 13 and 14 with Figures 11 and 12 plainly show the result of the different distributions of diffusing elements. The significance of these simulations is that RBS can distinguish between bilayers with concentration gradients typical of lattice diffusion and with constant solute concentrations. The latter is typical of grain boundary diffusion where mass transport has completely filled the grain boundaries.

Figure 15 is a simulation of the copper on nickel structure; there is more nickel transport into copper than copper in the opposite direction (compare with Figure 11). The significant change to the RBS spectrum is the (energy) position of the overlap valley. As more nickel moves into the copper layer there is a decrease in energy of the overlap valley. The opposite is true if more copper diffuses into the nickel layer and a similar behavior occurs for the overlap peak for the opposite deposition sequence. The position of the overlap valley or peak, depending on the deposition sequence, will move in the opposite direction of the element that has the most diffusion with heat treatment. For copper on

nickel, the valley will move forward in the spectrum if more copper diffuses from the overlayer into the nickel underlayer. The valley will move backward in the spectrum if more nickel from the underlayer diffuses into the copper overlayer.

3.6 AUGER ELECTRON SPECTROSCOPY

AES uses a primary electron beam to excite atoms in a target material. As the atoms return to their ground state they can emit Auger electrons. The energy of these particular electrons is characteristic of the source atom and the intensity of the signal is proportional to the element's concentration. Appendix II gives more details of this method of measuring element distributions including some limitations.

In this experiment, there are two AES techniques to detect the evidence of mass transport. The first is a surface survey that measures the Auger transitions of elements present at the surface of a thin film structure. The detectable Auger transitions originate from the top 30 Å of the overlayer. This measurement technique produces a spectrum of signal intensity versus transition energy. The energy of the detectable transitions determines the element identity and can help to determine the arrival of an underlayer element after diffusion through the overlayer thickness. The conditions for the AES surface survey are in Table 7.

Primary Electron Beam Energy, KeV	3.0
Electron Beam Current, μA	1 - 2
Energy Scan, eV	1 - 1000
Step Time, ms/step	100
Step Size, eV/step	0.5
Measurement Cycles	5
Chamber Base Pressure, Torr	$<10^{-9}$

Table 7: Typical Conditions for AES Surface Surveys

The second technique involves depth profiling to measure the distribution of copper and nickel in the post deposition and heat treatment samples. The objective is to determine if any significant diffusion takes place and to support the results of the RBS measurements. Depth profiling itself is by alternate sputtering and measurement steps. At each step, measurements of the electron emission intensity are made within an energy window for each element of interest. After reducing the data (see Appendix II), this method will produce a measurement of concentration versus sputter time (or depth). Table 8 outlines the typical depth profiling conditions and Table 9 is a list of the specific element scans (AES energy windows). The energy and range in Table 9 define the energy window for each element (see also Appendix II and Figures 5 and 6) and encompass the Auger transition energy for that element. The step size and step time define the measurement steps made within the energy window. There are multiple sweeps within each energy window.

Primary Electron Beam Energy, KeV	3.0
Electron Beam Current, μA	1 - 2
Argon Beam Energy, KeV	3.0
Argon Beam Current, μA	25
Argon Partial Pressure, Torr	$\leq 2 \times 10^{-7}$
Sputter Area, mm^2	1.5 - 2.0
Depth Profile Sputter Time, sec/step	0.5 - 0.8
Chamber Base Pressure, Torr	$< 10^{-9}$

Table 8: Typical Conditions for AES Depth Profiles

Element	Energy, eV	Range, eV	Step Size, eV/step	Step Time, ms/step	Sweeps
Carbon	257	30	50	50	5
Oxygen	350	20	50	50	5
Nickel	765	20	50	50	5
Copper	905	20	50	50	5

Table 9: Element Energy Window Scans for AES Depth Profiling

Since the Auger transition energy for nickel overlaps with a lower transition for copper it was necessary to use data reduction. The procedure was to take measurements in the copper and nickel energy windows when only copper was present in the material. This helps to determine the contribution of copper to the nickel signal when both elements are present. More details of this algorithm appear in Appendix II.

3.7 X-RAY DIFFRACTION

In X-Ray Diffraction (XRD), a beam of x-rays will diffract off a polycrystalline material if the arrangement satisfies the Bragg condition. The diffraction angles and widths of the diffraction peaks provide information about crystal structure. Details of this measurement technique appear in Appendix III. The purpose of x-ray diffraction measurements is to determine changes in either the phase or grain sizes of the copper and nickel films following heat treatment. Mass transport will facilitate both reactions. Appendix III has an example diffraction pattern.

The measurements are of diffracted beam intensity versus the angle of diffraction; a peak will appear at the conditions of constructive interference. The peak position determines the crystal planes responsible for diffraction while its width is a measure of the average size of the diffracting particle. In this experiment, the diffraction conditions are for normal coupled scans using the radiation line of Cu K_{α}. The range of diffraction angle measurements is 40 to 100 °. The step size and time are 0.050 ° and 10.0 seconds, respectively.

3.8 FIGURES

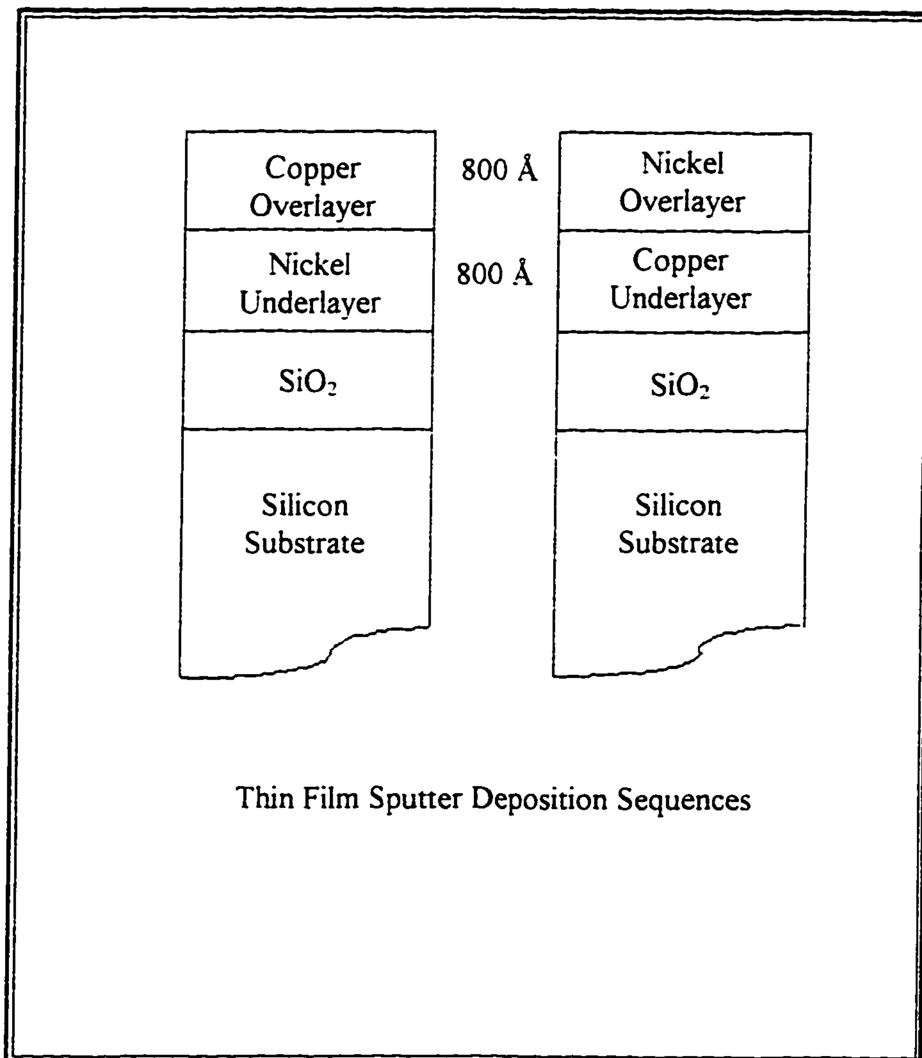

Figure 7 Schematic of Thin Film Structures

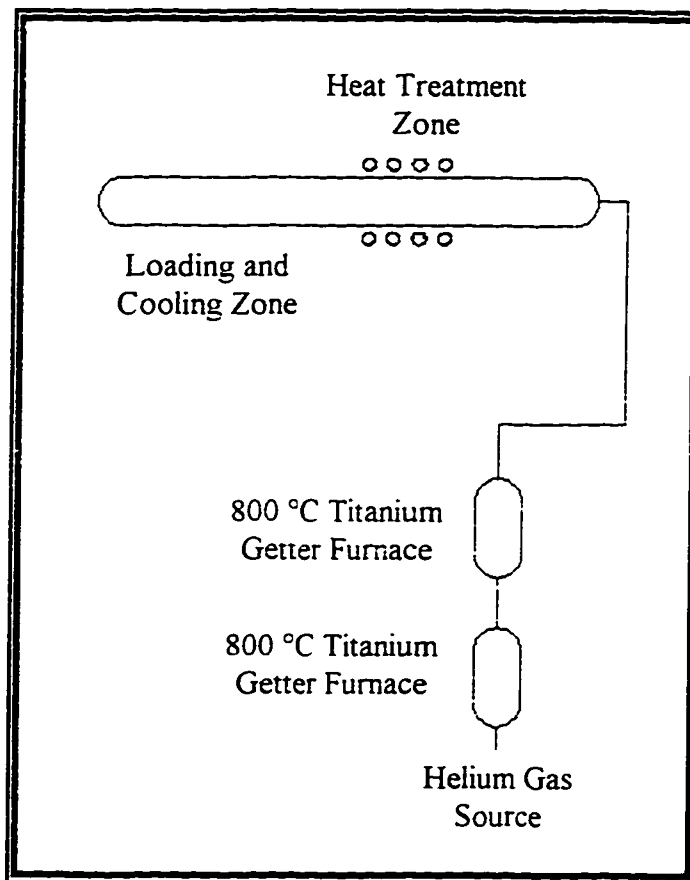

Figure 8: Schematic of Heat Treatment Furnace

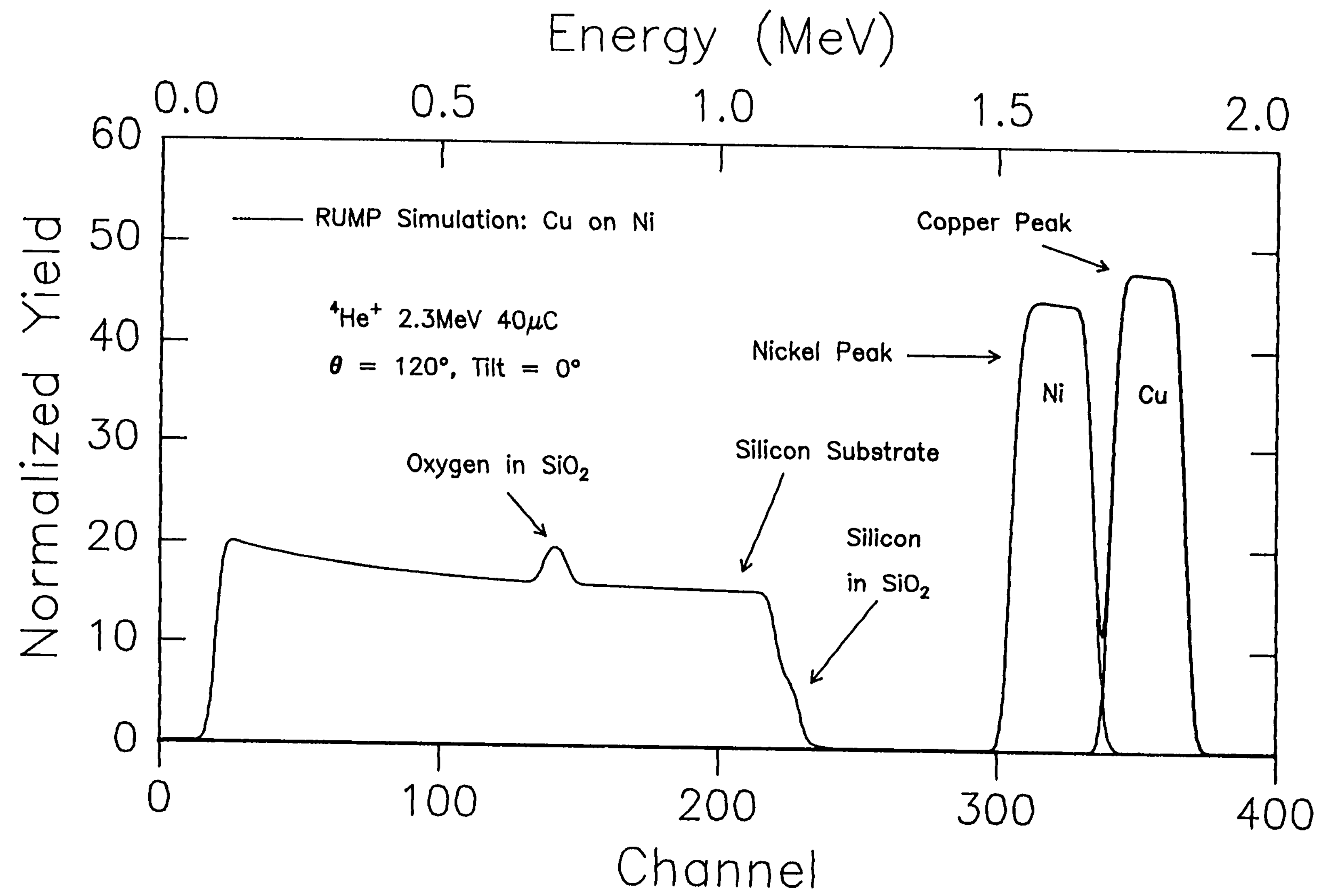

Figure 9: RBS Simulation of a Copper on Nickel Thin Film Structure

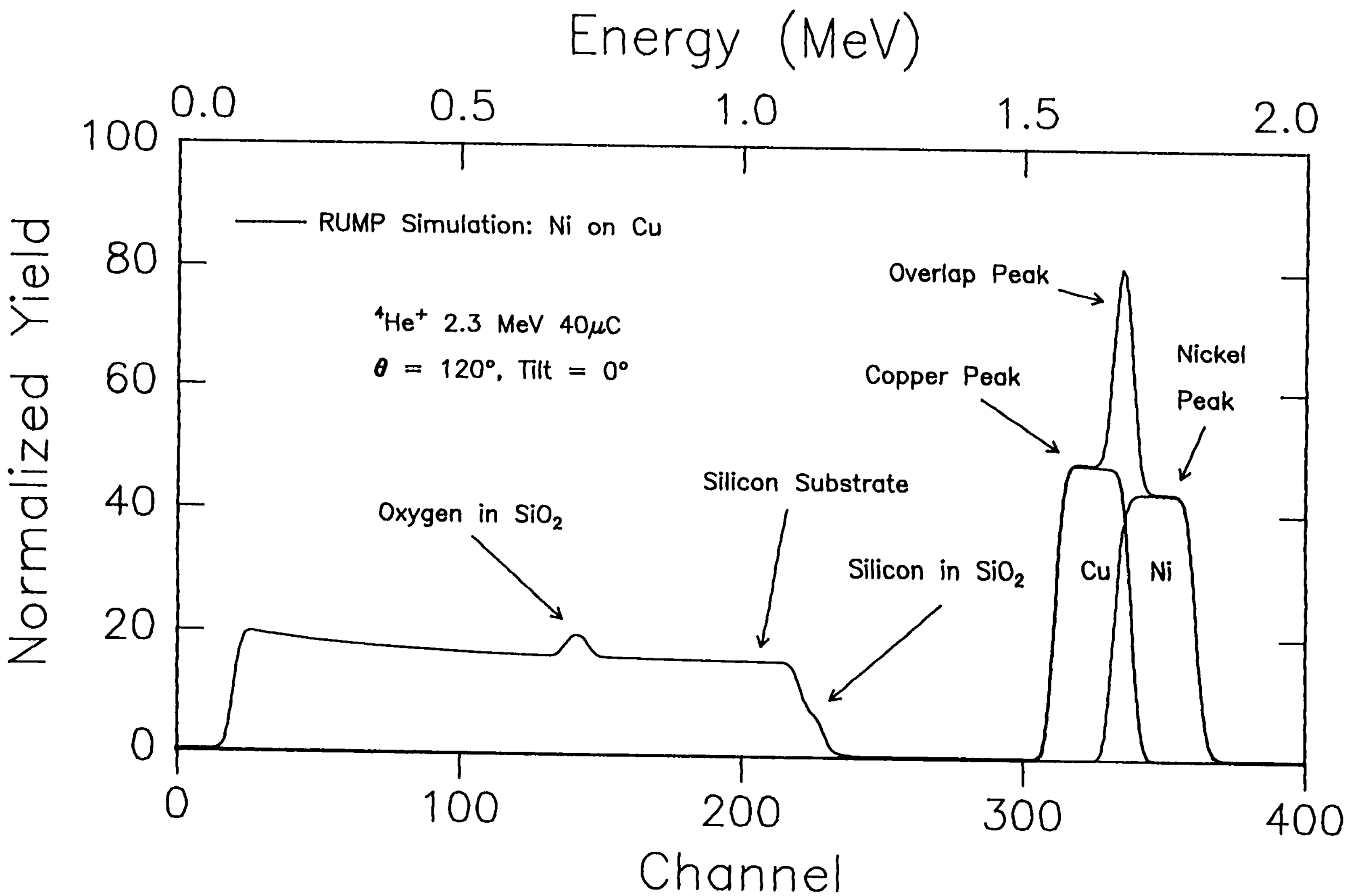

Figure 10: RBS Simulation of a Nickel on Copper Thin Film Structure

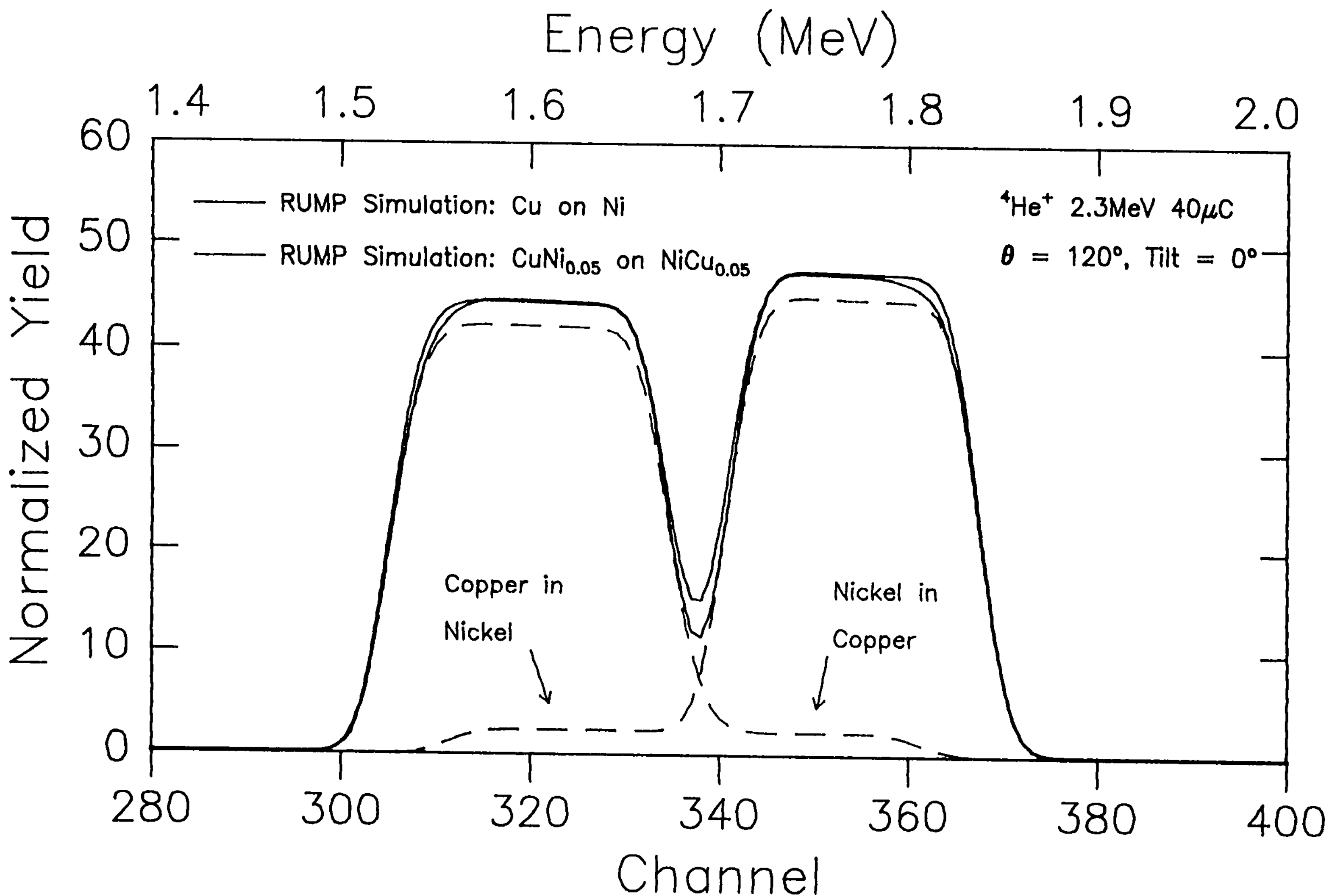

Figure 11: RBS Simulation of Equal Mass Transport in Copper on Nickel Films

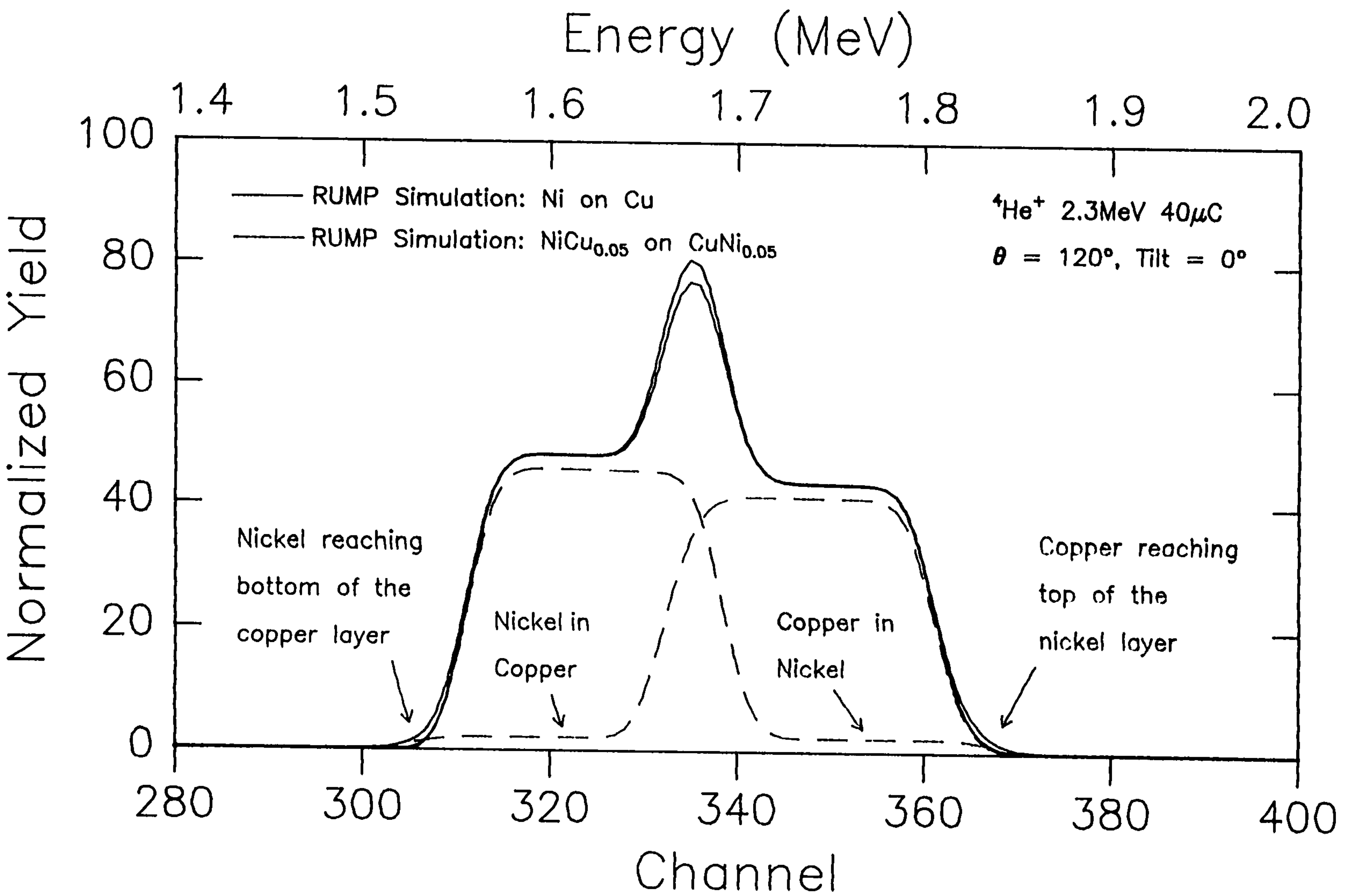

Figure 12: RBS Simulation of Equal Mass Transport in Nickel on Copper Films

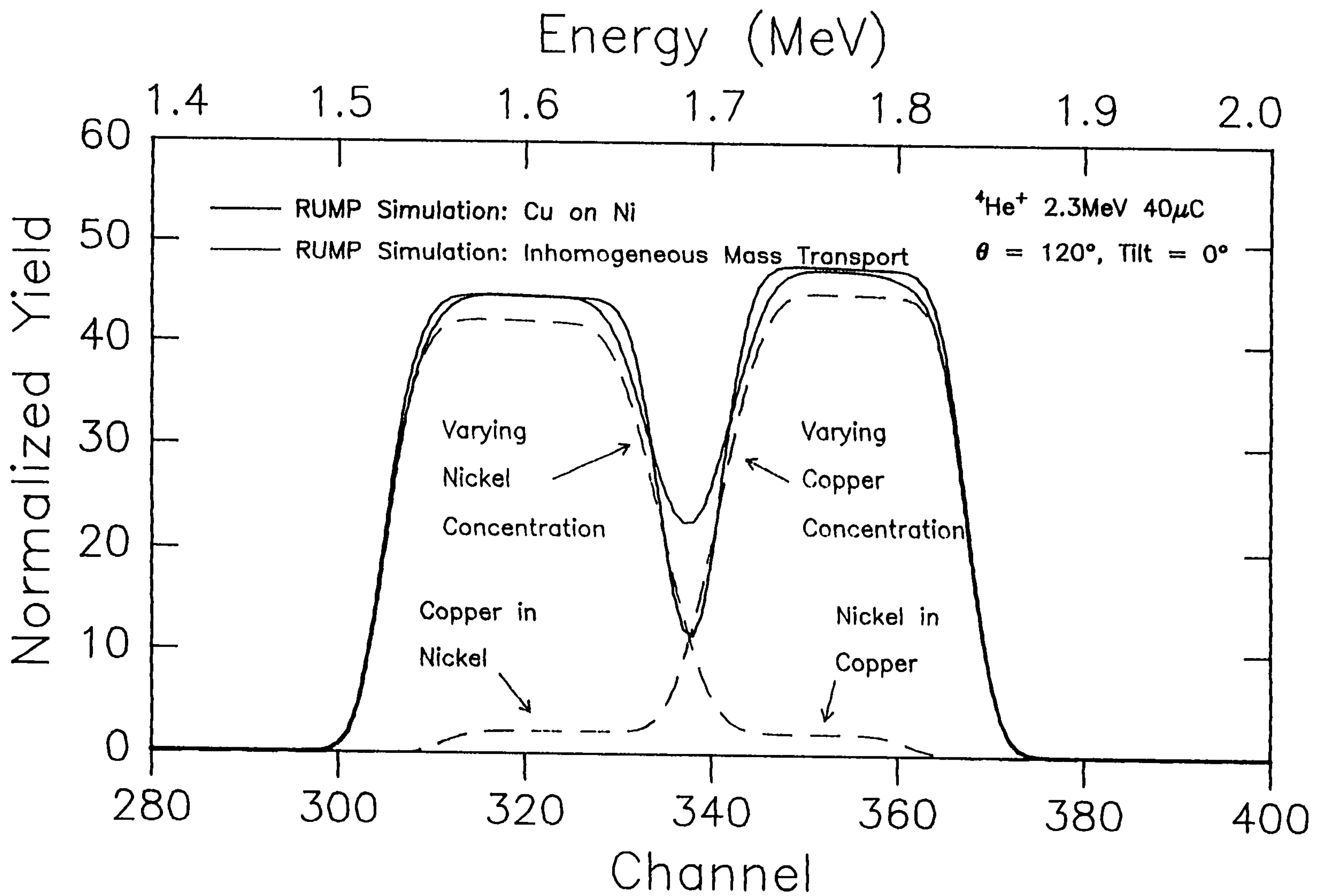

Figure 13: RBS Simulation of Inhomogeneous Concentrations in Copper on Nickel Films

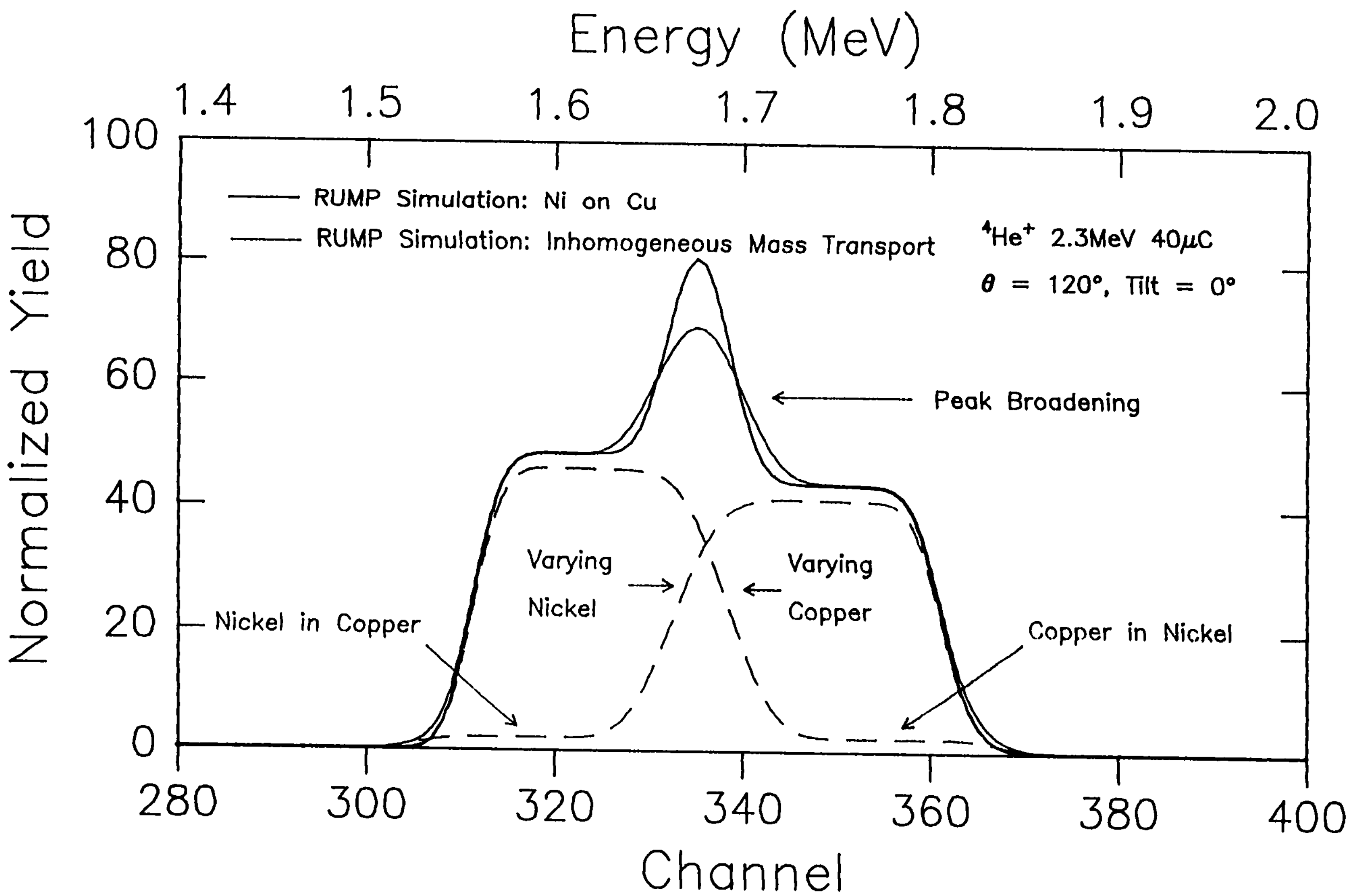

Figure 14: RBS Simulation of Inhomogeneous Concentrations in Nickel on Copper Films

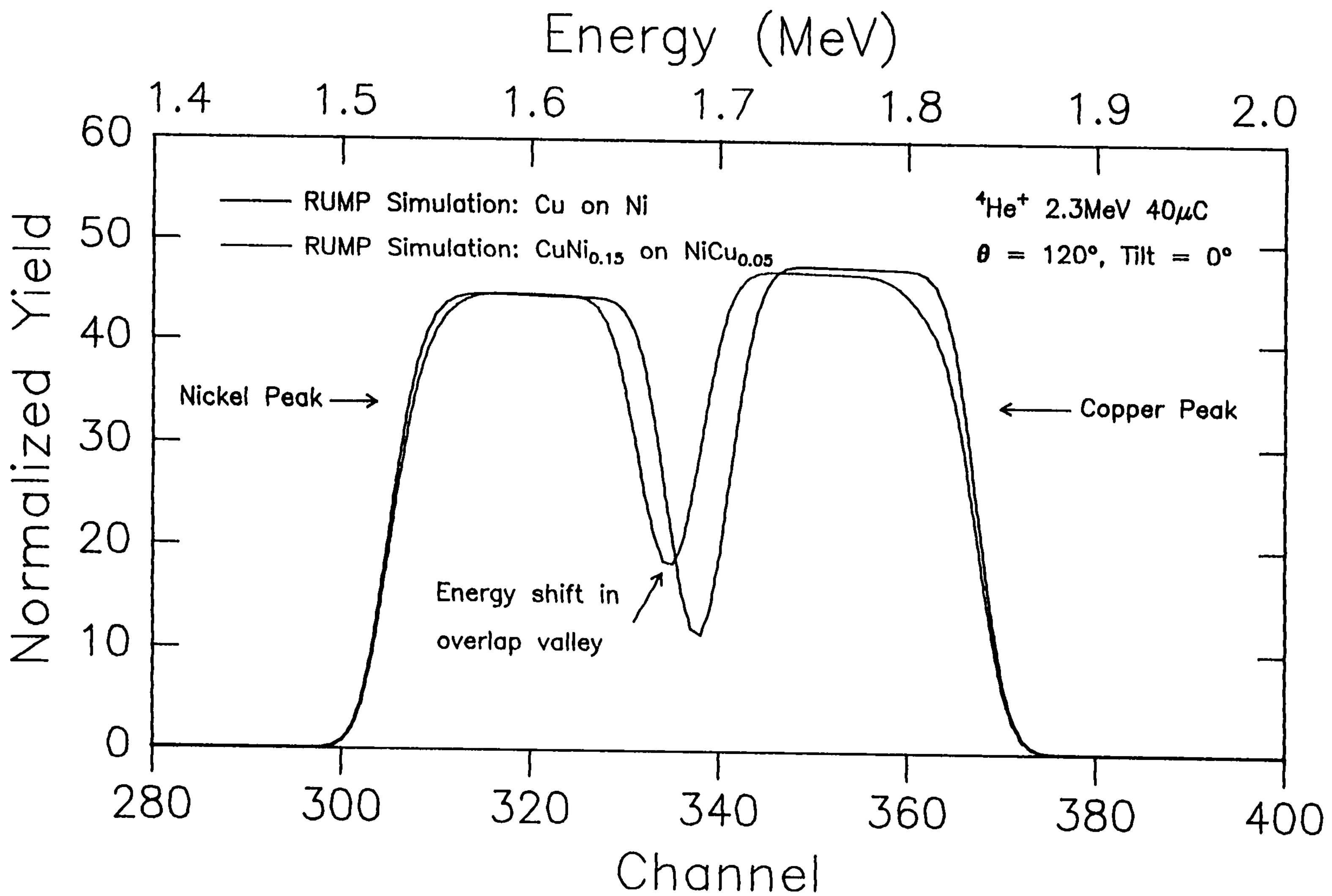

Figure 15: RBS Simulation of Unequal Mass Transport in Copper on Nickel Films

4.0 RESULTS

4.1 PHYSICAL OBSERVATIONS

After heat treatment there were no significant changes visible in or on the samples except for a transition in color. The copper on nickel structure after deposition has a red copper color on the surface. After heat treatment at the higher temperatures (>300 °C) a metallic gray appearance replaces the copper color. After heat treatment at all the lower temperatures, the copper color fades but still remains visible. The surface appearance of the nickel on copper structure did not change with any heat treatment condition.

Optical and electron microscopy inspections show that the surface is relatively smooth and flat. In addition, the surface topography remains the same after all heat treatments. The films remained intact and did not peel off the substrate.

4.2 RBS MEASUREMENTS

4.2.1 Copper on Nickel Structure

For the post deposition samples, the film thickness from peak area measurements is 775 ± 22 Å for copper and 799 ± 16 Å for nickel. Calculations from RBS measurements of different parent samples in their post deposition condition determine the average values. The difference in thickness is the variation due mainly to position of the sample in the deposition chamber. There is also a variation in thickness (Figure 16) across each sample, most likely due to the same source as the sample to sample variation. The range in thickness across the sample in Figure 16 is 25 Å for copper and 34 Å for nickel.

The post deposition and heat treatment measurements are for samples that originate from different portions of their original wafer. This forces a variation in thickness on the various conditions. It is difficult to directly compare the RBS spectra of different conditions when there are variations in thickness. The consequence is RBS will detect a different mass of material and the back scattering spectrum of samples will not coincide below the surface signal.

For all samples after heat treatment, there is an increase in the back scatter counts in the overlap energy range (valley) between the two metal peaks (Figure 17). Also, the counts at the peak edge, away from the opposite metal's peak, are smaller for post heat treatment samples. These changes represent mass transport of copper and nickel. Copper is diffusing from the overlayer into the nickel underlayer while nickel is moving in the opposite direction. A simulation of the back scattering spectrum (Figure 11), to illustrate

these changes, shows scattering energies from copper in the nickel layer and from nickel in the copper layer. The decrease at the opposite edges of the metal peaks is due to fewer atoms in the original layer following mass transport.

Another change in the RBS spectra, which is noticeable at heat treatment temperatures of 300 °C and 350 °C, is a decrease in counts at the high energy side of the nickel peak (Figure 18). This is due to a variation in concentration of copper; the change is with depth in the nickel underlayer However, the distribution of nickel in the copper overlayer is apparently homogeneous.

Simulations of the RBS measurements (by RUMP) are able to provide estimates of the diffusing element concentrations in the copper or nickel layers. The atomic concentration of nickel in the copper overlayer, following heat treatment at 225 °C, is approximately 5 % (Figure 19). There is a similar concentration of copper in the nickel underlayer. At the higher temperatures, a complicated RBS simulation (Figure 20) requires multiple layers in the model to closely match the measurement. In this specific case, represented in Figure 21, there are six layers. The uppermost layer has a thickness represented by 7×10^{17} atoms/cm^2 of copper with 45 % nickel. The remaining layers vary in thickness and composition. This is not a unique solution to the RBS measurement but represents an estimate that also relies upon the results from AES depth profiling. Table 10 contains the simulated solute concentrations from of all the heat treatment conditions, with a graph of the same data shown in Figure 22.

The simulation results in Table 10 and Figure 22 assume that the solute distribution is uniform throughout the thickness of the solvent layer and that the interface or surface is not rougher after heat treatment. However, the RBS measurements show that the diffusing element concentration does vary throughout the depth of the solvent layer (Figure 18) when the heat treatment is above 250 °C. Therefore, some results in Table 10 and Figure 22 are concentrations taken from the deepest layer in the simulation and require some caution in the interpretation of their meaning.

Anneal Time, hours	Anneal Temperature, °C	Nickel in Copper Overlayer, %	Copper in Nickel Underlayer, %
8	225	5	5
16		5	5
32		5	5
64		5	5
4	250	6	5
8		6	5
16		6	5
32		6	5
2	300	12	10
4		12	12
8		12	15
16		14	15
1	350	25	16
2		26	17
4		27	17
8		27	17
1	400	40	18
8		45	20

Table 10: RBS Simulation Estimates for Diffusion Concentrations, Copper on Nickel

Figure 22 and Table 10 show that, for 250 °C and below, the solute concentration does not increase with time (other than the initial change upon heat treatment). At higher temperatures, the solute concentration changes with both time and temperature of heat treatment.

4.2.2 Nickel on Copper Structure

The film thickness from peak area measurements of this structure is 766 ± 28 Å for nickel and 821 ± 38 Å for copper. The average values are from RBS measurements of different samples in their as deposit condition. The uncertainty is the variation in thickness due to position of the sample in the deposition chamber. As with the opposite deposition sequence, there is a variation in thickness across each sample.

The RBS overlap peak of copper and nickel exhibits a decrease in the yield for post heat treatment samples (Figure 23). Another change in the RBS spectra is an increase in counts at the high energy side of the nickel scattering (Figure 23) seen at the "foot" of the peak (compare with Figure 13). There is a similar but less obvious change at the low energy "foot" of the copper peak. All of these differences in the RBS spectra indicate mass transport of copper and nickel. In particular, copper is clearly diffusing all the way through the nickel overlayer. However, it is unclear if the copper is spreading over the surface or simply reaches the top surface layer of nickel. The variation in thickness across each sample, and from sample to sample, makes it difficult to emphatically determine if nickel diffuses all the way through the copper underlayer. However, there are enough indications

from RBS measurements to believe that nickel does reach the metal to silicon dioxide boundary.

Table 11 shows the simulated solute concentrations after each heat treatment (Figures 24, 25, and 26). A graph of the same data appears in Figure 27. The simulation results for the high temperature heat treatments are not necessarily unique solutions because of the inhomogeneous diffusion concentrations. This is evident in the copper on nickel structure RBS results (Figure 18). Again, it is necessary to exercise caution when interpreting the data.

Anneal Time, hours	Anneal Temperature, °C	Copper in Nickel Overlayer, %	Nickel in Copper Underlayer, %
8	225	5	5
16		5	5
32		5	5
64		6	6
4	250	6	6
8		7	7
16		6	6
32		7	6
2	300	9	7
4		9	7
8		9	6
16		10	8
1	350	10	8
2		10	10
4		10	11
8		12	10
1	400	17	35
8		25	40

Table 11: RBS Simulation Estimates for Diffusion Concentrations, Nickel on Copper

4.2.3 Contamination

RBS provides an energy spectrum and the technique can therefore simultaneously detect the presence of many elements. Exceptions to this include when there are similar (overlapping) back scattering energies or where the contamination concentration is below the detection limit [3] of the technique (10^{14} to 10^{15} atoms/cm^2). From the RBS spectra, there is no evidence of contamination in the metal layers unless the contaminants are oxygen, silicon, or similar in mass to copper and nickel (cobalt and zinc, for example). This applies to samples after deposition and in their heat treatment conditions. Also, there is no indication that oxygen or silicon, from the substrate or its oxide, diffuses into the metal layers.

4.2.4 Summary of RBS Measurements

The RBS measurements show many of the features and changes seen with the RUMP simulations. Most notable is the change in yield of the overlap portions in the spectra. The RBS results indicate that mass transport between the nickel and copper layers takes place with heat treatment. Both nickel and copper diffuse into the opposite layer, regardless of the deposition sequence. The nickel concentration in the copper underlayer and overlayer is homogeneous It also appears that the copper concentration in the nickel underlayer is inhomogeneous. AES and XRD present more evidence of these conclusions in the next sections.

4.3 AES MEASUREMENTS

4.3.1 Surface Survey

Figure 28 is an example plot of the AES survey results; the measurements are from both deposition sequences before heat treatment. The copper or nickel peaks are visible only when they are the overlayer element. The remaining peaks represent transitions for carbon and oxygen. They appear because of some surface metal oxide and hydrocarbon contaminants from the atmosphere. Figure 29 is an overlay plot for the nickel on copper structure showing the results for post deposition and post heat treatment samples. The appearance of copper at the surface is very evident. When copper is the overlayer element, the appearance of nickel at the surface is less obvious (Figure 30) because of the overlapping transition energies. However, there are differences in the peak shapes at 716 eV and 848 eV but not at 920 eV. The latter energy is the only copper transition that does not overlap with a nickel peak.

4.3.2 Depth Profile

The available AES depth profiles, for the copper on nickel structure, show mass transport of both elements (Figure 31). At the 225 °C and 250 °C heat treatment temperatures, there is an initial change upon heat treatment. However, there is no prominent change in the normalized concentration levels of the diffusing elements with increasing heat treatment time.

At higher temperatures (>250 °C) there is a difference between the overlayer copper diffusing into the nickel underlayer and the mass transport of nickel in the opposite direction (Figure 32). For the latter case, the nickel distribution throughout the bulk of the copper overlayer is uniform. The distribution of copper in the nickel underlayer is only uniform at the lower temperatures (<300 °C). At the higher temperatures, the concentration of copper varies throughout the nickel layer; the concentration profiles of copper and nickel lack any symmetry about the interface region.

Table 12 contains the diffusing element concentrations as they vary with heat treatment time and temperature. The same data appear in Figures 33 and 34. The normalized concentration values assume that the only elements present in the film structure are copper and nickel. At the higher heat treatment temperatures (>300 °C), the distribution of copper in the nickel layer is not uniform. Therefore, the concentration values in Table 12 for the above conditions are estimates based upon the AES concentration at the last or next to last depth profile measurement.

4.3.3 Summary of AES Measurements

The surface survey results clearly indicate that the underlayer element reaches the surface of the overlayer. This takes place before the end of the 8 hours at 225 °C heat treatment and applies to both copper and nickel. The changes in depth profile also support the conclusion that diffusion is taking place. Furthermore, there is a difference in the results when the temperature changes from 250 °C to 300 °C. After heat treatment at the

lower temperatures, the depth profiles do not change with time or temperature except for the initial difference upon heat treatment. At the higher heat treatments (>250 °C) the depth profile does change with time and temperature.

Anneal Time, hours	Anneal Temperature, °C	Nickel in Copper, %	Copper in Nickel, %
8	225	11.7	5.5
16		10.4	5.3
32		12.2	5.0
64		12.0	5.3
4	250	11.5	4.7
8		12.4	4.2
16		14.4	4.7
32		13.5	4.2
2	300	17.0	5.4
4		18.4	6.3
8		20.9	5.5
16		23.2	6.5
8	350	37.5	16*
1	400	44.6	15*
8		48.5	20*

Table 12: Diffusing Element Concentrations from AES, Copper on Nickel Structure
(* Estimate, concentration varies with depth).

4.4 X-RAY DIFFRACTION (XRD)

4.4.1 Copper on Nickel Structure

There are several peaks visible in the x-ray diffraction patterns of samples in their post deposition condition (Figure 35). The dominant peak is from the single crystal silicon substrate. It occurs at approximately 69 ° and corresponds to the silicon (100) plane. The remaining peaks appear in groups of two and represent the copper and nickel layers. The copper appears at the lower diffraction angle because its lattice parameter (3.6150 Å) is larger than that of nickel (3.5238 Å) [30]. The diffraction angle for the same plane is inversely proportional to the lattice parameter (Appendix III, Equation A3.3). The different diffraction peak pairs are from different lattice planes; (1 1 1), (200), and (3 1 1) are plainly visible, (222) is barely visible.

The average of the peak position measurements for copper, with hkl plane indices (1 1 1), is 43.396 °. For nickel, the measurements' average is 44.519 °. These results are in good agreement with the published values [30] for copper and nickel (respectively 43.298 ° and 44.508 °) Tables 13 and 14 compare the published positions [30] with the measurable positions in the diffraction patterns. The tables also show the measured peak widths and relative peak intensity. The grain sizes are from calculations using the diffraction peak positions and widths (Appendix III, Equation A3.4). The relative intensity measurements indicate that both the copper and nickel layers consist primarily of (1 1 1) grains. The average (1 1 1) particle size (from calculation) for the post deposition condition is 212 Å for copper and 144 Å for nickel.

Position, °2θ	hkl	Relative Intensity	Measured Position, °2θ	FWHM, °2θ	Measured Rel. Intensity	Grain Size, Å
43.298	111	100	43.409	0.4026	100	212
50.434	200	46	50.594	0.8719	13	101
89.934	311	17	90.283	0.8266	6	136
95.143	222	5	95.538	1.1466	2	103

Table 13. As Deposit Copper Peak Identification for Copper on Nickel

Position, °2θ	hkl	Relative Intensity	Measured Position, °2θ	FWHM, °2θ	Measured Rel. Intensity	Grain Size, Å
44.508	111	100	44.519	0.5944	100	144
51.847	200	42	51.996	0.8367	11	106
92.947	311	20	92.996	1.2084	4	96
98.449	222	7	98.662	0.8852	3	138

Table 14: As Deposit Nickel Peak Identification for Copper on Nickel

Figure 36 is an overlay plot of several diffraction patterns for the same heat treatment time (8 hours) but from different temperatures. The plot shows the (111) and (200) peaks of both copper and nickel. As the heat treatment temperature increases, from 225 °C to 400 °C, there is a slight change in the position of the copper peaks; the diffraction angle increases with the heat treatment temperature. Although Figure 36 only shows the (111) and (200) diffraction peaks, the same apparent increase in position occurs for all the copper peaks. Except possibly at the highest heat treatment temperatures, the positions of the nickel peaks in this structure are constant.

When the sample heat treatment is at 350 °C or above, a third peak appears in the diffraction patterns. Its position is between the diffraction angles of copper and nickel. It is

still possible to discern the original diffraction peaks for copper and nickel in most of the diffraction measurements. Tables 15 and 16 are surveys of the changes due to heat treatment on the (111) peak positions and widths for copper and nickel, respectively. The tables also include calculations of average grain size (Appendix III, Equation A3.4). There were no determinations of uncertainties in the grain size calculations for this experiment.

Anneal Time, hours	**Anneal Temperature, °C**	**Peak Position, °**	**Peak Width, °**	**Grain Size, Å**
N/A	Post Deposition	43.409	0.4026	212
8	225	43.424	0.3314	258
16		43.470	0.3207	267
32		43.482	0.3186	268
64		43.480	0.3415	250
4	250	43.469	0.3330	257
8		43.496	0.3085	277
16		43.501	0.3284	260
32		43.470	0.3303	259
2	300	43.413	0.5366	159
4		43.567	0.3455	248
8		43.610	0.3664	234
16		43.605	0.4141	207
2	350	43.596	0.2918	293
8		43.583	0.3083	278
1	400	43.676	0.3183	269
8		43.735	0.4001	214

Table 15: XRD Changes with Heat Treatment, (111) Copper, Copper on Nickel Structure

The peak width changes may indicate either grain size differences, the onset of or variation in lattice strain, or a combination of both. Here the changes are strictly

interpreted as reflecting a change in grain size. Some inconsistencies exist in the 350 °C and 400 °C samples and may indicate lattice strain is also important.

Anneal Time, hours	Anneal Temperature, °C	Peak Position, °	Peak Width, °	Grain Size, Å
N/A	Post Deposition	44.519	0.5944	144
8	225	44.513	0.3590	239
16		44.551	0.3714	231
32		44.562	0.3580	240
64		44.564	0.3866	222
4	250	44.549	0.3665	234
8		44.568	0.3270	263
16		44.573	0.3451	249
32		44.534	0.3445	249
2	300	44.492	0.3339	257
4		44 594	0.3352	256
8		44.593	0.3253	264
16		44.560	0.3171	271
2	350	44.578	0.2902	296
8		44.578	0.3149	273
1	400	44.613	0.2334	368
8		44.584	0.2127	404

Table 16: XRD Changes with Heat Treatment, (111) Nickel, Copper on Nickel Structure

4.4.2 Nickel on Copper Structure

In comparison with the copper on nickel structure, there are some small differences in the diffraction patterns of the nickel on copper deposition sequence. The diffraction patterns for different temperatures are shown in Figure 37. The nickel grain size is larger in the as deposit condition when nickel forms the overlayer (Tables 14 and 18). However, after heat treatment, there is very little difference in the

grain size of nickel between each deposition sequence (Tables 16 and 20). For copper, the diffraction patterns show that grain size is similar in the post deposition condition for both deposition sequences (Tables 13 and 17). However, the apparent grain growth is larger (Tables 15 and 19) for all heat treatment conditions when copper is the underlayer material.

Position, °2θ	hkl	Relative Intensity	Measured Position, °2θ	FWHM, °2θ	Measured Rel. Intensity	Grain Size, Å
43.298	111	100	43.365	0.4137	100	207
50.434	200	46	50.452	0.7209	15	122
89.934	311	17	90.074	0.8985	3	125

Table 17: As Deposit Copper Peak Identification for Nickel on Copper

Position, °2θ	hkl	Relative Intensity	Measured Position, °2θ	FWHM, °2θ	Measured Rel. Intensity	Grain Size, Å
44.508	111	100	44.521	0.4053	100	212
51.847	200	42	51.924	0.6641	15	133
92.947	311	20	93.011	0.9904	6	117

Table 18: As Deposit Nickel Peak Identification for Nickel on Copper

Regarding the appearance of new peaks, the same response to heat treatment of the copper on nickel structure occurs in the diffraction patterns for nickel on copper. At the higher heat treatment temperatures (350 °C and 400 °C), a diffraction peak appears between the diffraction angles of the individual element peaks (Figure 37). The pattern for the 400 °C heat treatment sample clearly shows three peaks. Tables 19 and 20 contain the diffraction data for heat treatments on this deposition sequence.

Although the peaks of heat treatment samples are close to their positions in the post deposition condition, the data clearly show a shift to one side. That is, all the copper and nickel peak positions are generally at a higher angle after heat treatment. This is particularly apparent after comparing the measurement results of the parent (post deposition) sample with its heat treatment samples (the part of the wafer broken off for processing). This indicates possible strain and/or stress relief.

Anneal Time, hours	Anneal Temperature, °C	Peak Position, °	Peak Width, °	Grain Size, Å
N/A	Post Deposition	43.365	0.4137	207
8	225	43.476	0.2507	341
16		43.478	0.2578	332
32		43.350	0.2602	329
64		43.467	0.2628	325
4	250	43.474	0.2554	335
8		43.471	0.2542	336
16		43.471	0.2568	333
32		43.465	0.2585	331
2	300	43.367	0.2575	332
4		43.505	0.2659	322
8		43.366	0.2626	326
16		43.497	0.2792	306
1	350	43.493	0.2477	345
2		43.482	0.2388	358
4		43.496	0.2647	323
8		43.496	0.2469	346
1	400	43.342	0.2464	347
8		43.424	0.3065	279

Table 19: XRD Changes with Heat Treatment, (111) Copper, Nickel on Copper Structure

Anneal Time, hours	Anneal Temperature, °C	Peak Position, °	Peak Width, °	Grain Size, Å
N/A	Post Deposition	44.521	0.4053	212
8	225	44.578	0.3655	235
16		44.576	0.3755	229
32		44.438	0.3758	228
64		44.563	0.3639	236
4	250	44.577	0.3840	224
8		44.567	0.3651	235
16		44.565	0.3793	226
32		44.557	0.3803	226
2	300	44.469	0.3496	245
4		44.589	0.3760	228
8		44.443	0.3677	233
16		44.571	0.3861	222
1	350	44.565	0.3700	232
2		44.566	0.3654	235
4		44.540	0.3977	216
8		44.568	0.3440	250
1	400	44.417	0.2637	325
8		44.444	0.1118	768

Table 20: XRD Changes with Heat Treatment, (111) Nickel, Nickel on Copper Structure

4.4.3 Summary of XRD Measurements

For samples after heat treatment at 225 °C and 250 °C there are only slight changes in the diffraction patterns. A third peak appears between the copper and nickel peaks when the heat treatment is at 350 °C and 400 °C. From 250 °C to 350 °C the differences in the diffraction patterns, versus the post deposition condition, become more pronounced. There is no significant difference between the behavior of different deposition sequences. The XRD results confirm the occurrence of mass transport between the layers and a new diffusion peak indicates an alloy phase.

4.5 FIGURES

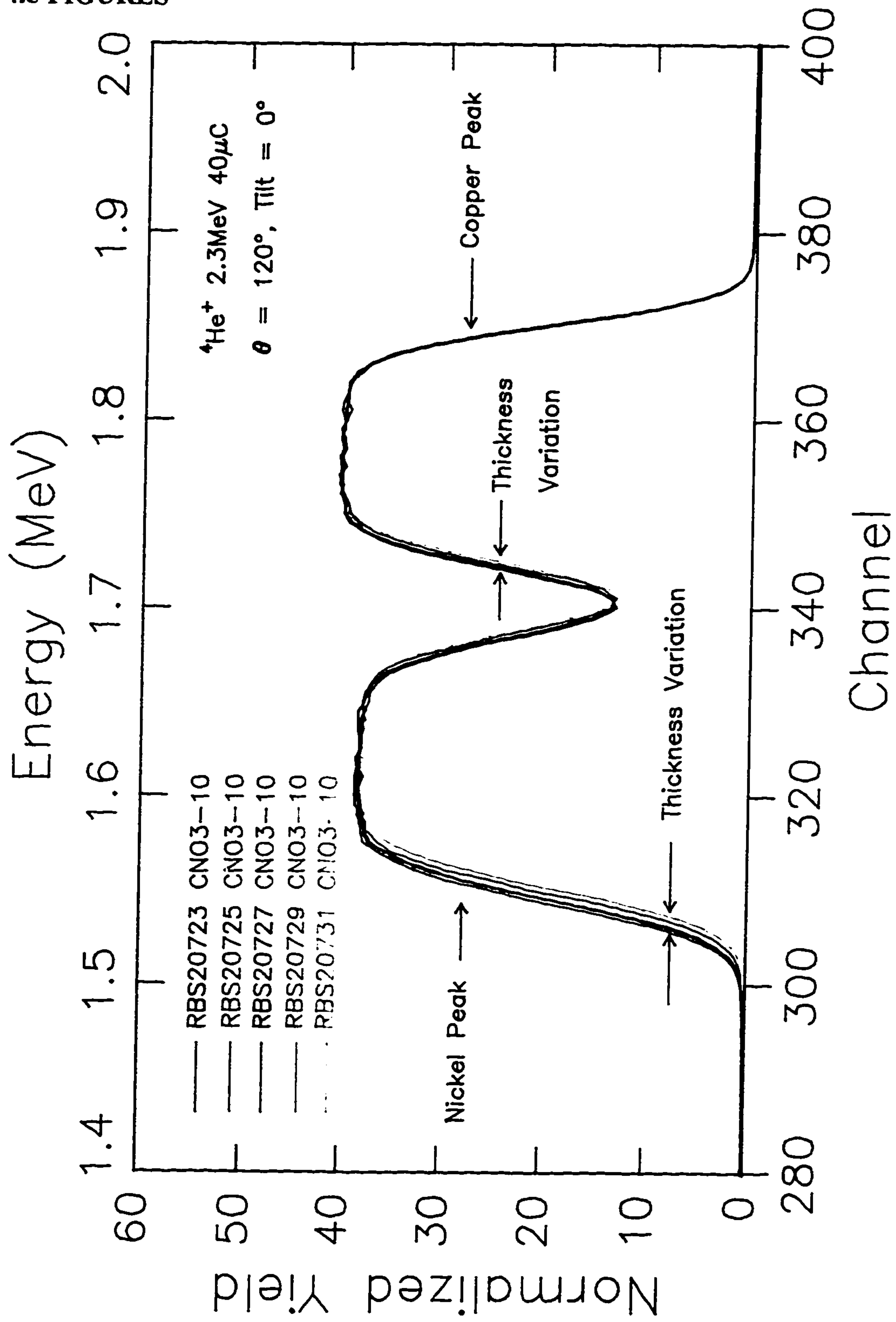

Figure 16: RBS Measurement of Thickness Variation Across a Sample

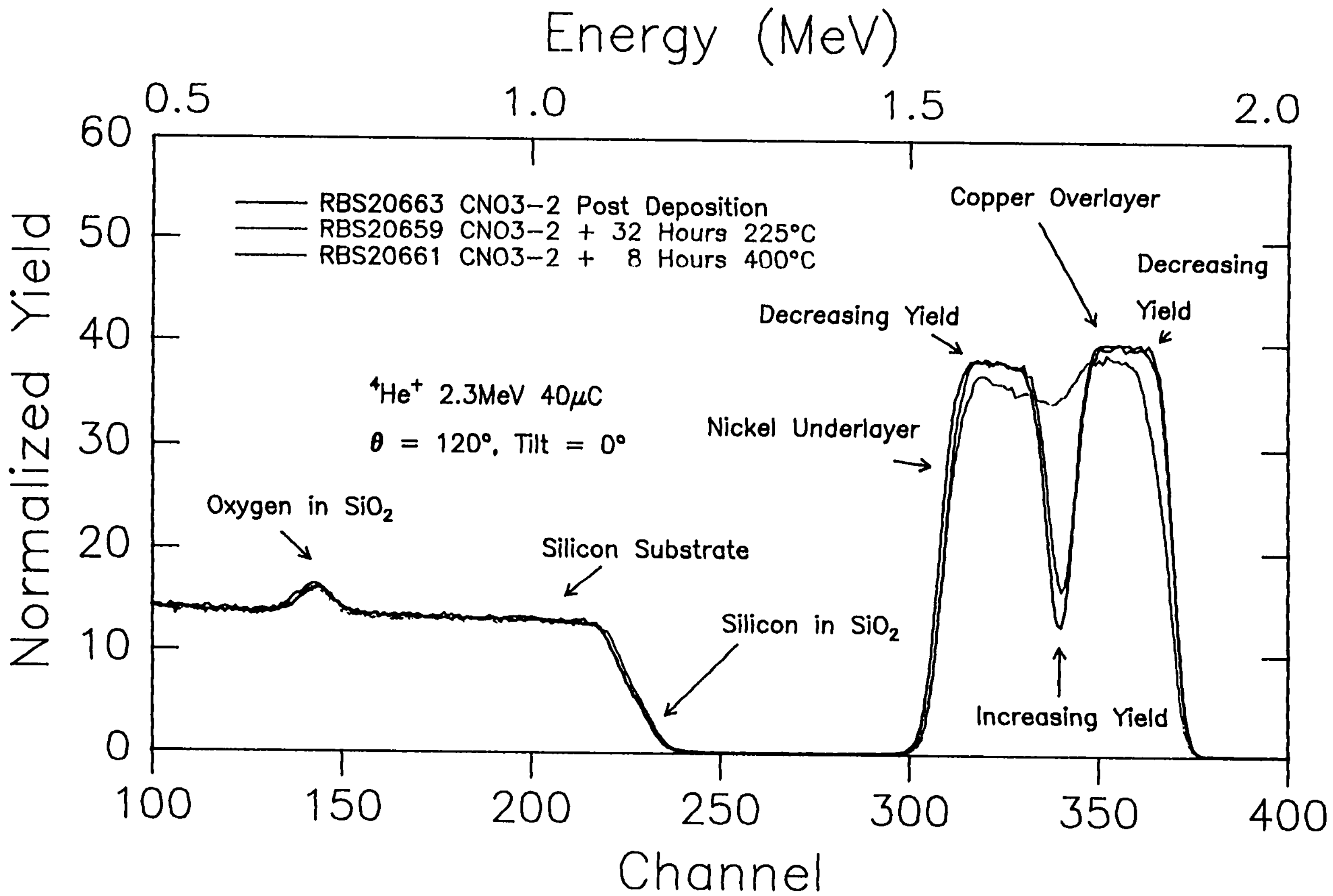

Figure 17: RBS Measurement Showing Yield Increase for Copper on Nickel

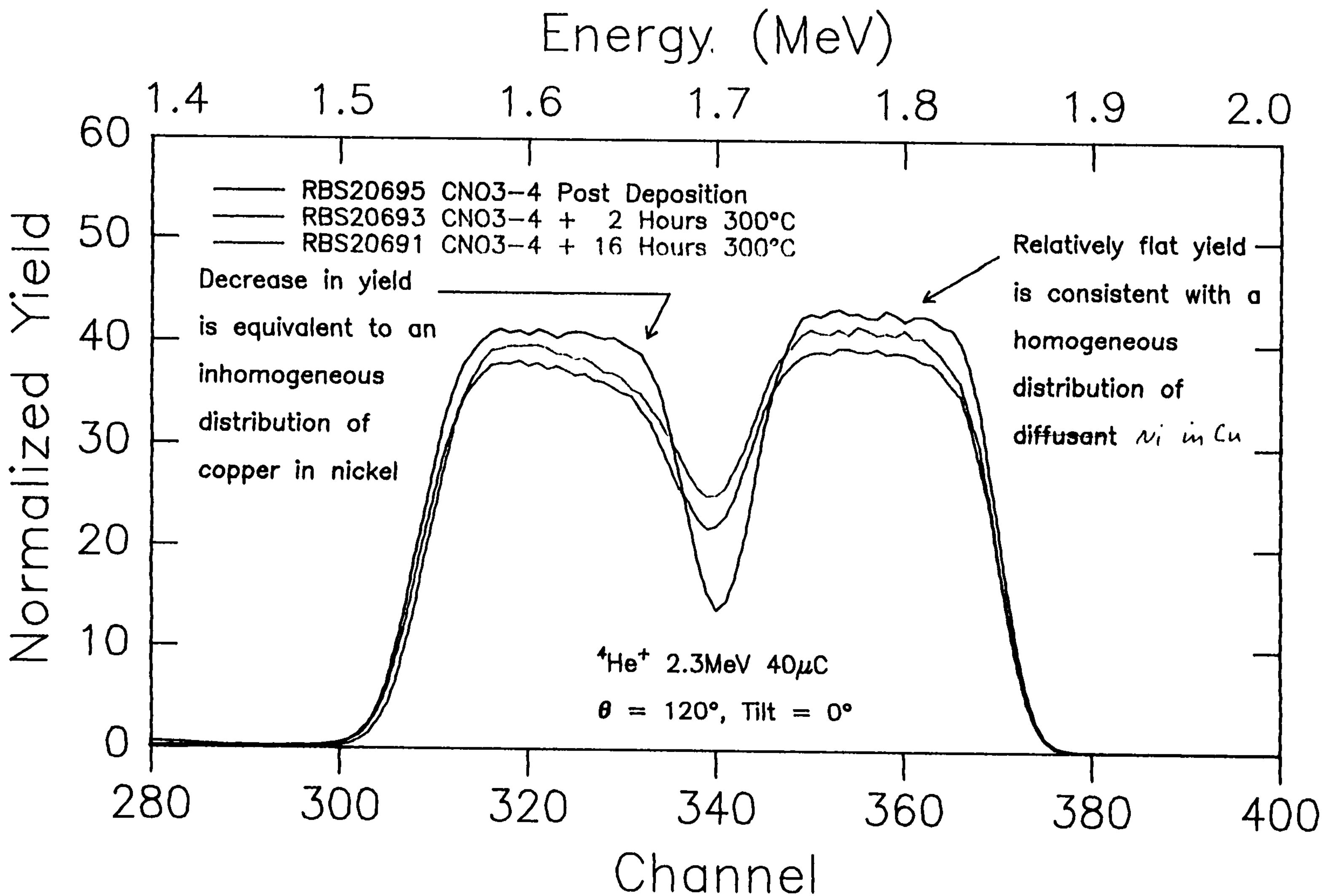

Figure 18: RBS Measurement Showing Inhomogeneous Diffusion of Copper into Nickel

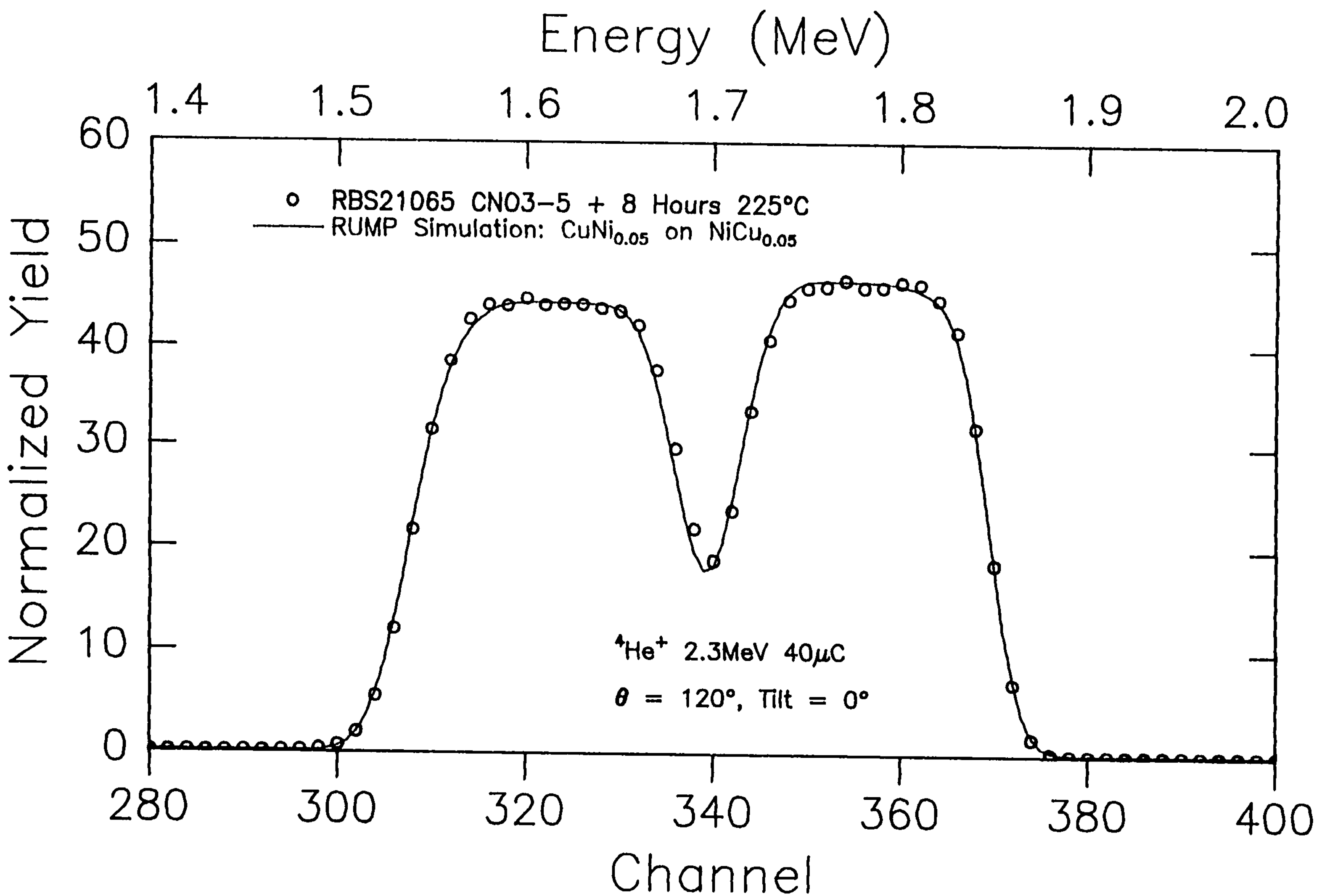

Figure 19: RBS Simulation of Measurement for Copper on Nickel, 225 °C

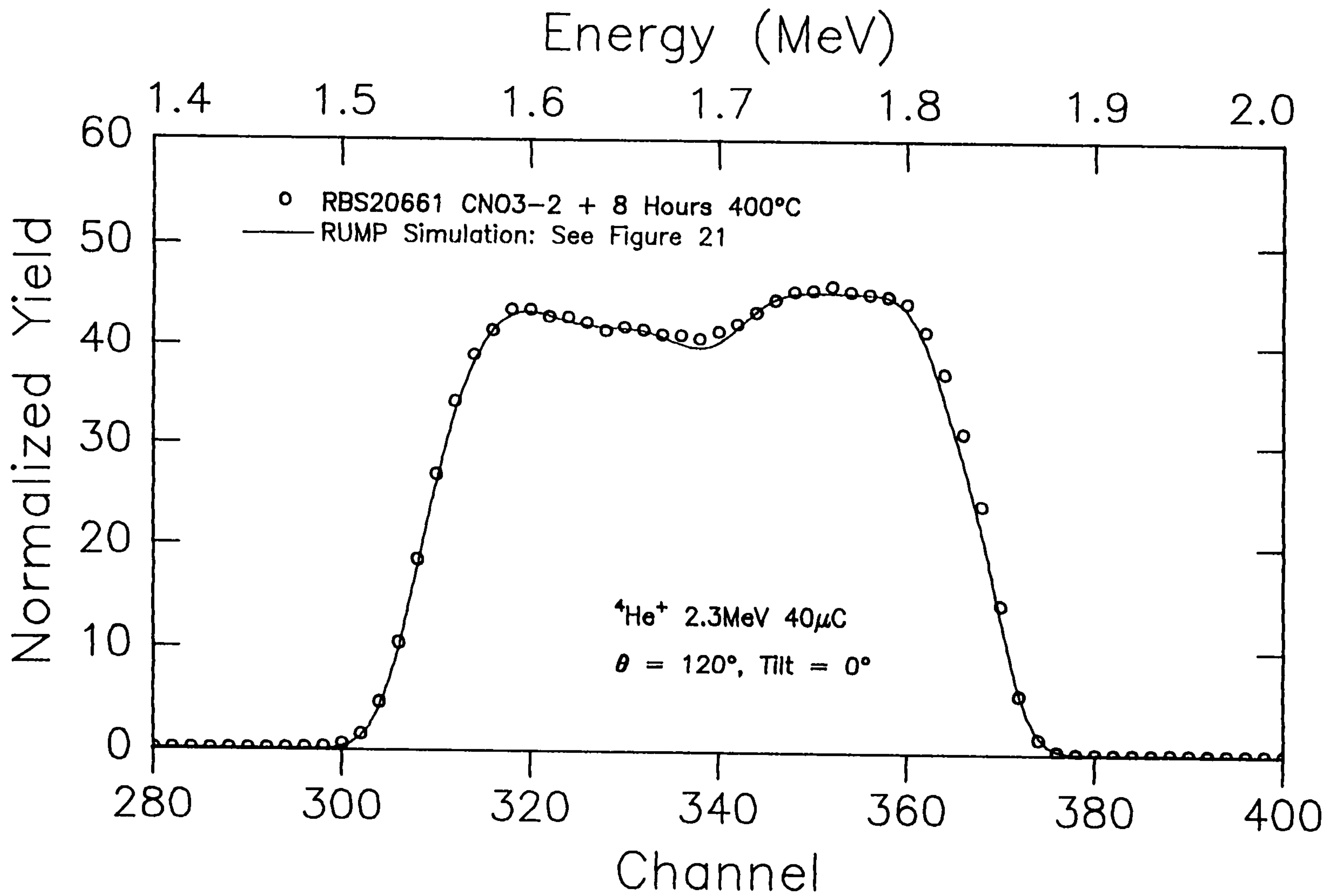

Figure 20: RBS Simulation of Measurement for Copper on Nickel, 400 °C

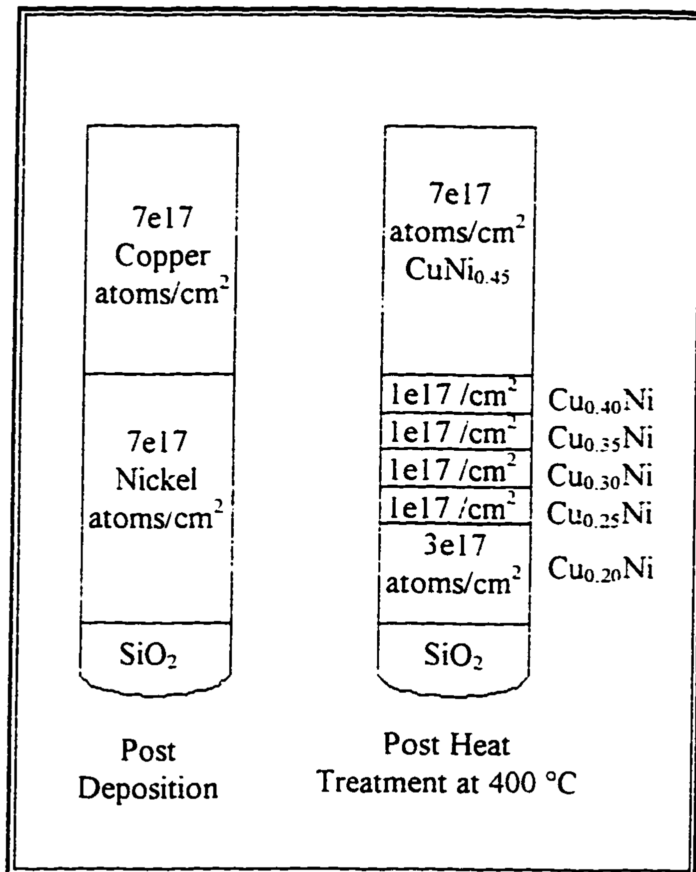

Figure 21: RBS Simulation Structure for Figure 20

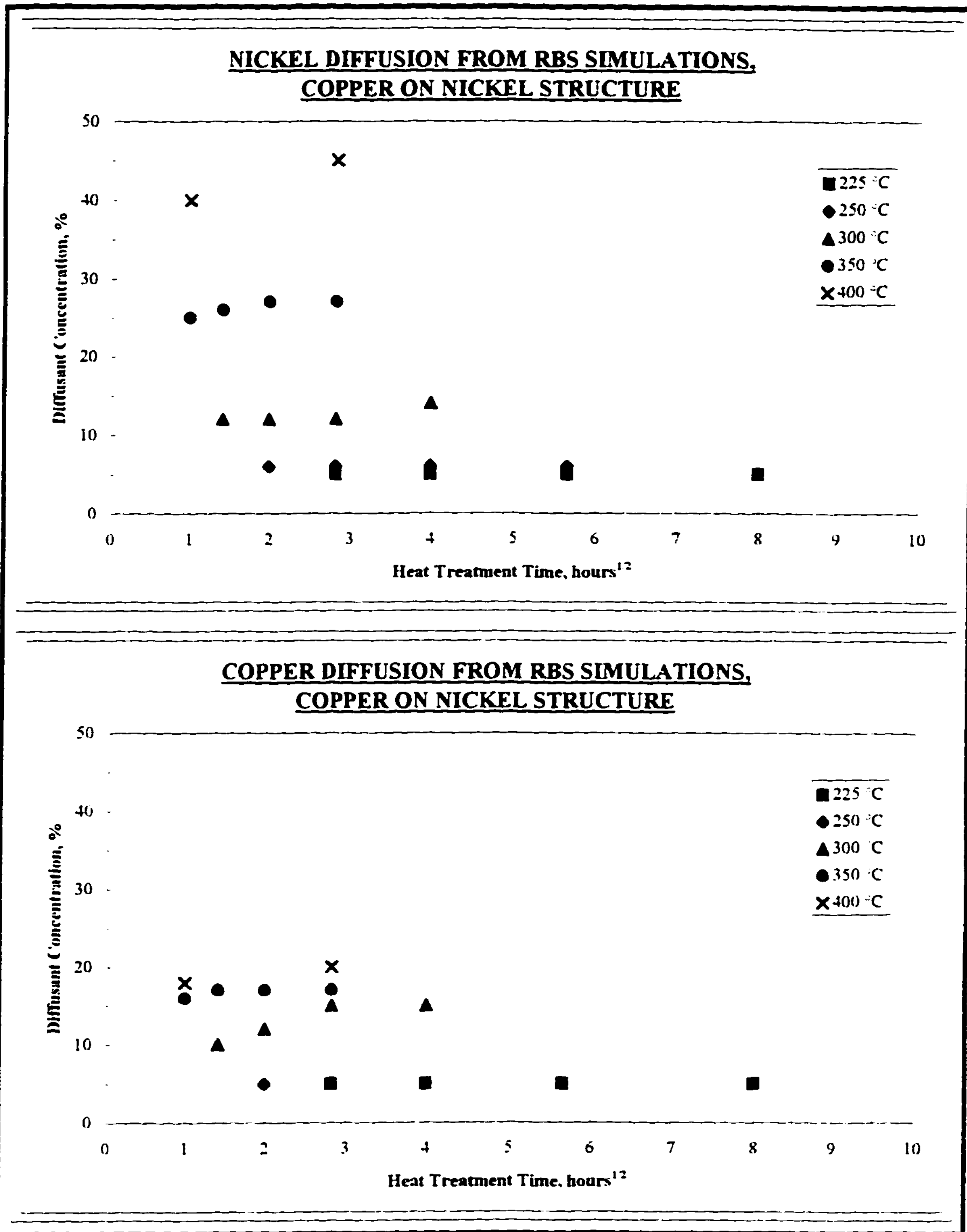

Figure 22: Diffusant Concentrations from RBS Simulations of Copper on Nickel

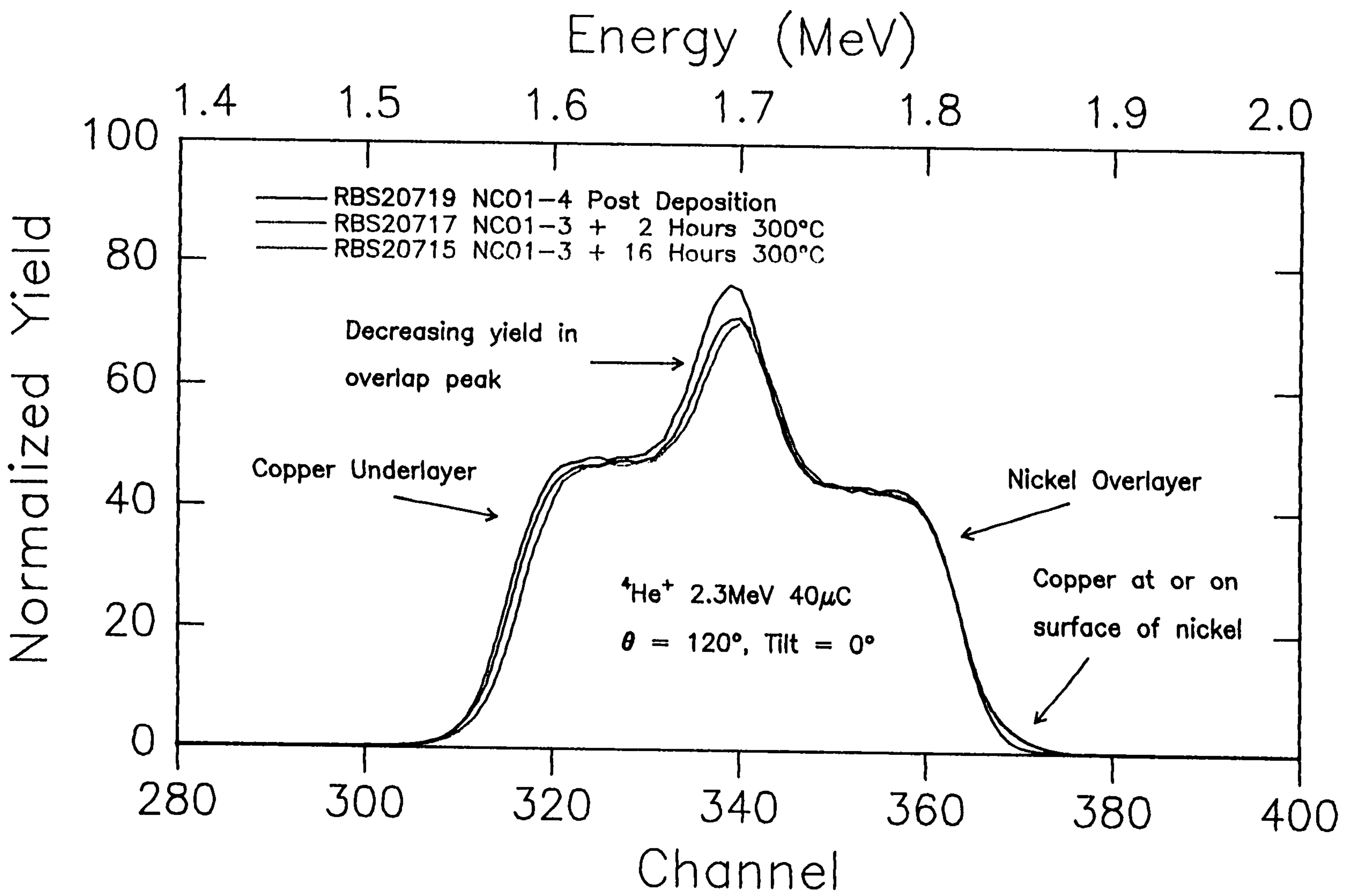

Figure 23: RBS Simulation Showing Yield Decrease for Nickel on Copper

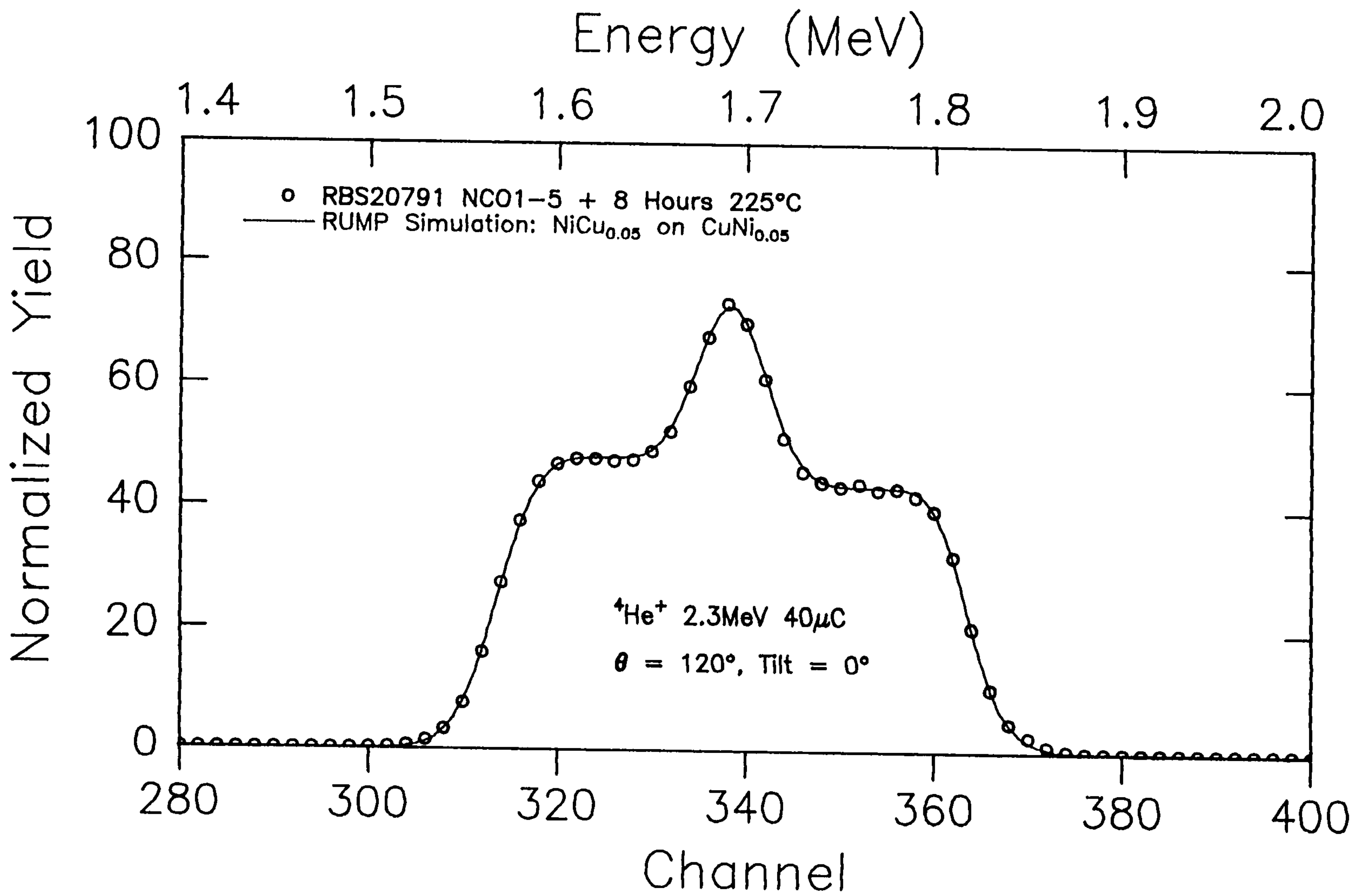

Figure 24: RBS Simulation of Measurement for Nickel on Copper, 225 °C

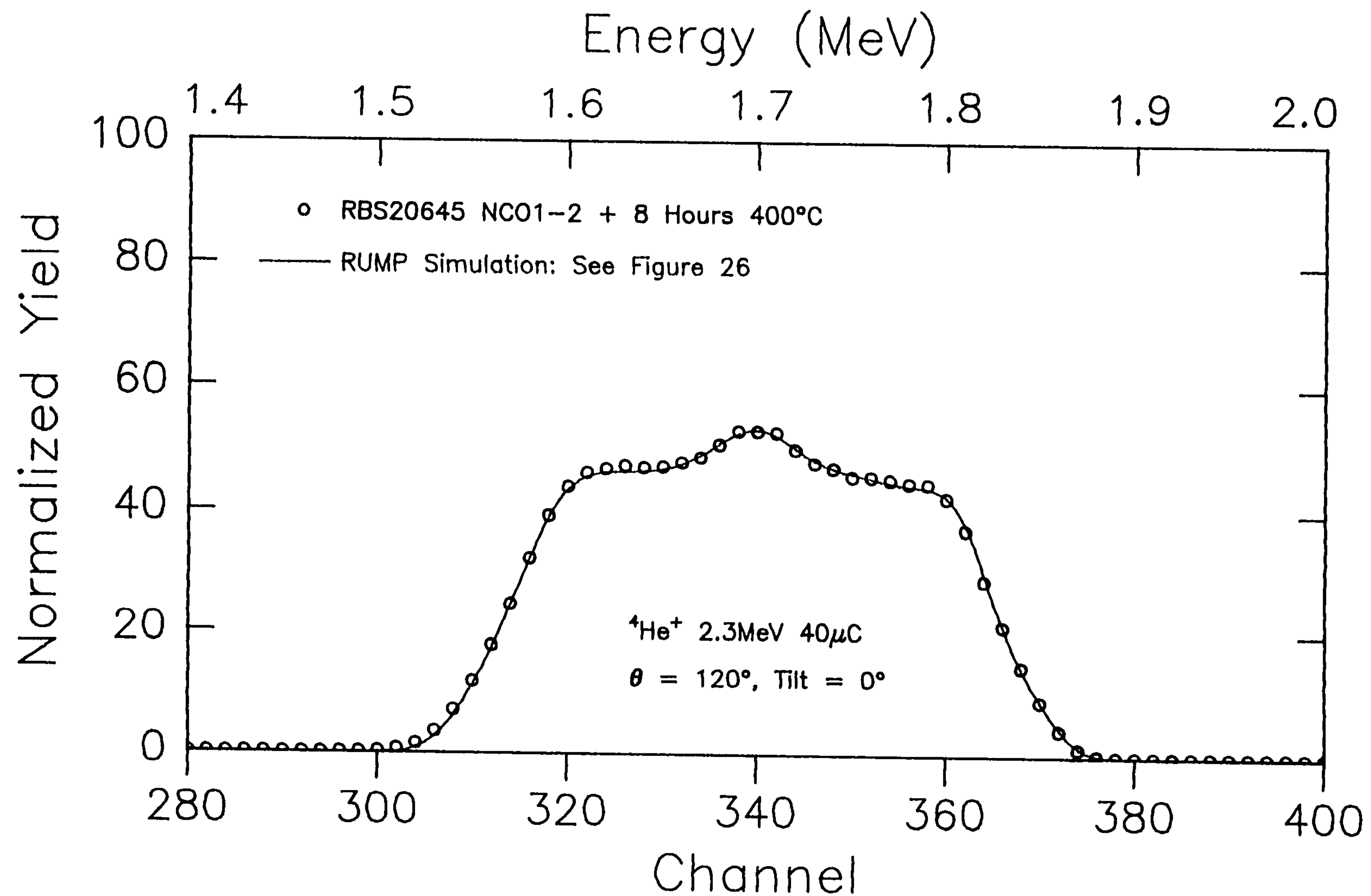

Figure 25: RBS Simulation of Measurement for Nickel on Copper, 400 °C

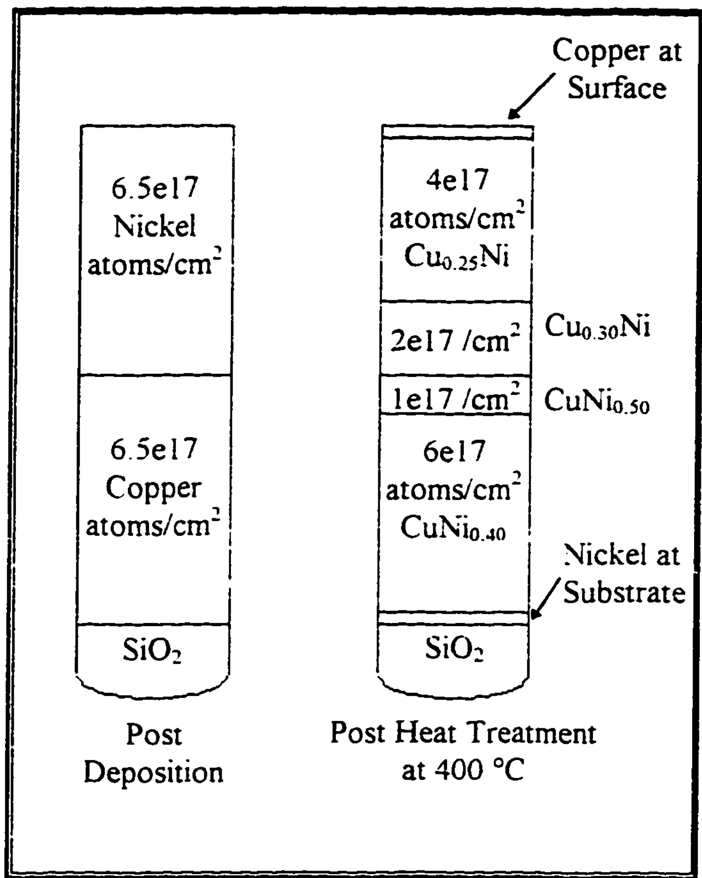

Figure 26: RBS Simulation Structure for Figure 25

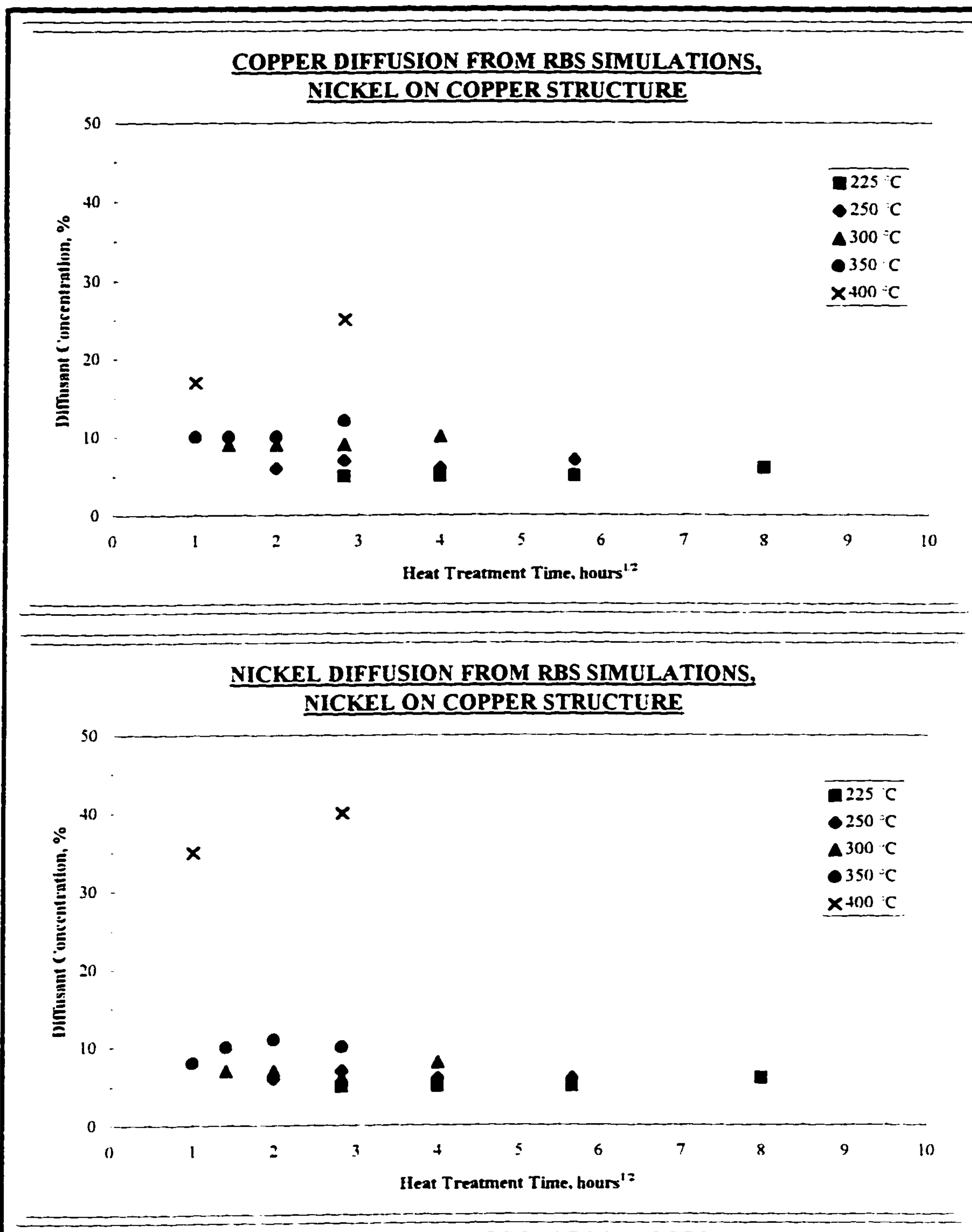

Figure 27: Diffusant Concentrations from RBS Simulations of Nickel on Copper

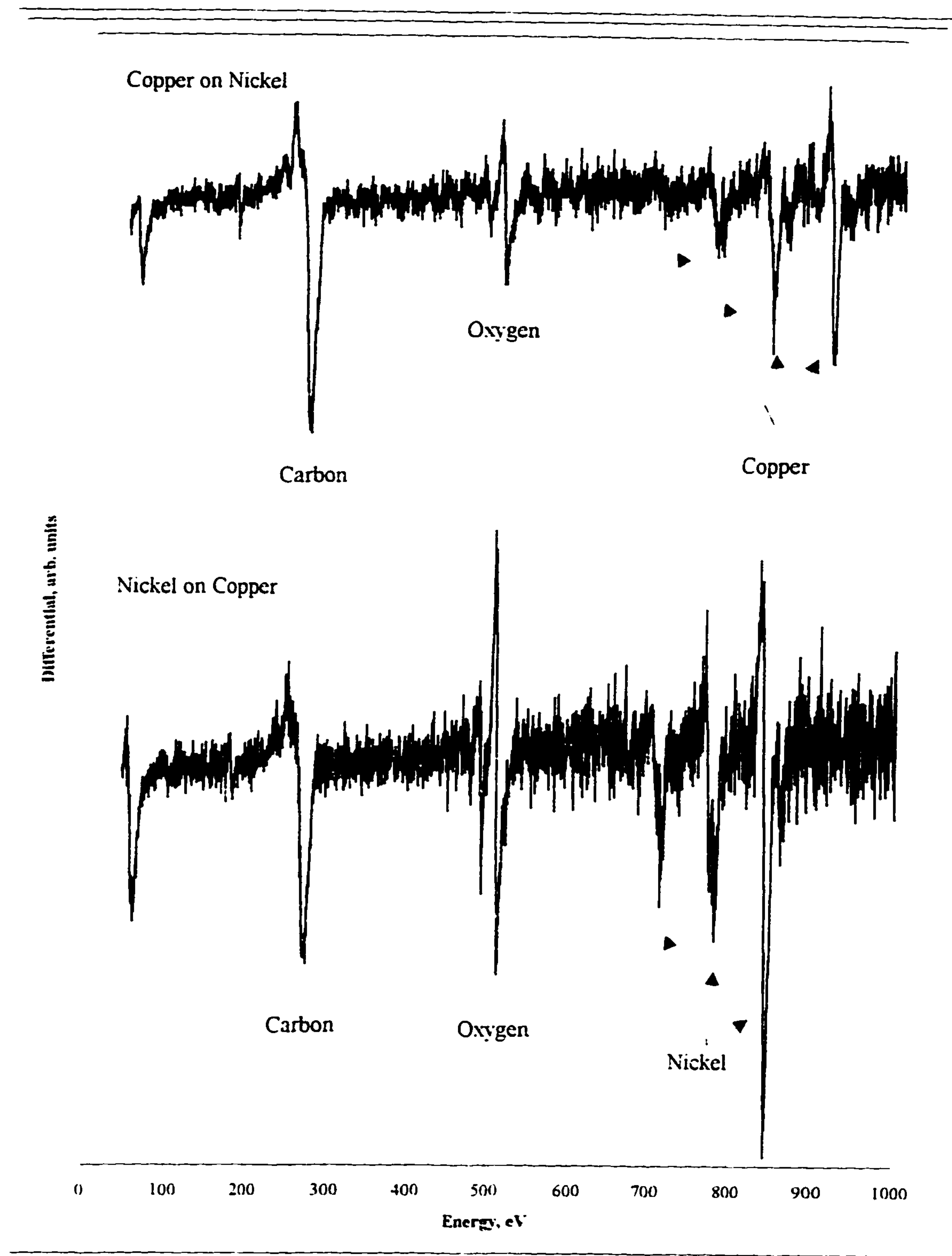

Figure 28 AES Surface Survey for Copper Nickel Bilayers Post Deposition

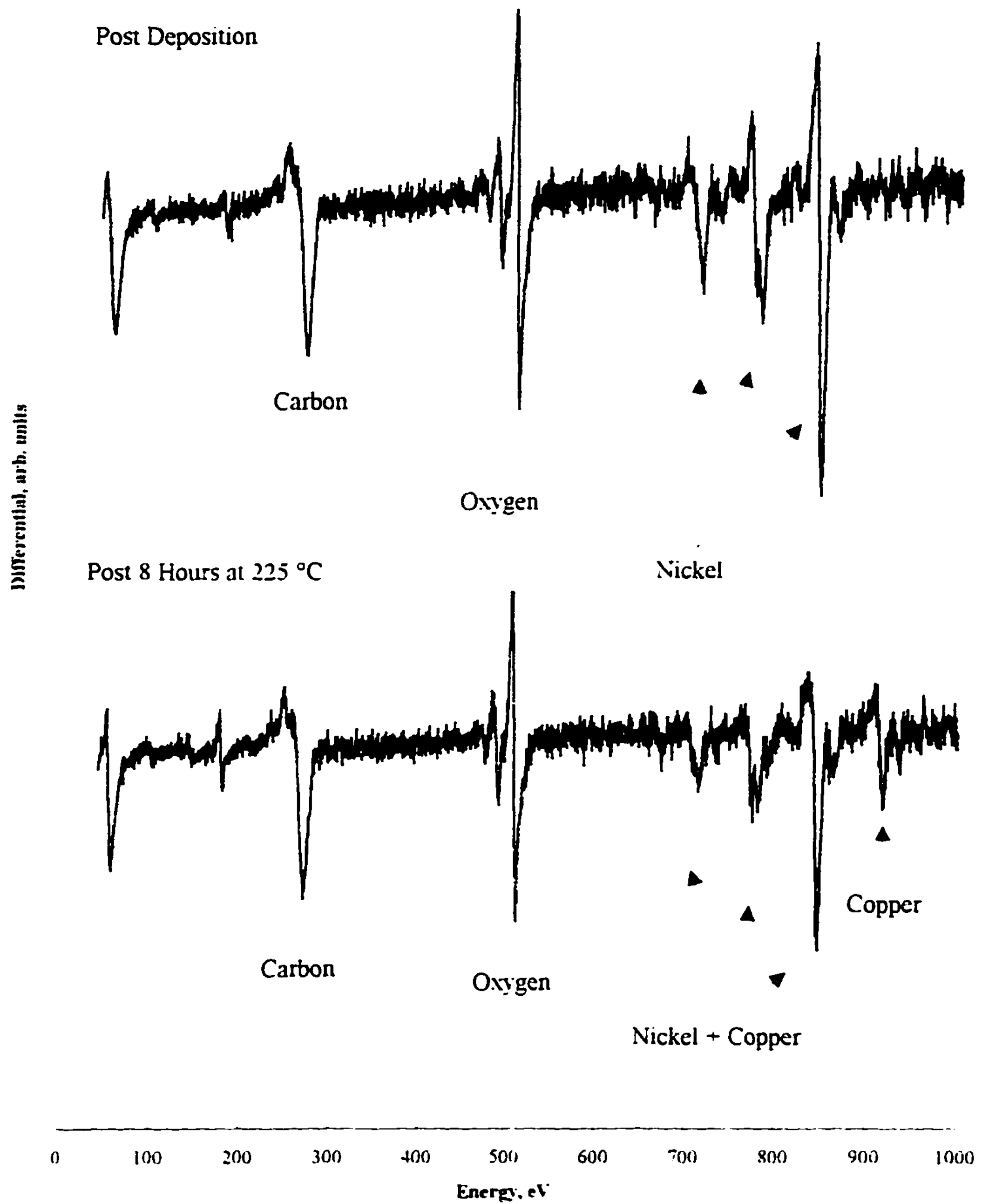

Figure 29: AES Overlay for Nickel on Copper Before and After Heat Treatment

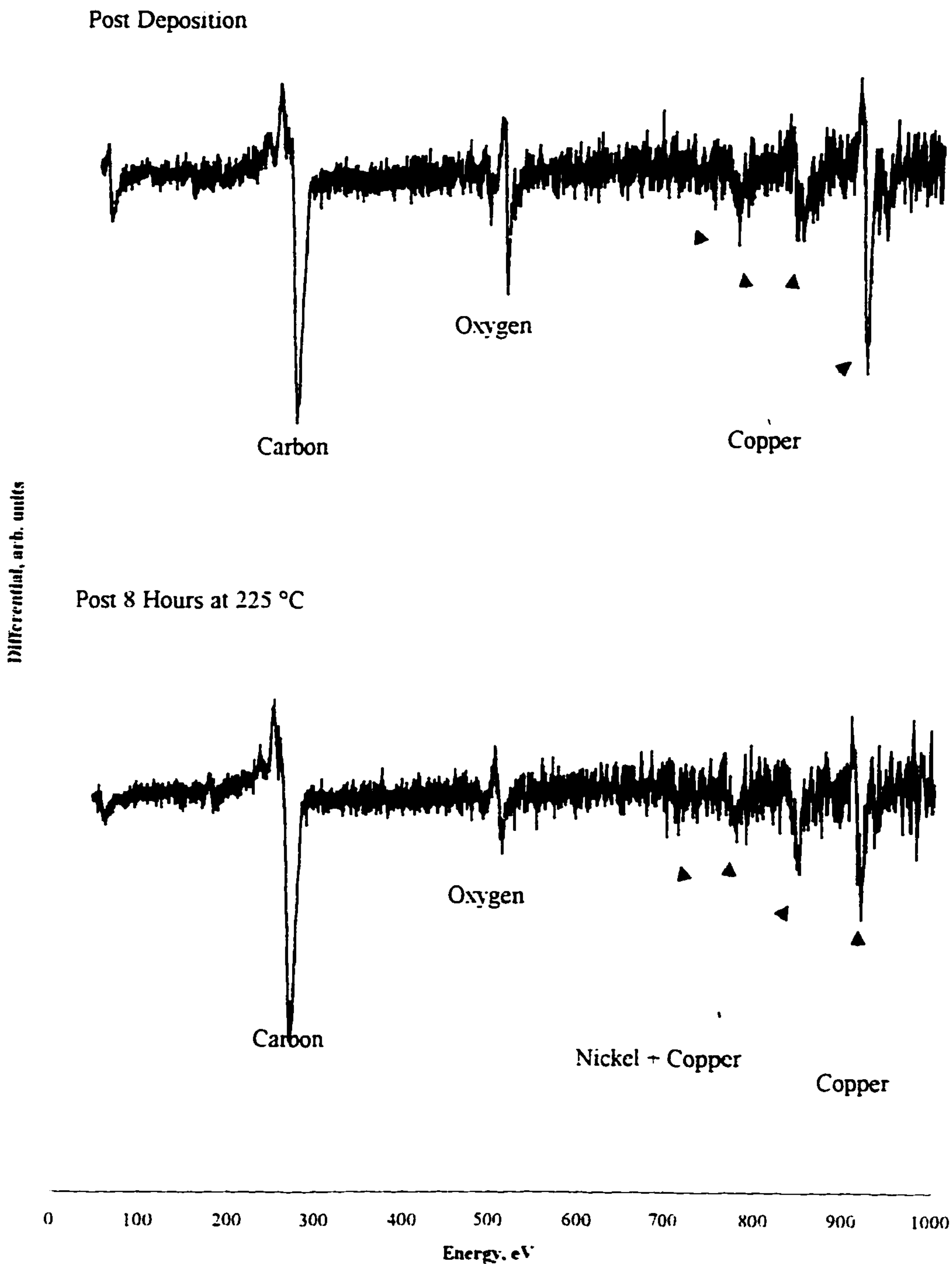

Figure 30: AES Overlay for Copper on Nickel Before and After Heat Treatment

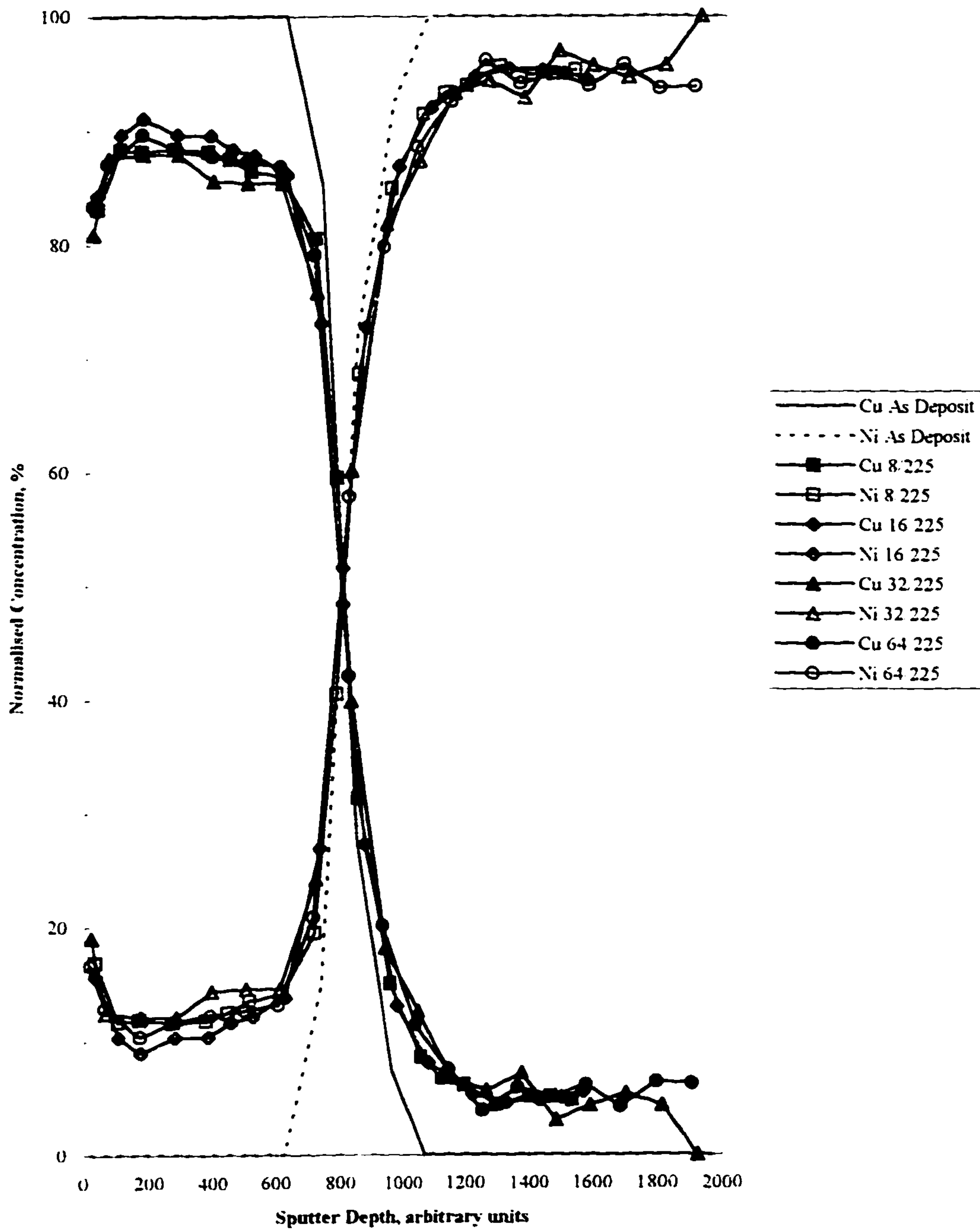

Figure 31: AES Depth Profiles for 225 °C Heat Treatment

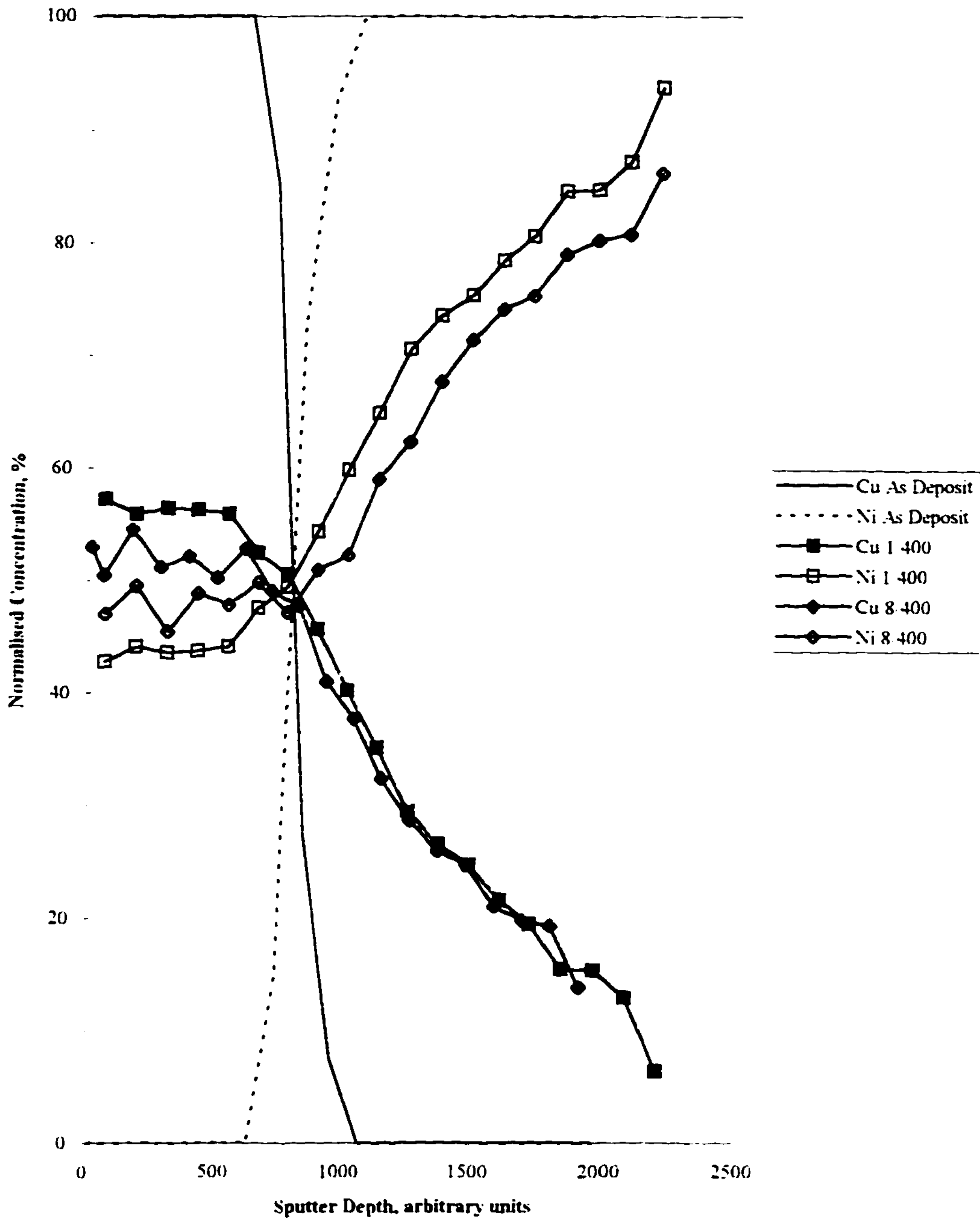

Figure 32: AES Depth Profiles for 400 °C Heat Treatment

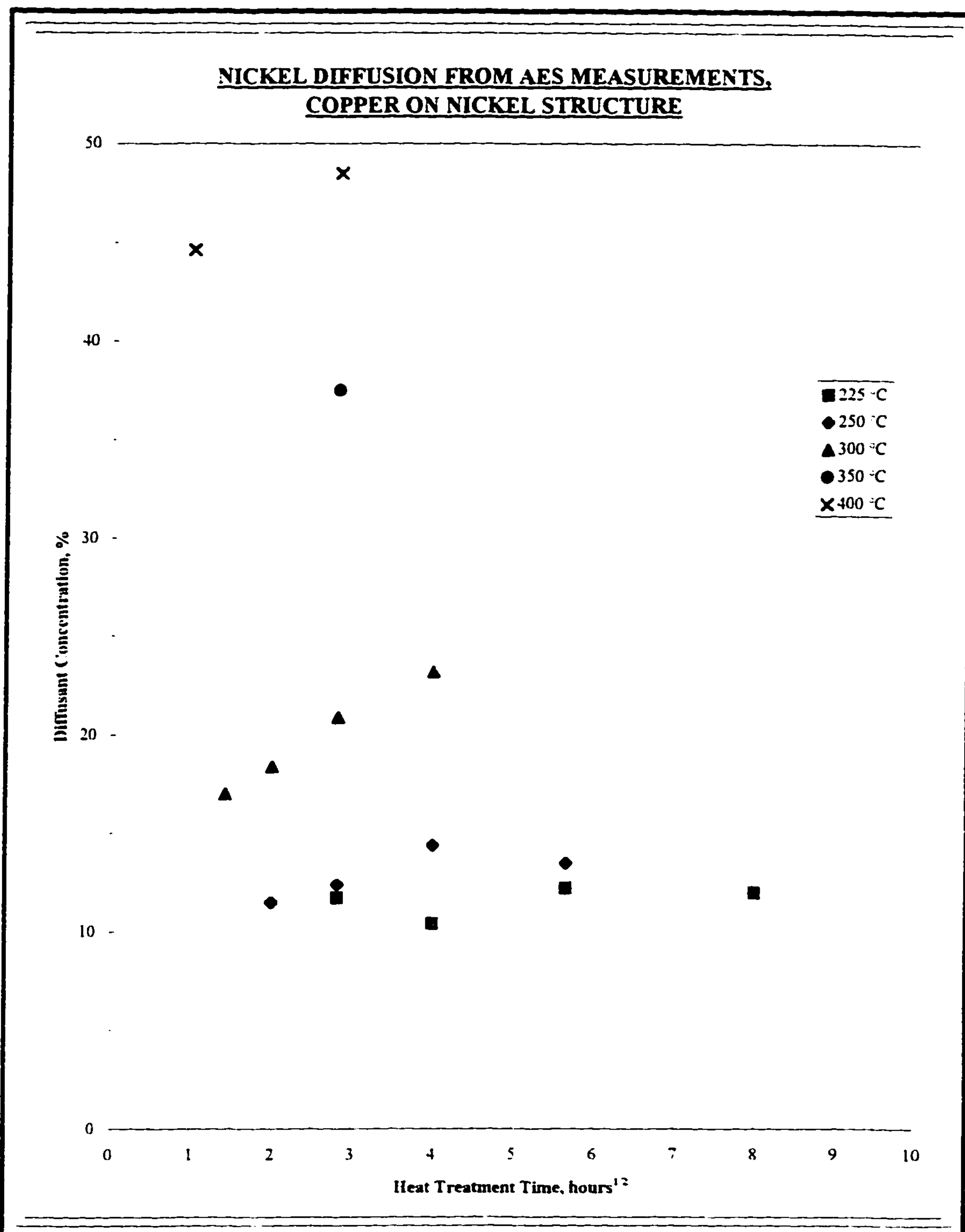

Figure 33: Nickel Concentrations from AES Measurements for Copper into Nickel

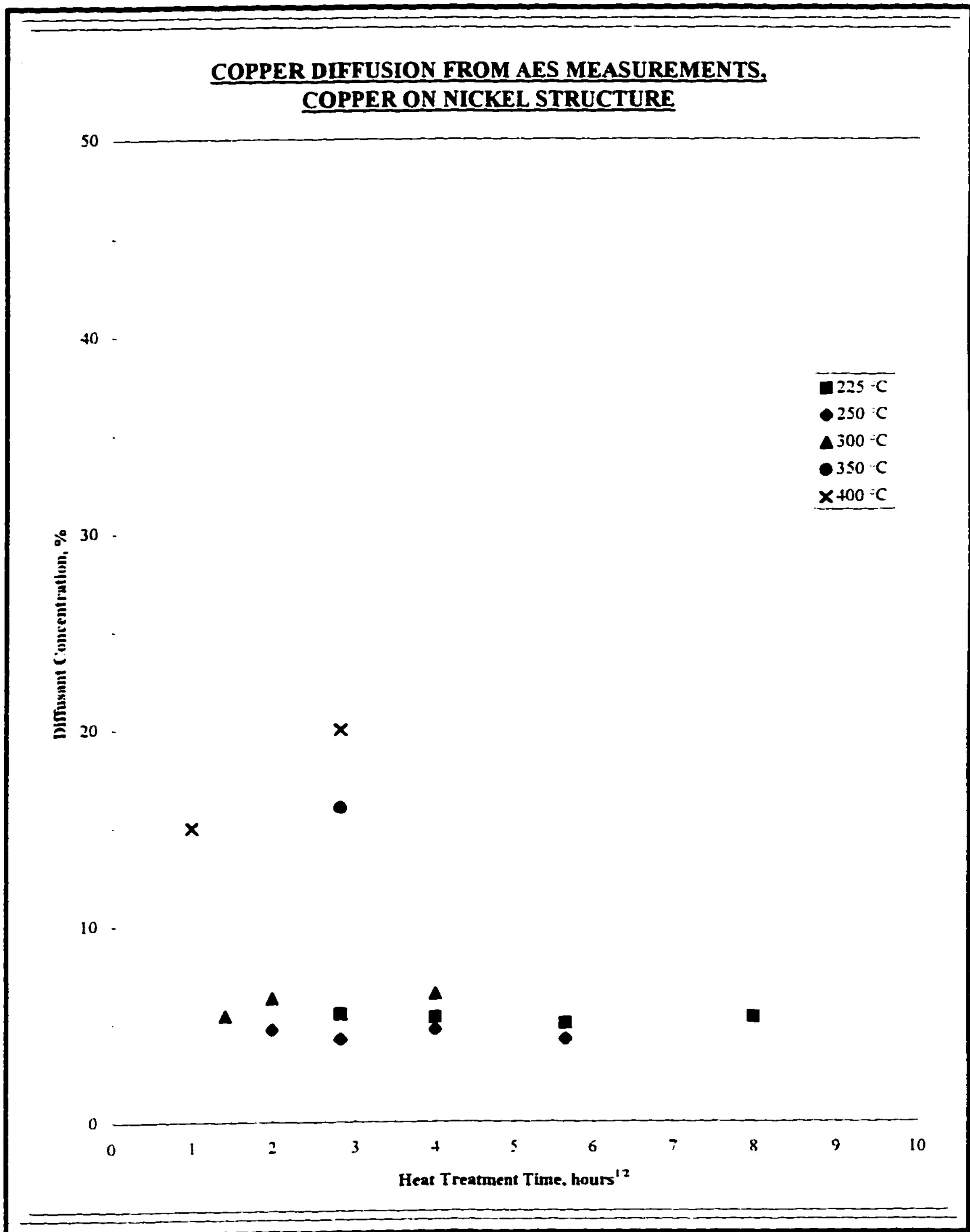

Figure 34: Copper Concentrations from AES Measurements for Copper nto Nickel

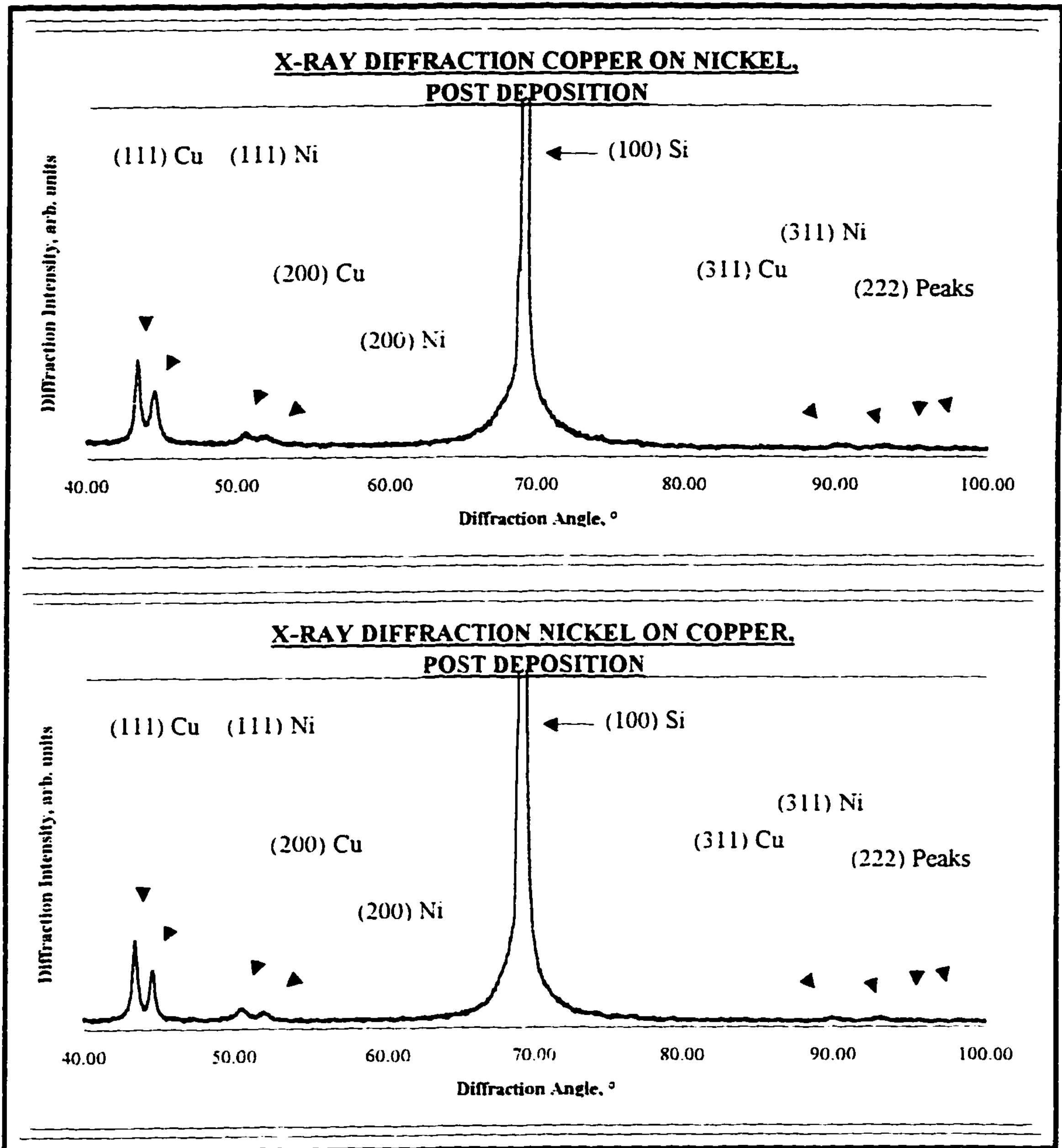

Figure 35: X-Ray Diffraction Patterns for Post Deposition Samples

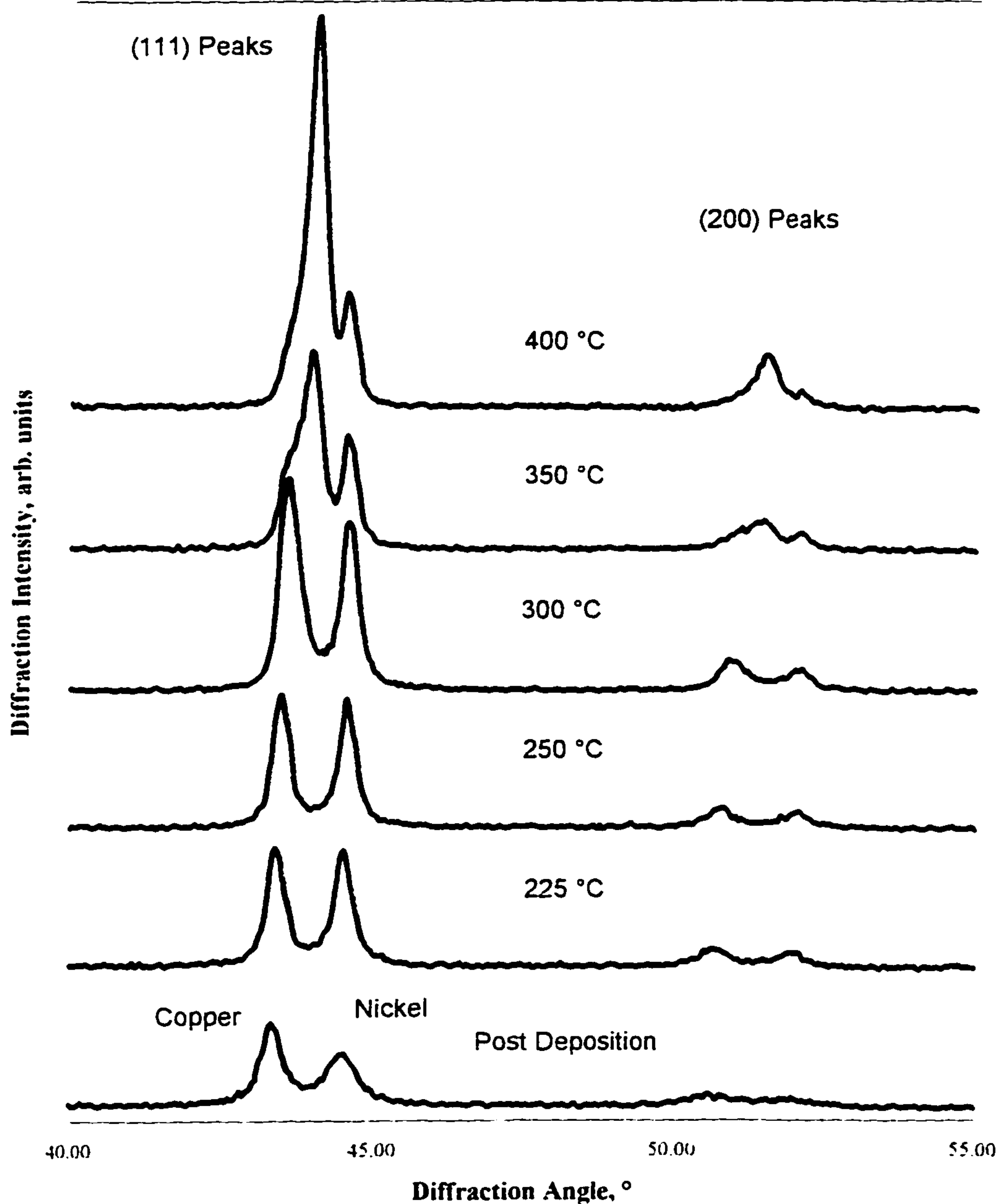

Figure 36: XRD Pattern Overlay for 8 Hour Heat Treatments, Copper on Nickel

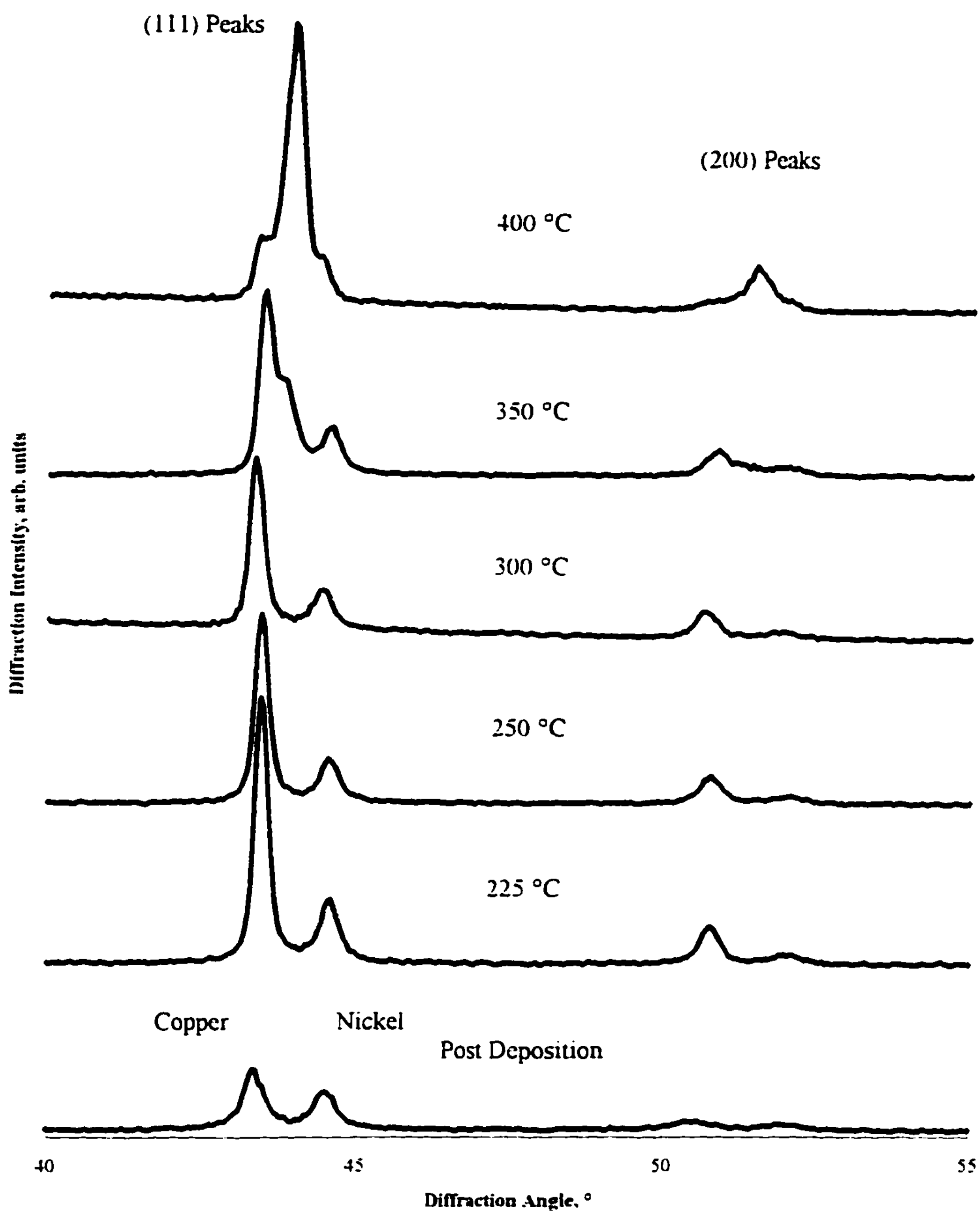

Figure 37: XRD Pattern Overlay for 8 Hour Heat Tretaments, Nickel on Copper

5.0 DISCUSSION

5.1 QUALITATIVE DESCRIPTION OF RESULTS

5.1.1 Mass Transport

The RBS and AES measurements clearly show mass transport occurs in both deposition sequences and that the diffusing elements are able to pass through the entire thin film structure thickness. The first evidence of the permeation distance is in the visual inspection of the copper on nickel structure. The change in the surface color, even at the lowest temperatures and shortest heat treatment times, supports the conclusion that nickel is reaching the surface and displacing copper atoms. It may also suggest that nickel is covering the surface of the copper film. The results from RBS extend the evidence that copper reaches the surface in the nickel on copper structure. The AES surveys also confirm in both deposition sequences that the underlayer element is present at the surface after heat treatment.

There are strong indications from the RBS results that nickel from an overlayer is able to diffuse through the copper underlayer. However, when copper is the overlayer material, the evidence that it is able to reach the oxide boundary is not strong. The RBS results are difficult to interpret with the variation in thickness of the films. AES typically shows a decreasing concentration gradient of copper into the nickel at the higher heat treatment temperatures (Figure 32). Since copper does diffuse through an overlayer nickel, there is a good probability that it also diffuses completely through the nickel underlayer of all samples

It is evident from the AES results that the heat treatment conditions span Type B and C diffusion kinetics (Figure 38). There is an initial concentration build up with heat treatment. However, there is no significant change in the diffusion profiles with time at 225 °C and 250 °C; the concentration of the diffusant reaches a constant level sometime before 8 hours at 225 °C. There are no observed changes until the 300 °C heat treatment conditions. This represents filling of boundaries by grain boundary diffusion at 250 °C and below. It applies to AES results of nickel in an overlayer copper and copper diffusing in the opposite direction. The RBS measurements tend to support this conclusion; there is very little difference between the back scattering spectra of the samples after heat treatment under the same low temperature conditions (Figure 39). The obvious difference is an initial change that takes place upon heat treatment. AES and RBS measurements of samples receiving heat treatments above 250 °C reveal continuous changes in the diffusion profiles with both time and temperature (Figures 38 and 40) and indicates intragrain lattice diffusion. Therefore, diffusion kinetics at the lower heat treatment temperatures of 225 °C and 250 °C appears to be Type C for both deposition sequences. The kinetic regime is Type B at temperatures of 350 °C and above. At 300 °C, RBS supports lattice diffusion for the copper on nickel structure, as does the AES result, but not necessarily for the opposite deposition sequence.

The AES measurements show that there is more nickel in the copper overlayer than copper in nickel following heat treatment at the lower temperatures (12 % versus 6 %, Table 12). This does not mean faster kinetics with only grain boundary diffusion.

Instead, the result suggests that there is more grain boundary volume in the copper overlayer. However, the RBS measurements do not generally support more diffusion of nickel than copper at the same temperatures. The best RBS measurements for comparison of this deposition sequence show a constant overlap back scattering energy between the copper and nickel peaks (Figure 41). From RBS simulations, the fixed energy position indicates equivalent amounts of diffusion in both directions. Therefore, there is more evidence suggesting that the nickel in copper concentration from AES depth profiling is in error. A possible explanation for this may occur in the algorithm to remove the overlap between copper and nickel. More discussion of this appears in a later section.

When nickel is the overlayer material, the RBS measurements attest to similar diffusion kinetics for both elements if the heat treatment is under 300 °C. At the higher temperatures of 350 °C and 400 °C the diffusion of nickel is definitely faster than for copper in both deposition sequences (Tables 10, 11, 12).

5.1.2 X-Ray Diffraction

There is an initial change in the positions and widths of the copper and nickel x-ray diffraction peaks that occurs upon heat treatment. However, the diffraction patterns show only slight changes with time in the position of the copper peak, for heat treatments below 300 °C, and very little difference in the peak widths. Starting at 300 °C, changes in position and width are more noticeable. The position of the nickel peak remains constant up to the 400 °C heat treatment condition while its width starts to change at 300 °C. The

calculations from the XRD results show an initial change in the grain size upon heat treatment for both films. However, the dimensions of the grains do not appear to change with heat treatment condition (Figure 42) until the temperature reaches 300 °C for copper and 400 °C for nickel. This coincides with the prominent shift in peak positions.

The x-ray diffraction peak positions depend on the lattice spacing and the average grain (particle) size. The peak widths in the diffraction patterns are a function of lattice strain and grain size. Therefore, both lattice strain and grain growth influence the grain size calculations from the XRD peak widths. The diffraction results clearly show a smaller grain size for samples in their as deposit condition regardless of the deposition sequence. They also indicate that, at least for temperatures less than 300 °C, there is very little change in grain size with heat treatment time and temperature. It is possible to deduce from this that the heat treatment provides some stress relief. This will account for the apparent initial change in the grain size (calculated from the as deposited peak widths). It also could explain the lack of further grain growth after heat treatment at longer times or higher temperatures. (There were no stress measurements in this investigation.)

There are complications if the heat treatment introduces inhomogeneous lattice strain. Support of lattice strain comes from the changes in peak positions after the high temperature heat treatments, combined with the RBS and AES evidence of lattice diffusion at these temperatures. For the temperatures where only grain boundary diffusion is in evidence, there is no lattice diffusion to distort the lattice. Therefore, the assumptions above indicate that no grain growth occurs at the lower heat treatment temperatures. It is

therefore possible that grain size calculations for samples with no heat treatment are erroneous because of an initial film stress (introduced in the deposition process).

The third diffraction peak appears in the patterns for higher temperature treatments; it is from an alloy of copper and nickel and is certainly consistent with mixing from lattice diffusion. It is not obvious, however, if the peak is the result of a gradual dilution from diffusion or the nucleation of an alloy phase. In many cases the alloy diffraction peak appears with copper and nickel peaks still plainly visible. The equilibrium phase diagram for copper nickel [7] shows a continuous range of alloys with complete solubility so a phase nucleation is unforeseen Therefore, as expected, the third peak represents a copper nickel alloy forming from lattice diffusion.

At 350 °C and above, diffraction peaks from copper and nickel could represent regions with little or no lattice diffusion. Their peak positions are only slightly different when the heat treatment is at lower temperatures. When the third peak appears in the diffraction patterns it is the nickel peak that remains obvious. This is consistent with the slower kinetics for copper diffusing in nickel leaving more of the nickel grains undiluted. However, it is also possible that inhomogeneous strain in the region where lattice diffusion does take place (the periphery of the grain) also puts stress on the undiluted grain core.

To summarize the x-ray diffraction results, there is good confidence that the grain size is steady for copper and nickel following heat treatments below 300 °C. If stress relief does account for the narrower peak widths then the calculated initial change in the grain dimension is possibly incorrect. It is logical to use the low temperature heat treatment

measurements to determine the initial grain size. At the higher heat treatment temperatures, lattice diffusion will introduce inhomogeneous strain that can confuse the results and calculations. Since there is also the third diffraction peak, it is difficult to make any convincing determination about grain size or growth when the heat treatment is above 250 °C. The presence of three peaks suggests that a portion of the grain volume, in both the copper and nickel layers, still exists in an undiluted condition. Diffusion into the grains starts from the grain boundary source. Therefore, there is a volume at the periphery of grains that has a varying concentration of the diffusing element. This in turn creates inhomogeneous lattice strain and stress on the core of the grain. Until lattice diffusion permeates the entire grain, the grain cores will remain pure.

5.2 DIFFUSION MODELS

The results for low temperature diffusion indicate that diffusion is only via grain boundaries with the solute completely penetrating through both films. The results at higher temperatures show changes in concentration gradients that indicate bulk lattice diffusion. If the grain boundaries are already filled, then mass transport into the grains is a process of penetration from the grain boundaries towards the center of the grain. The following models attempt to correlate the quantitative experimental results to a physical model.

5.2.1 Grain Boundary Volume Fraction

For a simple model of grain structure in a solid one can assume the grain boundary volume surrounds a spherical grain (Figure 43). The width of the grain boundary is δ. (Note that only $\delta/2$ associates with one grain while the other half associates with an adjacent grain.) The diameter of the grain is G and is much larger than the grain boundary width.

$$Volume\ of\ Grain = \frac{4}{3} \cdot \pi \cdot \frac{G^3}{8}$$

$$Surface\ Area\ of\ Grain = 4 \cdot \pi \cdot \frac{G^2}{4}$$

$$Volume\ of\ Grain\ Boundary = \pi \cdot G^2 \cdot \frac{\delta}{2}$$

$$\frac{Volume\ of\ Grain\ Boundary}{Volume\ of\ Grain} = \frac{3 \cdot \delta}{G}$$

The ratio $3 \cdot \delta / G$ is an approximate volume fraction of grain boundaries in a polycrystalline material that contains spherical grains. The same ratio applies if the shape of the grain is a cube and G is the length of the cube edge. In a system where mass transport takes place only along grain boundaries, the volume ratio can be used as an estimate of the maximum solute concentration once the grain boundaries are filled. It should be the same as the fractional atomic concentration of the diffusing species measured by AES or RBS. The concentrations are averages over a plane that is parallel to the film and intersects grains and grain boundaries. For a grain size of 250 Å and a boundary width of 5 Å, this model estimates a maximum solute concentration of 3 % by filling from grain boundary diffusion only.

The obvious limitation of this model for volume fraction of grain boundaries is that polycrystalline materials have a diversity of grain sizes and shapes. Also, there is not a great precision in the knowledge of grain boundary widths such that small differences are meaningful. For example, a difference of 1 Å to a 5 Å grain boundary width surrounding a 200 Å grain will change the volume ratio by approximately 20 %. Grain boundary widths themselves are not uniform and depend on the angle of the grain boundaries; low angle grain boundaries will have smaller widths. Another limitation is the existence of triple (or higher) points at the conjunction of multiple grains. These features have a larger capacity and less resistance to mass transport. Note that a grain boundary width of 5 Å is a

reasonable upper limit. This width is approximately two or three lattice planes. If it were larger then the grain boundary would start to resemble a hole.

Another drawback in the above model, to describe grain boundary diffusion, is in accounting for more than one mobile species in the grain boundaries. Grain boundary self-diffusion does take place so it is reasonable to expect that both elements will occupy the regions between grains. If no other elements are present in this experiment, the multiple elements are simply copper and nickel. Thus the observed diffusant concentration for grain boundary diffusion may be less than the volume ratio from this model.

5.2.2 Diffusion into a Sphere

Darken [31] discusses solutions to Fick's second law for diffusion in a sphere. One set of boundary conditions is for an initial concentration within the sphere (taken as zero in this experiment) and a constant surface concentration (in the boundary). A first order analysis will use a surface (grain boundary) concentration of 100 % but this is not necessarily the case for interdiffusion (see discussion in the previous section). The mean concentration of diffusant within the sphere is then a function of the diffusion coefficient and the sphere (grain) diameter. The solutions are available either in table form or as graphs [31]. Reference 31, p.8, provides a graph of mean diffusant concentration versus the permeation distance to half grain size ratio as it applies to diffusion into a sphere. With an experimental determination of mean diffusant concentration the graph then provides a

value for the permeation distance to half grain size ratio. Using the XRD measurements to determine the grain size in turn provides an estimate of the permeation distance.

For this experiment, the mean concentration of diffusant is the difference between the concentration measurements of grain boundary only diffusion and grain boundary plus lattice diffusion. Therefore, they apply only to the kinetic regime where grain boundary filling is complete and lattice diffusion into the grains is taking place. Using the graph for diffusion in a sphere from Reference 31 provides a measure of the ratio between the permeation distance and the half grain diameter. Knowing the grain size then allows a determination of the permeation distance. Comparison of this value with the value predicted by results of previous workers [19, 23] will help to analyze the lattice diffusion process.

5.3 QUANTITATIVE DISCUSSION

5.3.1 Grain Boundary Diffusion

The grain boundary diffusion at the lowest heat treatment temperatures is very rapid particularly for the underlayer element diffusing to the surface. The results of other workers [23] predict a permeation distance of less than 200 Å from grain boundary diffusion (225 °C for 8 hours). This experiment employs films that are over 750 Å thick. Taking the film thickness as a permeation distance the calculation for the 8 hour and 225 °C heat treatment produces a diffusivity of approximately 2×10^{-15} cm^2/sec. The true characteristic length is obviously larger than the film thickness since the layer is completely full before the end of the shortest time lowest temperature heat treatment. This applies to copper and nickel; both elements reach the surface before the 8 hours. The diffusivity from the literature results [23] is 4×10^{-18} cm^2/sec for copper in nickel and 7×10^{-17} cm^2/sec for nickel in copper.

This confirms that grain boundary diffusion for the film structures in this work is extremely fast. Among the possible explanations for the different results are the deposition technique and/or film properties. A faster deposition rate, with less time for atomic arrangement, might facilitate larger grain boundary widths. This factor increases the grain boundary capacity and lowers the resistance of the short circuit path. Other workers have found large variations in activation energy with the orientation of tilt boundaries [32]. It is also possible that the films in this experiment are porous. Diffusion along internal surfaces

of a macroscopic pore is faster than along grain boundaries. Without further investigation, it is not possible to ascertain the actual reason for the difference in diffusivity.

To resolve the discrepancy between the AES and RBS results, for grain boundary diffusion of nickel into copper (Tables 10 and 12), it is simple enough to apply the grain boundary volume fraction model from Section 5.2.1. The following applies to diffusant concentrations in the copper on nickel structure (Tables 10 and 12). The grain size for copper is 260 Å (from the XRD results of heat treatment samples, Table 15). Taking the grain boundary width as 5 Å, the calculated grain boundary volume is approximately 6 %. Thus the 5-6 % RBS result (≤250 °C heat treatments, Table 10) is in better agreement with the model than the AES results (Table 12). For copper diffusing along the boundaries of nickel grains (Tables 10 and 12), where the nickel grain size is 240 Å (Table 16), the volume ratio is also 6 %. AES and RBS agree (5-7 %) with this calculation for the copper on nickel structure (Tables 10 and 12).

For the nickel on copper structure at low temperatures, the grain sizes are 230 Å for nickel and 330 Å for copper (Tables 19 and 20). The volume ratio calculations in turn produce 7 % for copper in nickel and 5 % for nickel in copper. The RBS simulations of the measurements at the same low temperatures produce similar results (5-7 %, Table 11) for both copper in nickel and nickel in copper.

The evidence plainly supports grain boundary diffusion taking place at the 225 °C and 250 °C heat treatment temperatures. The extent of grain boundary filling is in good agreement with what one expects from the grain boundary volume ratio. It is possible to

suggest reasons for the rapid diffusion seen in this work and that published by other workers. However, a conclusive reason will require quantitative measures of the diffusivity and activation energy. As the diffusing elements were able to permeate throughout the thickness of a layer in the thin film structure, such data could not be extracted from the experimental results.

5.3.2 Diffusion in the Lattice

The Auger and RBS results suggest that, after heat treatment for 8 hours at 400 °C, the thin film structure has almost a 50 % average composition. The prediction for permeation distance of nickel in single crystal copper, from lattice diffusion at this heat treatment condition, is less than 10 % of the grain diameter (Table 3). As seen in the x-ray diffraction patterns (Figures 36 and 37), there are still copper and nickel regions within the thin film structure. Therefore, mass transport has not produced a homogeneous alloy film. Instead, lattice diffusion is creating an outer "crust" in the grains where an inhomogeneous concentration can approach the high concentrations that may exist at the grain boundaries.

For the model of diffusion into a sphere (Section 5.2.2), the initial conditions in this experiment are a diffusant concentration of zero in the grain. The assumption is the surface concentration of diffusant is 100 % at the boundary. After the 400 °C for 8 hours heat treatment, the AES results put the average concentration of nickel in copper at 49 %. This is the average concentration of diffusant in the grains and grain boundaries. The concentration due to grain boundary diffusion is 12 % (Table 12) giving a mean diffusant

concentration inside the grain of 37 %. The result is similar (40 %) when using the RBS simulation estimates. The ratio of permeation distance to (half) grain size is 0.12 (from graph, Reference 31, p.8) and this produces a permeation distance of 16 Å for a 260 Å grain diameter. This indicates a slightly slower diffusion than the 19 Å calculation using the results for diffusivity in single crystals (Table 3). If the concentration at the grain surface is less than 100 %, a larger permeation distance of nickel into copper must necessarily provide the same matrix concentration. This occurs when both copper and nickel are present in the grain boundaries. The experimental results do not determine the proportion of copper and nickel in the grains. However, it is possible that their concentrations are in proportion to their relative diffusivities. That is, if nickel is diffusing faster in the grain boundaries, as indicated by other workers [24, 25], then it will be the dominant element in the boundary regions.

There is no expectation of copper significantly diffusing into the nickel grains for any of the heat treatment conditions in this experiment. The diffusion coefficient [21] gives a permeation distance of less than 2 Å (after 8 hours at 400 °C). It is possible to estimate the concentration of diffusant in a (spherical) grain by using the volume of a sphere. First, assume that the entire permeation distance is at 100 % of the diffusant. This is an extreme limiting case and the actual diffusant concentration is obviously less than 100 %. For comparison, however, a grain size of 240 Å (Table 16) will put the concentration of diffusant in the grain at 5 %. This is the concentration above the grain boundary concentration. However, the AES measurement results for copper on nickel at 350 °C and

400 °C (Figure 32) clearly show nickel diluted to >30% copper close to the copper nickel boundary. Even deeper into the nickel layer, lattice diffusion is certainly taking place as the concentration increases more than 5 % above the grain boundary volume. The RBS measurement of the copper on nickel structure also supports lattice diffusion of copper into nickel; there is a decrease in counts at the high energy side of the nickel peak (Figure 18). The models for diffusion in polycrystalline films are not able to account for this behavior.

To complete the discussion of lattice diffusion it is important to mention the Kirkendall effect [33]. Interdiffusion in a binary couple will produce interface movement when one element has a higher diffusivity than the other. Diffusion by the vacancy mechanism will compensate the mass flow as vacancies move in the opposite direction. The outcome is the formation of voids or a concentration of vacancies that varies with the immediate concentration. This experiment and other workers [19, 23] clearly conclude that nickel diffuses faster than copper. Neither RBS nor AES are able to detect voids; there is no energy loss by the helium beam through a vacancy or void and the sputter erosion will simply jump across a void without indication. Therefore, continued work is necessary to determine if there is void formation, since it may relate to the enhanced copper diffusion.

5.3.3 Activation Energies

It is difficult to determine the activation energies of the grain boundary diffusion seen in this experiment. The first problem is the limited data. Compounding the issue is the rapid grain boundary diffusion. The grain boundary diffusion was complete before the end of the shortest time, lowest temperature heat treatment. This prevented measuring differences in diffusion with either time or temperature.

Figure 44 is a plot of the mean diffusant concentration squared, of nickel in copper, versus inverse temperature from the AES and RBS data for copper on nickel. Again, the mean diffusant concentration is the difference in concentration measurements between lattice plus grain boundary diffusion and grain boundary only diffusion. It applies to the regime where lattice diffusion and grain boundary diffusion occur simultaneously. The data is specifically for the 8 hour heat treatments. The activation energy for lattice diffusion from the AES data is approximately 1.60 eV and the correlation factor (R^2), from linear regression, is 0.91.

This activation energy is lower than the results published by other workers (>2 eV, Table 1) for nickel lattice diffusion in copper. It suggests that diffusion will occur readily at lower temperatures. However, the comparison of permeation distances for diffusion in a sphere (Section 5.3.2) indicates that, if anything, the nickel lattice diffusion in this experiment is slower than expected from results of other workers [17].

The curves from both the AES and RBS results possibly flatten out at the higher temperatures in the graphs of Figure 44. This may explain the lower activation energy. If

indeed the curves do flatten out it is equivalent to decreasing activation energies with increasing temperature. Therefore, the curve of the square of concentration versus (inverse) heat treatment temperature does not necessarily have an Arrhenius relationship and suggests a "saturation" due to either concentration dependent diffusivity or multiple mechanisms. The results in this experiment do not provide an adequate explanation for this behavior of nickel lattice diffusion in copper. It is not obvious if the AES data reduction is the cause since the RBS data shows the same trend.

5.4 APPLICATION TO HEAD STRUCTURES

For applications of copper and nickel thin film structures, the results in this experiment prove that diffusion will take place at temperatures as low as 225 °C. The lower limit for permeation distance in this experiment is 775 Å from grain boundary diffusion. In practice, the copper and permalloy (NiFe) layers have a total thickness of 40 - 80 Å for magnetoresistive read heads.

It is possible to use the results of this experiment and the grain boundary model of volume ratio to predict mass transport in thinner films. This is an estimate of the extent of grain boundary filling for a film in an actual structure. The ratio of grain size to film thickness is a way to estimate the grain size of the thinner films. If the permeation distance is only the film thickness of this experiment it provides an estimate of the diffusivity. (This value is low because the permeation distance is larger than the film thickness, even after the 8 hour at 225 °C heat treatment.)

Using results from the copper on nickel structure, the 8 hour at 225 °C permeation distance is 775 Å and produces a minimum diffusivity of 2×10^{-15} cm^2/sec. The copper grain size to film thickness ratio is 0.34. If the application structure uses a copper thickness of 50 Å then its grain size is 17 Å, approximately. Heat treatment of this film at 225 °C will fill the 30 % volume fraction of grain boundaries within 120 seconds! This is a first order calculation with a large uncertainty but clearly represents a large amount of mass transport at temperatures the film will experience during processing and operation.

It is more likely that the grain size at this level is approximately the film thickness. Therefore, it is necessary to extend the grain structure model to account for this by using, for example, columnar grains with a spherical cross-section. Such a structure produces a volume ratio of 14 % which will also fill in less than 2 minutes.

5.5 SOURCES OF ERROR

There are two important sources of uncertainty that influence the quantification of results. First there is the algorithm to deduct the copper Auger transition from the nickel signal. Although the algorithm does not change the qualitative interpretation of the outcome, there are significant discrepancies in diffusion concentrations between the AES and RBS techniques. The second concern is the difficulty in obtaining unique simulations from the RBS measurements. In this case, the variation in concentration makes the film structure more complicated with a number of possible RUMP solutions.

5.5.1 Removal of AES Copper Overlap

The algorithm to remove the copper overlap from the AES nickel signal involves several steps. To begin with, there is a subtraction of a background signal from the Auger intensity (versus energy) measurements. Following is a determination of the integral signal peak heights and the ratio of copper signals in the two element windows. From there, the ratio provides a measure of the copper contribution to the nickel signal. If there are any errors in the background subtraction, its effect will pass through all the calculations.

The background subtraction that results in a smaller reduction of the copper overlap is the one that decreases the ratio of the two copper signals. The two error conditions, to produce this situation, are too much background subtraction from copper in the nickel window and not enough reduction of copper in copper window. It is better to determine the background signal in a region where there are no measurements of Auger

transitions within the energy range of interest. That is, when all the electron emissions in the energy spectra originate from scattering events. However, there are always Auger transitions in the nickel window; they originate from either nickel itself or the lower energy copper transitions. Therefore, it is difficult to determine the correct background signal in the nickel energy window. If the estimate is too small, the result is not enough subtraction of the copper overlap in the nickel signal and will produce excessive grain boundary concentrations.

There was a compromise to the background subtraction in the nickel energy window as all measurements did include Auger transitions. If the depth profiling continues into the substrate, where presumably no copper or nickel is present, then it is possible to determine the background signal for the nickel window under the similar measurement conditions.

5.5.2 RBS Simulations

RUMP solutions are often not unique and many times require additional RBS measurements to reinforce the result. The problem is difficult with complicated structures as happens with inhomogeneous diffusion profiles. It is better practice to use the results from multiple techniques to determine a more exact solution.

In this experiment, the RUMP simulations did provide some valuable quantitative information when the heat treatment temperature was below 300 °C. The qualitative interpretations also agree with the AES and XRD measurements. However, the

inhomogeneous distribution of copper in nickel above 250 °C produced quantitative results from simulations that are possibly off by up to 50 %.

5.6 FIGURES

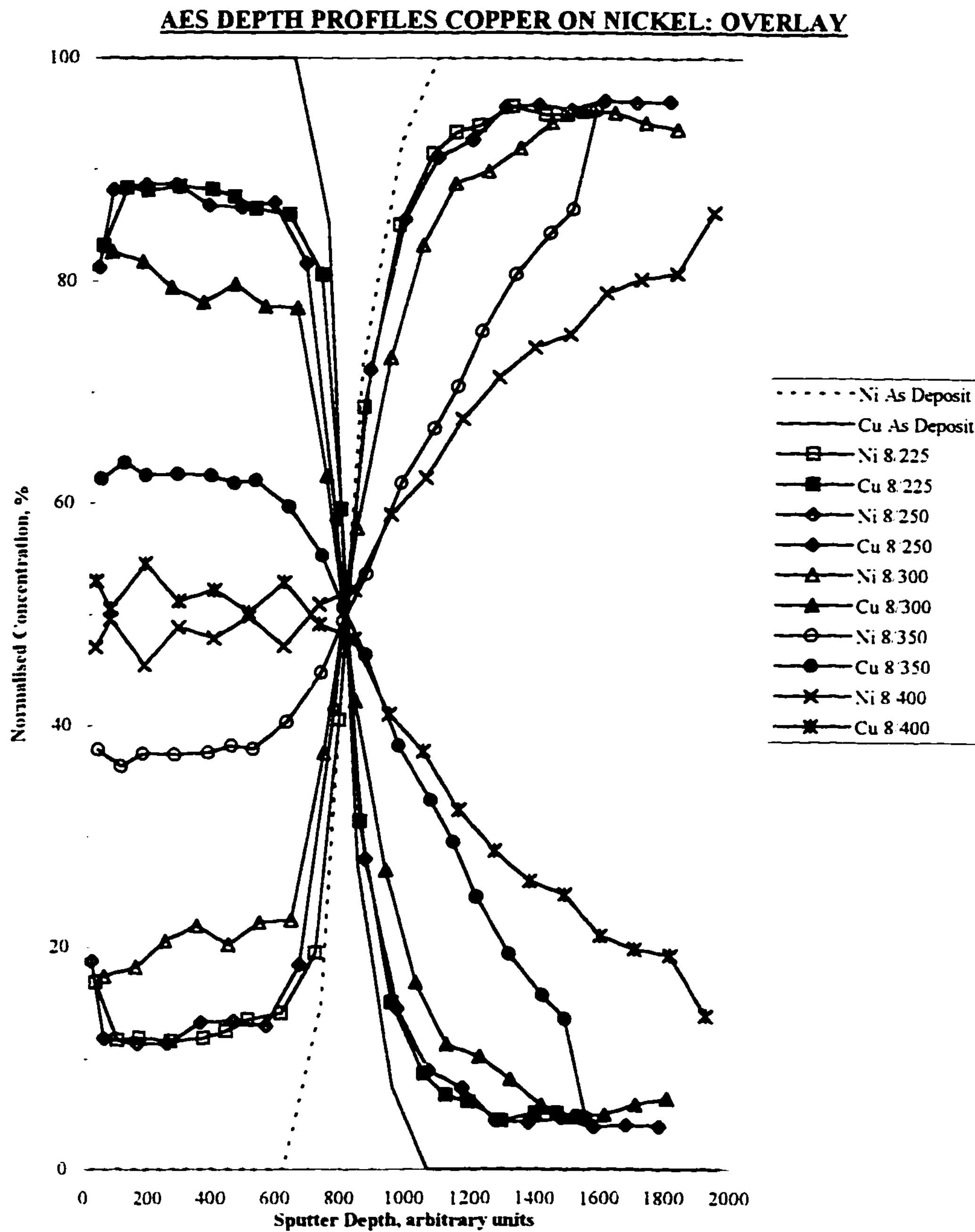

Figure 38 AES Concentration Profiles for 8 Hour Heat Treatments

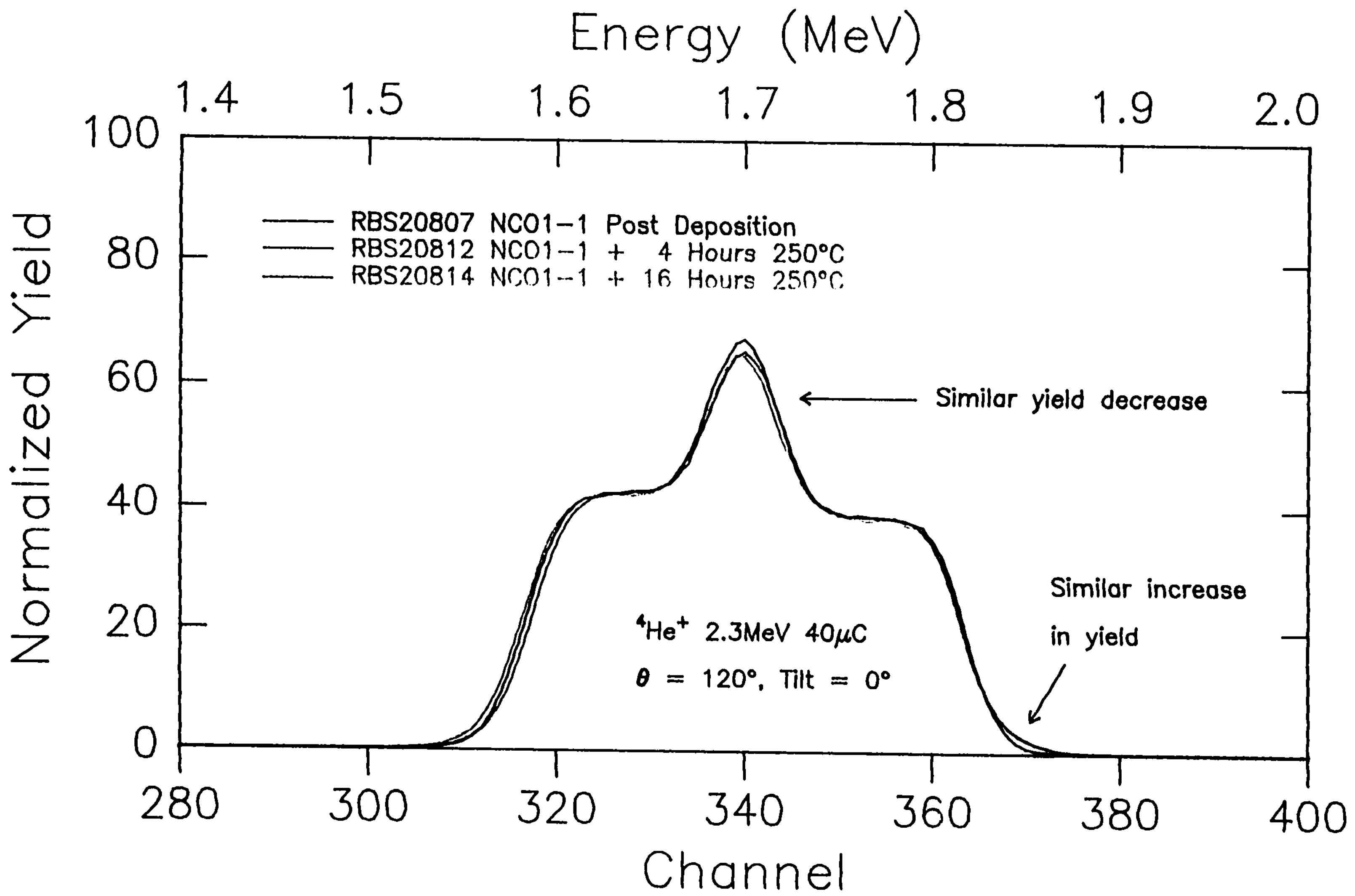

Figure 39: RBS Overlay Measurement Spectra for 250 °C Heat Treatments

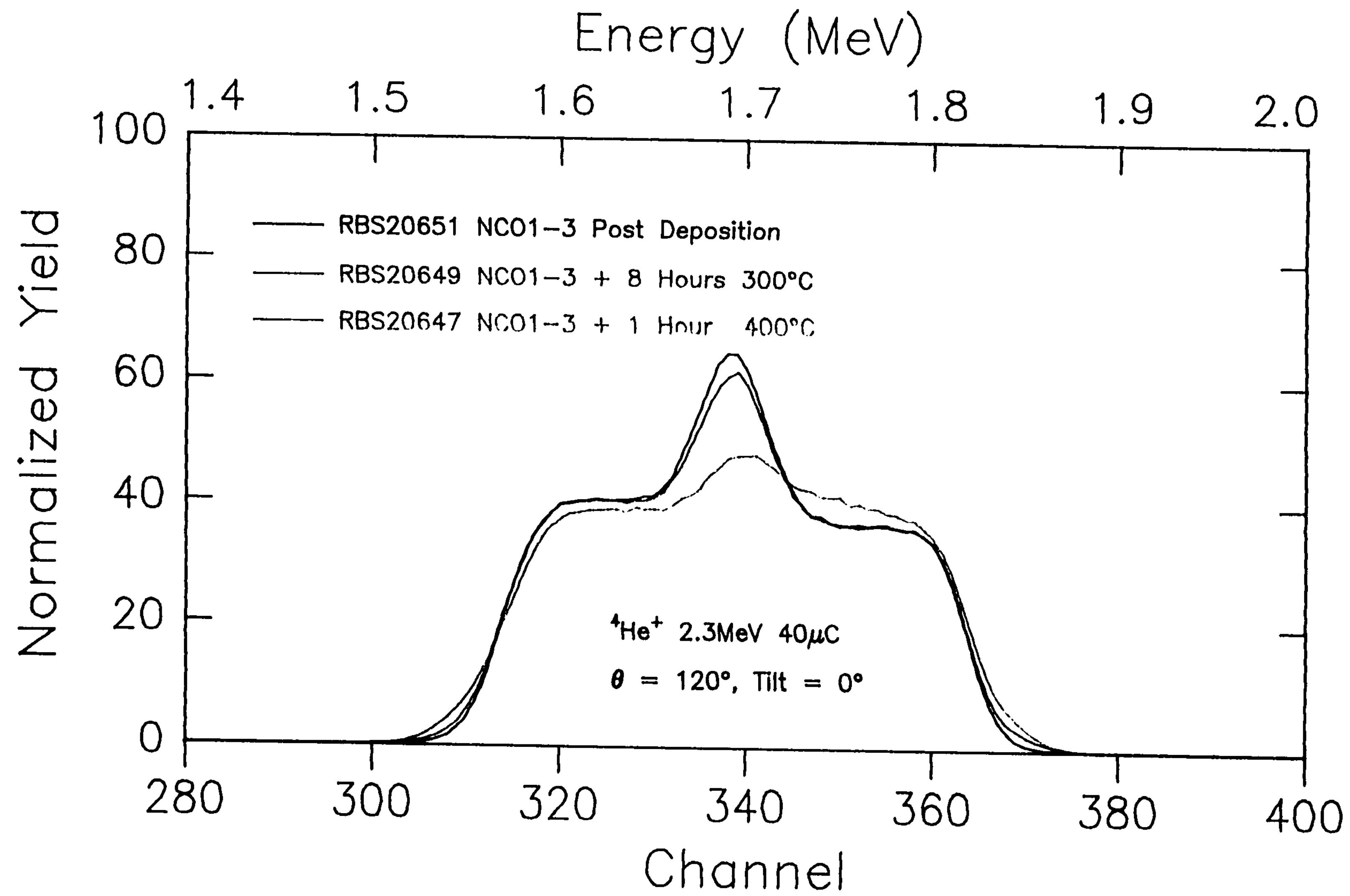

Figure 40: RBS Overlay Measurement Spectra for Different Times and Temperatures

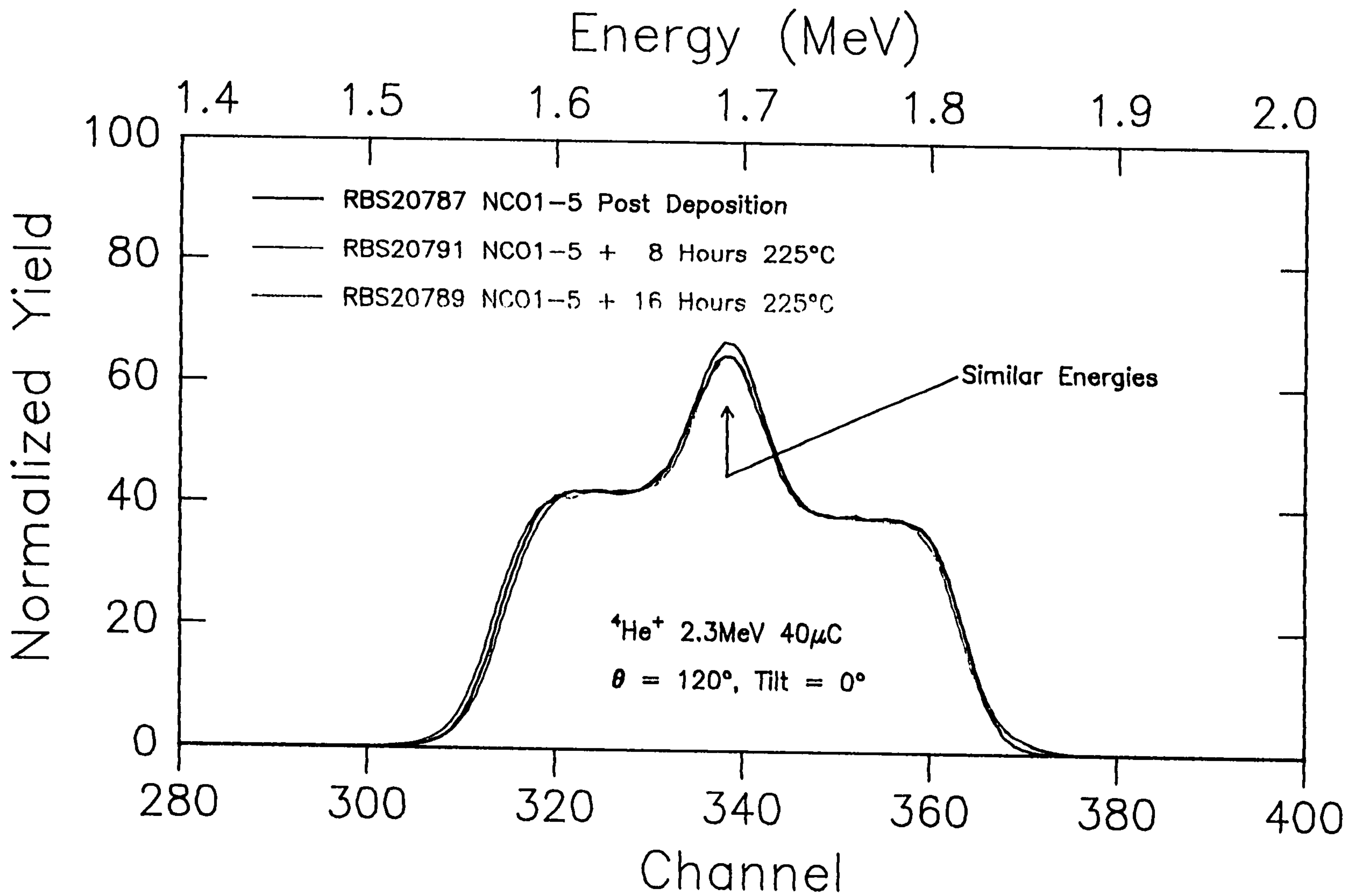

Figure 41: RBS Overlay Measurement Spectra for 225 °C Heat Treatments

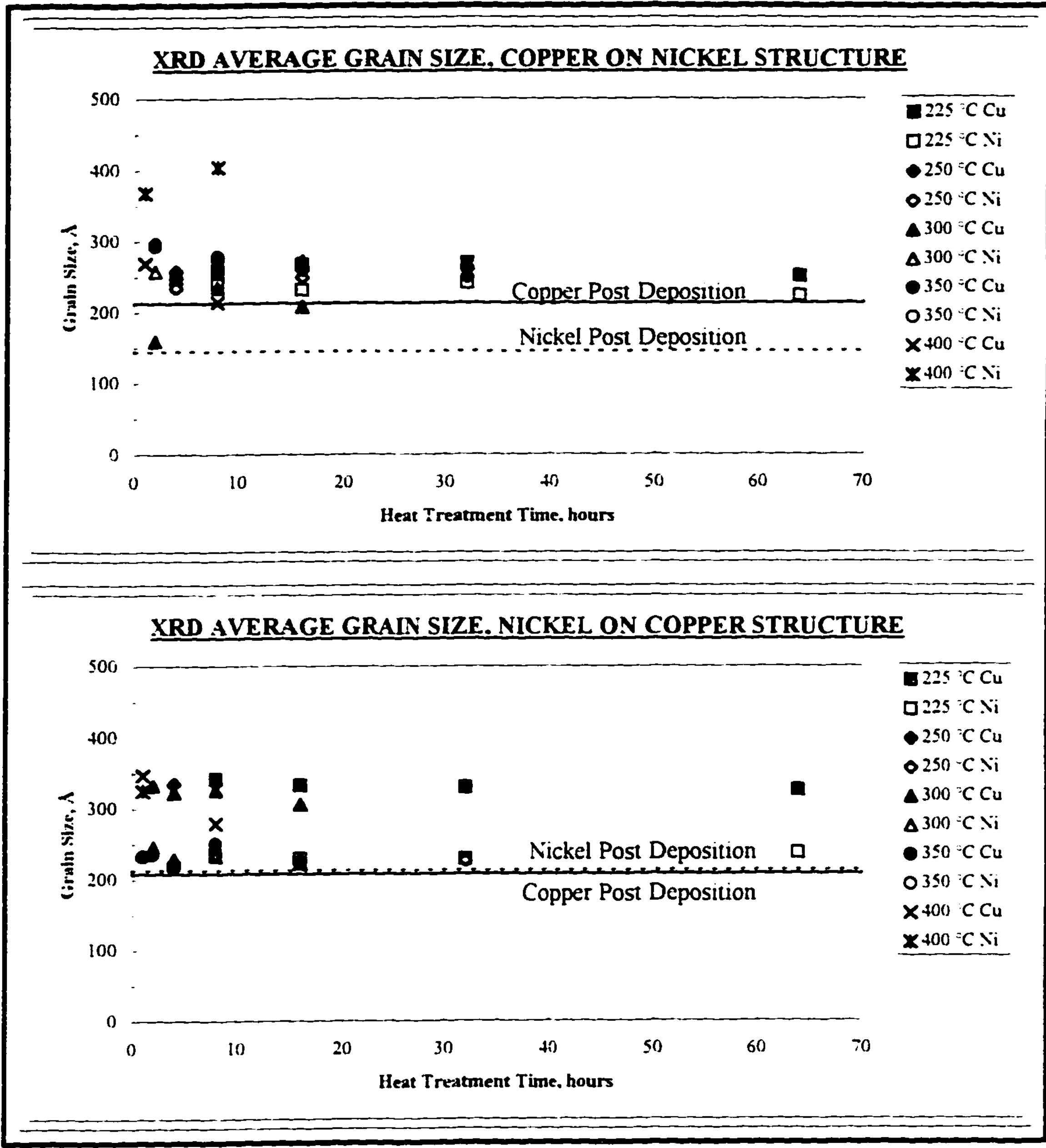

Figure 42: XRD Grain Size Changes with Temperature

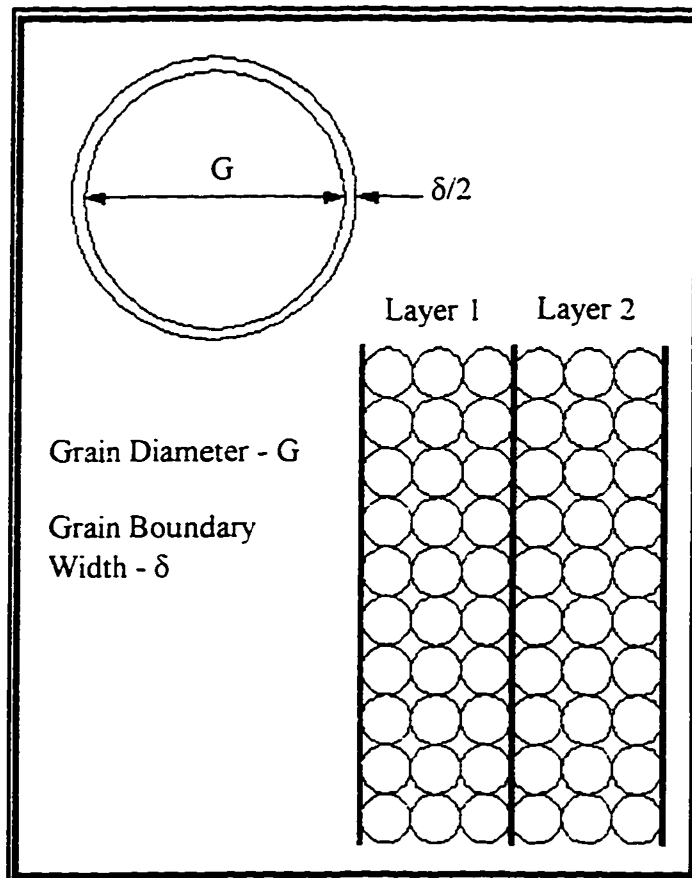

Figure 43: Schematic of Grain Structure

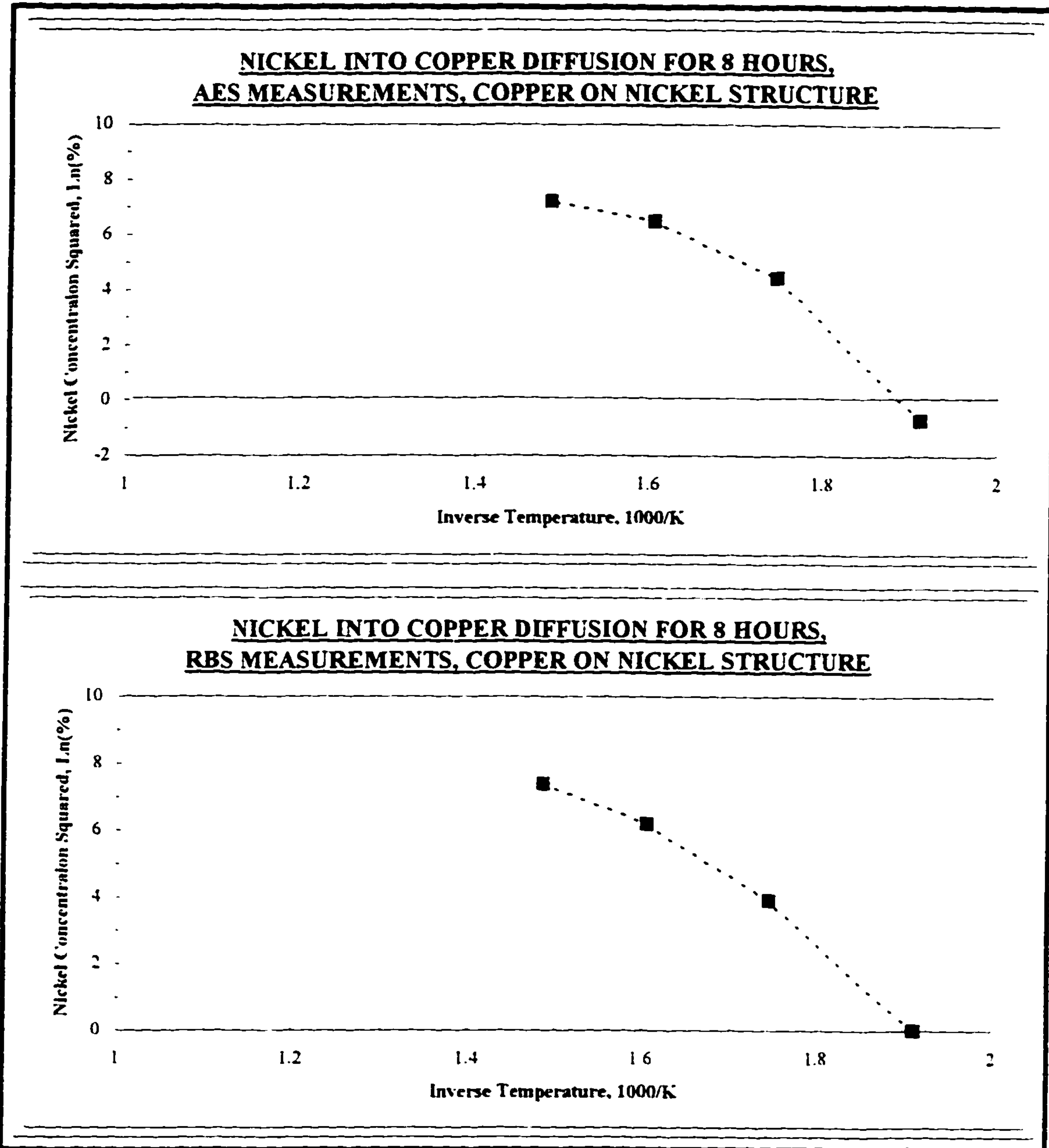

Figure 44: Lattice Diffusion Saturation

6.0 CONCLUSIONS

There are two regimes of diffusion kinetics for the copper nickel bilayers of this experiment. At temperatures of 225 °C and 250 °C the kinetics is Type C. The transformation to Type B kinetics takes place between 250 °C and 300 °C. Diffusion in the Type C regime is from short circuit paths; this includes grain boundaries, dislocations, and probably internal surfaces (pores). Lattice diffusion kinetics of nickel into copper grains is similar to diffusion of nickel in single crystal copper reported by other workers [17]. However, there is an enhanced lattice diffusion of copper in nickel grains. The results in this experiment do not readily explain the variation in concentration of copper in the nickel film.

The third x-ray diffraction peak is due to diffusion into copper and nickel grains where core regions of the grains remain undiluted. The continued appearance of three diffraction peaks (copper, nickel, copper-nickel alloy) supports an inhomogeneous distribution of copper nickel alloy throughout the thin film structure.

An improvement in the AES measurement technique will refine the experimental results. This includes better reduction of the data and taking measurements in the substrate. This will help to refine this untested algorithm of removing the overlap in signals from two elements.

The rapid diffusion along short circuit paths prevented a precise determination of activation energy and/or diffusivity. To make such measurements it is necessary to repeat the experiment for the low temperature heat treatments (250 °C and below) using either

shorter and more annealing times or thicker films. This can help to establish a clear time to arrival of the underlayer element at the surface.

In addition, the apparent saturation of lattice diffusion at the higher temperatures made it difficult to accurately determine any time dependence or activation energy. Again, more heat treatment times, specifically between 250 °C and 325 °C, can help in the quantification of lattice diffusion. Such a refinement in the experiment may also provide some insight into the inhomogeneous copper diffusion.

It is obvious that the deposition technique will influence the behavior of diffusion in thin films. The next step is to examine the remaining two binary structures (iron nickel and iron copper) in this sequence and establish baseline models. It is then important to use similar or exact deposition conditions as for the application when investigating the copper-permalloy ternary structure.

7.0 REFERENCES

1 C. Mény, *et al.*, J. Magnetism and Magnetic Materials **121** (1993) 406.

2 V.S. Speriosu, *et al.*. Phys. Rev. B **47**, 17 (1993) 579.

3 M.H. Tabacniks, *et al.*, Mat. Res. Soc. Symp. **382** (1995) 389.

4 D. Gupta, "Some Formal Aspects of Diffusion," in Diffusion Phenomena in Thin Films and Microelectronic Materials, Eds. D. Gupta and P.S. Ho, © 1988 Noyes Publications.

5 T.C. Huang, *et al.*. Appl. Phys. Lett. **62**, 13 (1993) 1478.

6 D.Y. Shih, *et al.*, J. Appl. Phys. **70**, 6 (1991) 3052.

7 B.D. Cullity, Introduction to Magnetic Materials, © 1972 Addison-Wesley, p. 113.

8 J.E.E. Baglin, Private Communication, 1996.

9 J.P. Noziéres, *et al.*, J. Magnetism and Magnetic Materials **121** (1993) 386.

10 D. Gupta, "Diffusion in Metallic Thin Films" in Diffusion Processes in High Technology Materials, © 1988 Trans Tech Publications, Switzerland.

11 L.I. Maissel and R. Glang, Handbook of Thin Film Technology, McGraw-Hill Publishing Company, © 1970, p.23-16.

12 J. Crank, The Mathematics of Diffusion, Oxford University Press (1956).

13 J.E.E. Baglin and J.M. Poate, "Metal-Metal Interdiffusion" in Thin Films -- Interdiffusion and Reactions, J.M. Poate, et al., Eds. John Wiley and Sons (1978).

14 L.G. Harrison, Trans. Faraday Soc. **57** (1961) 1191.

15 R.W. Balluffi and J.M. Blakely, Thin Solid Films **25** (1975) 363

16 I. Suni, *et al.*, Thin Solid Films **79** (1981) 69.

17 C.A. MacKliet, Phys. Rev. **109**, 6 (1958) 1964.

18 A. Ikushima, J. Phys. Soc. Japan **14** (1959) 1636.

19 M.B. Dutt, *et al.*, Phys. Stat. Sol. **56** (1979) 149.

20 S. Ceresara, *et al.*, Phys. Stat. Sol. **16** (1966) 439.

21 H. Helfmeier and M. Feller-Kniepmeier, J. Appl. Phys. **41**, 8 (1970) 3202.

22 J.E. Lewis and P.S. Ho, J. Vac. Sci. Technol. **20**, 3 (1982) 466.

23 H. Lefakis, *et al.*, Thin Solid Films **101** (1983) 207.

24 D. Gupta and P.S. Ho, Thin Solid Films **72** (1980) 399.

25 M.L. Tarng and G.K. Wehner, J. Appl. Phys. **42**, 6 (1971) 2449.

26 T. Tsakalakos and J.E. Hilliard, J. Appl. Phys. **55**, 8 (1984) 2885.

27 J. Klöber, *et al.*, Phys. Stat. Sol. A **94** (1986) K25.

28 Handbook of Auger Electron Spectroscopy, 2nd. Ed., L.E. Lewis, *et al.* Eds., Physical Electronics Division, Perkin-Elmer Corporation, © 1976.

29 L.R. Doolittle, NIM **B15** (1986) 227.

30 JCPDS-ICDD PDF Database, 1996.

31 L.S. Darken, "Formal Basis of Diffusion Theory" in Atom Movements, © 1951 American Society for Metals.

32 L.E. Murr, Interfacial Phenomena in Metals and Alloys, Addison-Wesley Publishing © 1975, p.295

33 A.D. Smigelskas and E.O. Kirkendall, AIME **171** (1947) 130.

APPENDIX I: RUTHERFORD BACKSCATTERING SPECTROMETRY

INTRODUCTION

In Rutherford Backscattering Spectrometry (RBS), a mono-energetic ion beam bombards a target material. Most of the ions will undergo changes in both energy and direction. If the target is very thin, some ions may traverse through and lose energy in the process. A few ions will scatter backwards from the target and strike a charged particle detector. The detector is at a known angle to the ion beam and measures the energy of the scattered ions.

In some respects, RBS is a non-destructive technique although this depends on the target. In certain cases, integrated circuits are sensitive to ion bombardment damage. However, for most samples RBS does not create any significant damage and is a suitable method for measuring the composition of thin films. The technique determines the masses of target atoms and is also capable of resolving the depth of the collision without the need for destructive profiling techniques.

BACK SCATTERING PROCESS

There are four physical concepts in the back scattering process: kinematic factor, scattering cross section, stopping cross section, and energy straggling. The kinematic factor is the discernment of mass from an elastic two-body collision. The scattering cross section is a description of the probability of a detectable collision event. The stopping cross section describes the energy loss of an ion traveling through a target and leads to the

determination of depth of a scattering event. The limitations in mass and depth resolution arise because of the statistical variation in energy losses, known as straggling. This section is a discussion of the first three concepts above. Remarks on straggling appear in the section on limitations of RBS.

The collision between an ion and a target atom is solvable with a hard sphere model. The kinematic factor is the ratio of the energy after a collision to the energy before. Its derivation is from simple elastic collision energy and momentum conservation.

$$\text{Kinematic Factor, } K = \frac{E_{After}}{E_{Before}} \qquad \text{(A1.1)}$$

$$K_{M_2} = \left[\frac{\sqrt{M_2^2 - M_1^2 \cdot \sin(\theta)} + M_1 \cdot \cos(\theta)}{M_1 + M_2} \right]^2 \qquad \text{(A1.2)}$$

Equations A1.1 and A1.2 give the kinematic factor [A1.1] of an unknown target atom; the mass of the bombarding ion and target atom are M_1 and M_2, respectively. The detection angle is θ relative to the incident beam direction. The equations determine the back scatter energy of the ion with a given starting energy. Therefore, the scattering energy identifies the mass of the target atom with the use of Equation A1.2. In practice, RBS measures the energy of a scattered particle at a known scattering angle.

Not all ions that strike the target will scatter backwards. The ratio of the number of ions scattered in any direction to ions hitting the target is approximately one in 10^4. The frequency of such collisions is an empirical function of the number of particles hitting the target (ion counting or charge collection), the target atomic density, and the target

thickness. The number of ions reaching the detector depends on the scattering angle and the solid angle subtended by the detector (Figure A1.1). The scattering cross section is used to describe the probability that an ion will scatter and reach the detector [A1.1].

$$A = \sigma \cdot \Omega \cdot Q \cdot N \cdot t \qquad (A1.3)$$

$$\sigma = \int_{\Omega} \frac{d\sigma}{d\Omega} d\Omega \qquad (A1.4)$$

$$\frac{d\sigma}{d\Omega} = \left[\frac{Z_1 Z_2 e^2}{4 \cdot E \cdot \sin^2\left(\frac{\theta}{2}\right)} \right]^2 \qquad (A1.5)$$

In Equation A1.3, A is the number of particles that reach the detector, Q is the total dose of ions, N is the atomic density of the target atoms, and t is the target thickness. The parameter Ω is the solid angle subtended by the detector and the scattering cross section is represented by σ.

Equation A1.4 is the average scattering cross section. Equation A1.5 is a model for the average differential cross section [A1.1]. In summary, the cross section depends on certain physical quantities. Obviously the atomic species, as Z_1^2 and Z_2^2, are important; they are the bombarding ion and target atom. The probability of scattering will increase with the size of either the ion or target atom. However, back scattering will only take place when a lighter ion collides with a heavier (stationary) atom. As such, it is not possible for RBS to detect atoms of the same or lighter mass than the primary ion.

The chance of a collision is inversely proportional to the square of the ion energy. Thus, with lower energies, or as the ion loses energy traversing through the target, the scattering efficiency will increase. Since the scattering cross section is inversely proportional to the detection angle, the scatter yield increases as θ decreases.

As the energetic ion penetrates the target material it loses energy and thus velocity. The energy loss is a result of small angle collisions (nuclear stopping) and ionization interactions with the electron clouds of target atoms (electronic stopping). The extent of the loss depends on the mass and composition of the target material as well as the ion and its energy. Since it is time consuming to make theoretical calculations there are tables of the stopping cross sections made from measurements. The stopping cross section of alloys and compounds is weighted according to the relative atomic abundance of elements.

The outcome of stopping cross sections is a range in back scatter energies for an element that is greater than a monolayer in thickness. This represents the areal density of the film as ions lose energy traveling in the forward and backward directions. With precise knowledge of film density and charge collection it is simple to convert this result into the thickness of the film. True film density is often not known exactly and the uncertainty in the charge collection depends on the precision of the electronics.

APPLICATIONS OF RBS

RBS uses a high energy beam of ions typically $^{4}He^{+}$ at around 2 MeV. An ion source generates charged particles that a high voltage will then accelerate towards a

target. Focusing, collimating, and filtering to a particular mass and energy take place along the beam line. To reduce unwanted collisions with gas phase molecules, measurements take place in a vacuum, typically at the 10^{-6} Torr level.

RBS is a technique for measuring the composition of thin films that are up to a few microns thick. As it is able to resolve the depth of scattering events, it is possible to determine thickness with certain limitations. The uncertainty in thickness arises from the accuracy in ion counting, stopping cross section, and film density. However, it is reasonable to compare the relative thickness, of similar films or structures, with some accuracy. More appropriately, though, RBS determines the areal density of thin films. The method does not require the use of reference samples or standards.

RBS is both a qualitative and quantitative technique. Figure A1.2 is an example of an RBS measurement. The energy scale identifies the elements present in a thin film structure, as the figure demonstrates with the vertical arrows. If the element is not present at the surface then energy losses displace its high energy position. The signal from under lying films will appear at lower energies depending on the density of materials that are above. The relative peak areas are proportional to the composition in the thin films providing results with low uncertainties (± 3 %).

RBS does have a detection limit of less than 10^{14} atoms/cm^2 [A1.2] making the technique useful for studying diffusion. This applies to spectra where there is good energy separation between the constituent elements. (If this is not the case, the detection limit may increase one or two orders of magnitude.) The back scatter spectrum simulation in

Figure A1.3 is for two films, one on top of the other. The solid lines show two peaks, one for each film or element in their as deposit condition. The region between the peaks is the back scattering energy of an element from one film in the matrix of the other film. The broken lines represent back scattering of atoms from the overlayer after their mass transport into the underlayer. Measurements of these kinds of changes in the back scatter spectrum can provide valuable information about the diffusion process.

LIMITATIONS OF RBS

In the back scattering process there are a number of limitations due to statistical variations in energy losses. This is energy straggling and it limits both the depth and mass resolution of RBS. The two causes are the different energy loss mechanisms and the variation in energy losses throughout the target material. Therefore, ions that start with the same energy will end with different energies after traveling into and out of the target material. This limits the determination of the collision depth and the film thickness. Since the ion beam is no longer mono-energetic after it passes below the surface, the uncertainty in mass resolution is higher for all atoms below the top monolayer.

Thickness determination is a function of charge collection, film density, and stopping cross section. The latter variable has the most uncertainty because their determinations are from measurements with poor precision [A1 1]. With appropriate charge collection electronics the counting of ions should have the smallest uncertainty. The density for single element metal films should be close to their bulk values but this is

dependent on the deposition method, among other factors. Experimental values of density for films are more reliable than computations from bulk density and relative abundance. Even so, it is normal practice in RBS to work with the number of atoms per unit area (atoms/cm^2). The need to know the film density is only important when making comparisons of thickness with other measurement techniques such as profilometry.

The difference in scattering energies is small for elements close to each other in the periodic table because their masses are similar. It is difficult to resolve the spectrum of a film with two or more such elements. In many situations, the back scatter energies will overlap. Structures with elements similar in mass, or where the back scatter energies overlap, will constrain the capability of RBS.

Other limitations in RBS are variation in electronic stopping within the target material as well as variation in film density. Channeling may take place if ions travel between the crystalline lattice positions or planes. As collisions and interactions for channeled ions take place deeper into the target, the loss of energy is different. It is possible to overcome most of the limitations above but effective analysis of thin films and diffusion will generally involve measurements with multiple techniques.

REFERENCES

A1.1 W-K. Chu, *et al.*, Backscattering Spectrometry, Academic Press, 1978.

A1.2 M.H. Tabacniks, *et al.*, Mat. Res. Soc. Symp. **382** (1995) 389

FIGURES

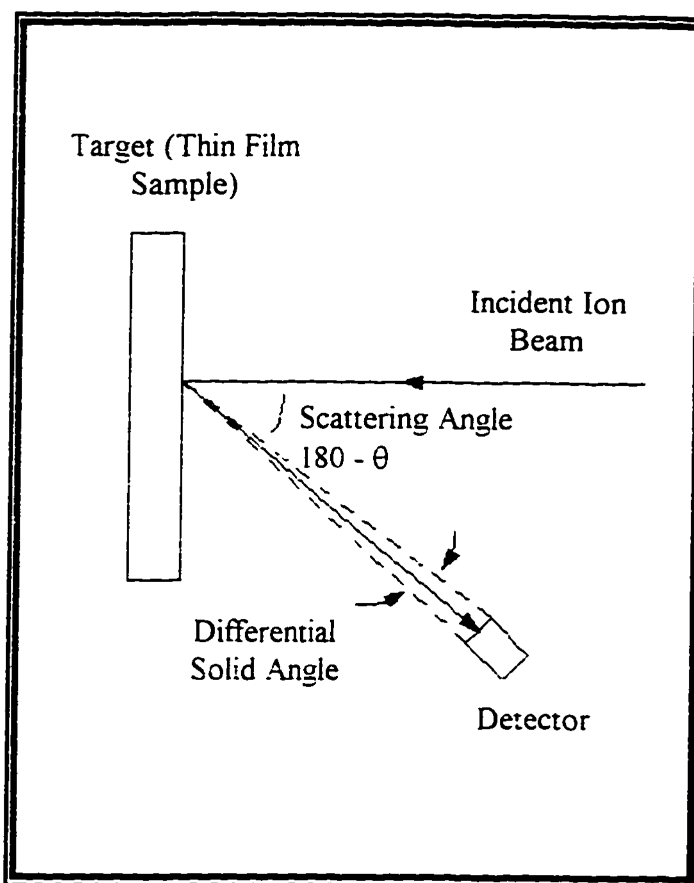

Figure A1.1 Schematic of a Back Scatter Experiment.

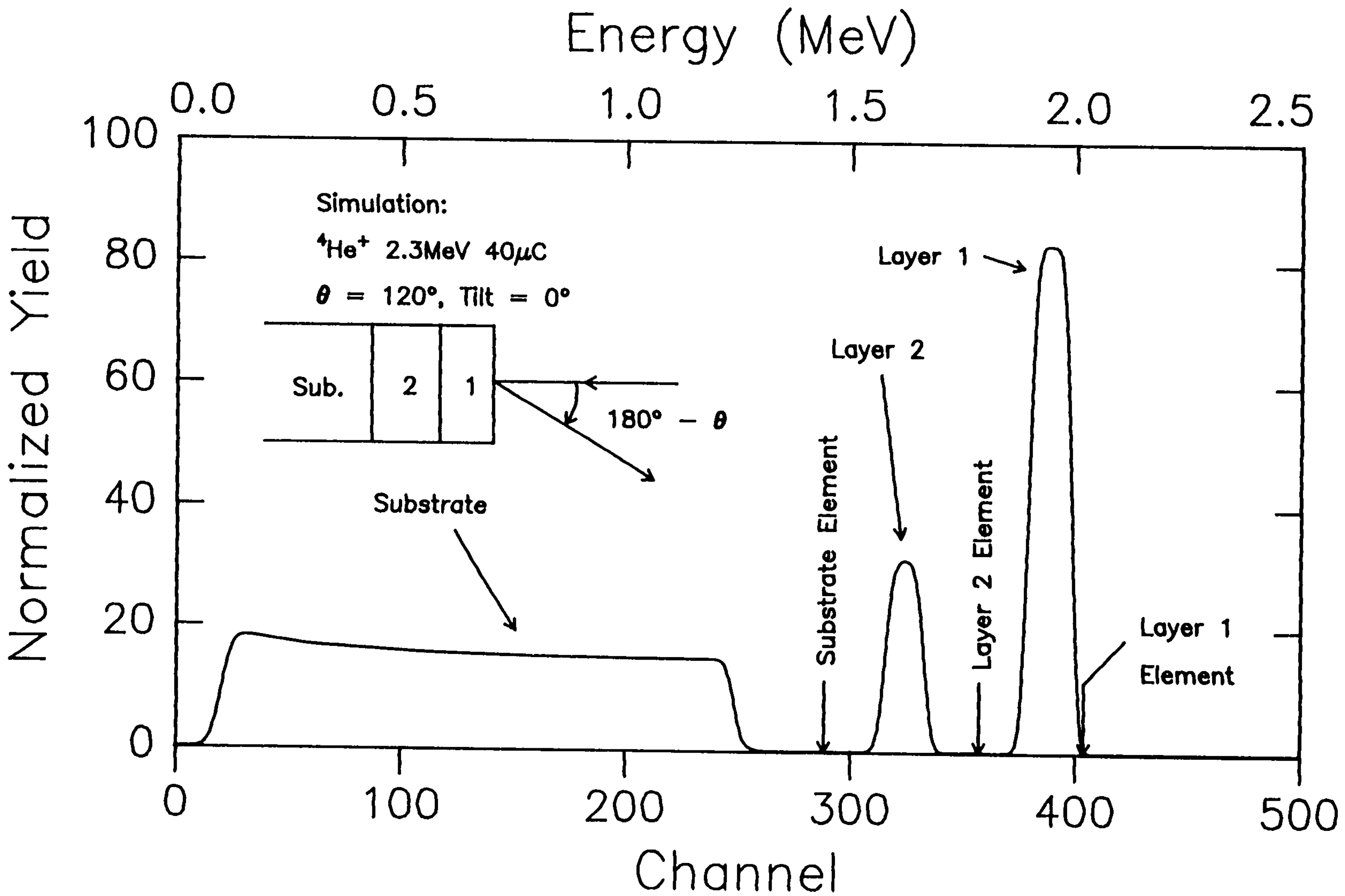

Figure A1.2: Example RBS Spectrum

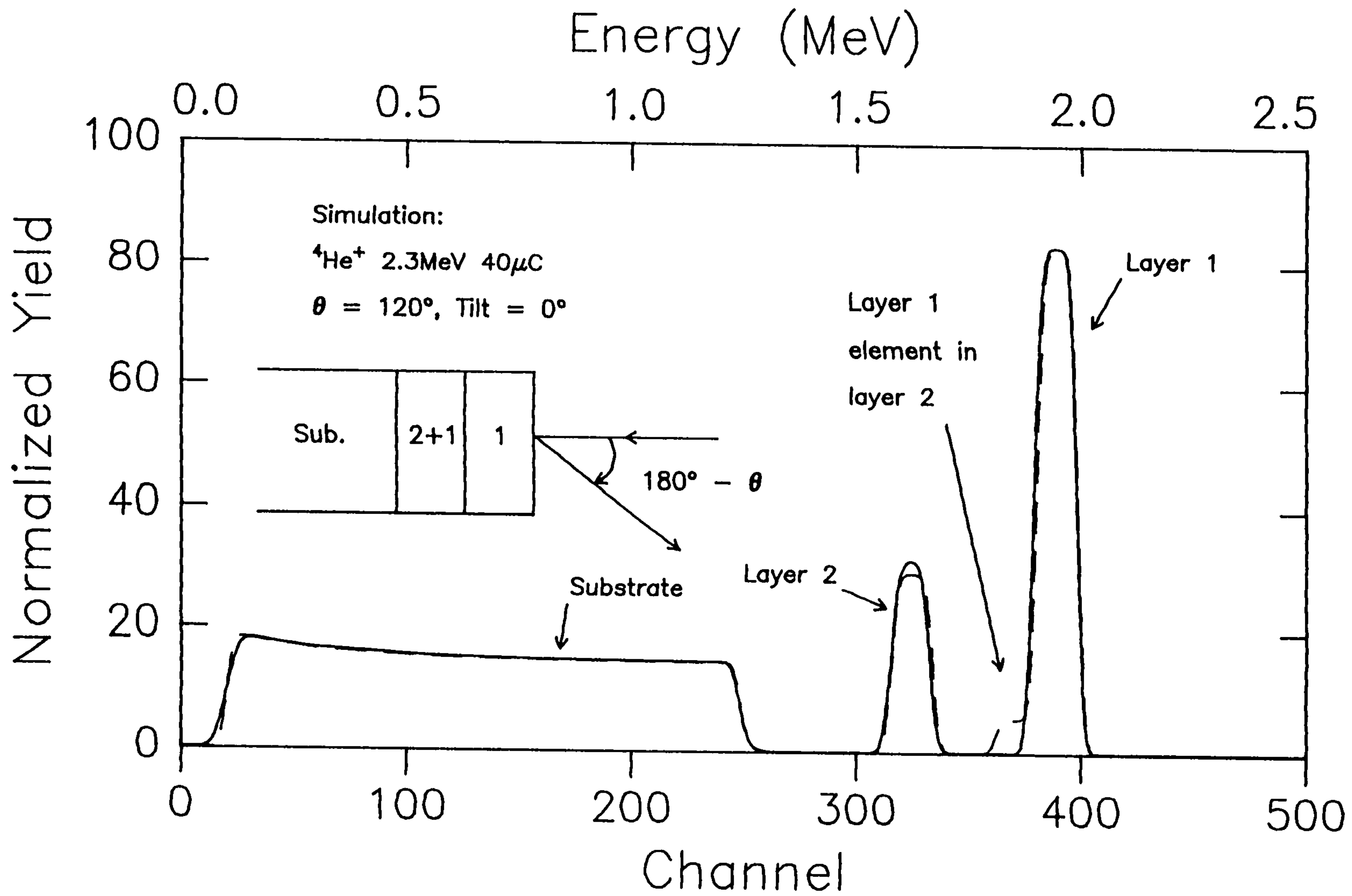

Figure A1.3. Measuring Diffusion with RBS

APPENDIX II: AUGER ELECTRON SPECTROSCOPY

INTRODUCTION

Auger Electron Spectroscopy (AES) is a sensitive surface analysis technique. The measurement relies on Auger emissions that result from bombardment of a sample by electrons or x-rays. The energy of an Auger electron is characteristic of the original atom since the process involves more than one core level. AES can evaluate variations in composition, either across a surface or in a perpendicular direction, and it is suitable for thin film analysis and appropriate for diffusion studies. Rapid data acquisition is possible with suitable electronics and processing. AES is also quantitative through either first principle calculations, published data bases, or the use of reference samples.

AUGER PROCESS

In AES, a beam of electrons bombarding a surface will result in back scattered primary electrons and emitted secondary electrons (Figure A2.1). Their energy will vary from low levels up to that of the primary beam (elastic scattered electrons). All below the primary energy are emissions resulting from ionization loss, diffraction, etc. Between the low energy and back scattered electrons, and in amongst the background spectrum, are emissions due to the Auger process. An electron energy (velocity) analyzer provides an energy spectrum or a measure of electron emission intensity versus energy.

For an atom at its ground state there are several electron shells with different binding energies. An incident electron may excite the atom by knocking out a core level

electron. For this process to take place, the incident electron has to have an energy greater than that of the binding energy. The atom will relax by filling the core level with an electron from an outer shell. In this transition, there is energy available that is equivalent to the energy difference between the two shells. This excess energy will either result in x-ray fluorescence or the emission of another electron from the same or shallower shell. The latter is an Auger electron.

The Auger transition involves three binding energies: the core level excitation, the relaxation level, and the level of the emitted electron. Figure A2.2 depicts a KL_1L_2 transition. An incident electron knocks out an electron in the K shell and relaxation takes place when an L_1 electron drops down to the K level, making energy available (E_K - E_{L1}). As the figure represents, the excess energy then causes the emission of an electron from the L_2 shell. The energy of the Auger electron is E_K - E_{L1} - E_{L2}. Other transitions are possible and include KLM, LMM, MNN, etc. Thus AES is capable of detecting elements where there are more than two electron energy levels, above helium in the periodic table.

Figure A2.3 is a surface Auger spectrum of a copper on nickel thin film structure. There is a series of weak signals (small bumps) on top of a large background. The latter is a constant slope that represents elastic and inelastic scattered electrons. Differentiation of this spectrum will emphasize the small features and diminish the background. Figure A2.4 is the differential spectrum of the same copper nickel sample. Clearly visible are the surface carbon and oxygen peaks as well as a series of peaks from copper; nickel does not appear because it is not present at the surface of this specimen.

The interaction depth of the incident electrons, and the region of core level ejection, is approximately 1 μm [A2.1]. However, the mean free path of electrons in materials is very short. Auger electrons lose energy through core excitation processes, plasmon losses, and inter band transitions [A2.2]. Therefore, it is only possible to detect Auger electrons emitted from just below the surface. The actual escape depth is matrix dependent but empirical studies [A2.2] show that it is normally less than 30 Å.

The surface sensitivity arises from the shallow escape depth of Auger electrons. Therefore, the condition of the surface is of great importance to achieve good results. To minimize the impact of varying surface conditions, it is necessary to take measurements in an ultra high vacuum (UHV) environment. That is, under conditions with minimum surface accumulation of atoms or molecules from the gas phase. Spectrometers need to possess the technology to achieve UHV and operation must follow appropriate practices to maintain the vacuum at such a level.

Quantification is possible because the intensity of an Auger emission is proportional to the relative concentration of that element. Equation A2.1 is a simple illustration where C is the element concentration, I_m is the intensity measurement of an element, and I_o is the measurement of the pure element. The intensity is the signal from Auger emissions at a transition energy (energy spectrum). I_o is the sensitivity factor. The physical processes that contribute to the intensity measurement are the ionization cross section, the depth below the surface of the transition, and the electron detector efficiency.

$$C = \frac{I_m}{I_o} \qquad (A2.1)$$

Sensitivity factors depend on the analyzer resolution and the differentiating algorithm [A1.1]. Therefore, it is important, when using published values, that conditions are at least similar. In practice, it is not often that quantification makes use of first principle calculations. Such a process requires an understanding of electron scattering and ionization cross-sections. Instead, it is simpler to take measurements on reference samples to determine the sensitivity factor values. The advantage of this practice is the experiment conditions are the same for the reference and unknown samples. There is no need to rely on sensitivity factors from measurement systems with a different resolution or modulation algorithm.

APPLICATIONS OF AES

AES is suitable for surface studies and, with accurate sample staging, it is possible to take spatial measurements of compositions over small areas. In one application, an AES experiment can determine the surface arrival time of an element from a buried film. Ex-situ annealing is possible but in-situ heat treatment provides better control of the surface condition.

For thin films, measurement of elemental distribution in the thickness direction makes AES an excellent tool for studying diffusion. To obtain a depth profile, it is necessary to remove material from the surface. The measurements take place either

consecutively or concurrently with erosion. Argon ion sputtering is a common method for removing material. To reduce the measurement time for depth profiles, it is easier to collect data within several short energy windows. There must be an energy window for each element of interest. The selection of the energy range depends on the primary beam and the elements of interest. For a 3 KeV primary beam the largest copper signal occurs near 920 eV; there are tables for transition energies of most elements.

The data for each element window, in counts versus energy, again requires differentiation. To convert to atomic concentration it is necessary to multiply the peak-to-peak height of the differential by a sensitivity factor; empirical determinations of sensitivity factor values are through measurements of reference samples.

LIMITATIONS OF AES

The sputter removal rate in depth profiling depends on a number of factors that include surface roughness, film density or composition, and ion beam density. Definitely the first two factors are difficult to control particularly for inhomogeneous structures that occur in diffusion studies. Limits on the areal density of the ion beam are mostly hardware dependent such that reproducibility is difficult over long periods. These circumstances put limits on measuring the true sputter depth.

The easiest way to circumvent this problem is to partially ignore the depth dimension and measure the build up of material within the film layer instead. This applies well to studies of low temperature diffusion. In such an experiment, the amount of mass

transport is a function of grain boundary diffusion and possible diffusion from the boundaries into the grain. The behavior of accumulation within a thin film, away from discontinuities, will provide an insight into possible diffusion mechanisms.

Since the AES differential peak has a finite width, a transition from one element may over lap with another element. This applies to transitions with similar energies or for a system with poor resolution. For a copper nickel couple, the lower transition energies of copper are very close to the transitions for nickel. The most abundant transition for nickel occurs near 848 eV; there are also copper transitions at 840 eV and 849 eV. Therefore, when both copper and nickel are present in the film, the nickel intensity is a sum of signals from both copper and nickel.

Subtracting the copper contribution will eliminate the signal over lap. The method to accomplish takes the intensity ratio of copper at uncorrupted transition energies to copper at over lap energies. The measurement is from material where only copper is present. The ratio is for copper in the nickel energy window to copper in its own window. It is preferable to calculate the ratio from the measurement data (integral curve) rather than from the differentiated data. This also requires the subtraction of a background signal that is equivalent to the detection of elastic scattering only. The signal at one copper transition is a proportional to all the other copper transitions. The ratio then permits calculation of the copper contribution to the nickel intensity because all transitions are proportional to the element concentration.

REFERENCES

A2.1 D. Briggs and M.P. Seah, Practical Surface Analysis, 2nd. Ed., Vol. 1: Auger and X-Ray Photoelectron Spectroscopy, John Wiley and Sons. 1990, pp. 5.

A2.2 A. Joshi, et al., "Auger Electron Spectroscopy" in Methods of Surface Analysis, Vol. 1: Method and Phenomena, Their Applications in Science and Technology, Edited by A.W. Czanderna, Elsevier Press, 1975

FIGURES

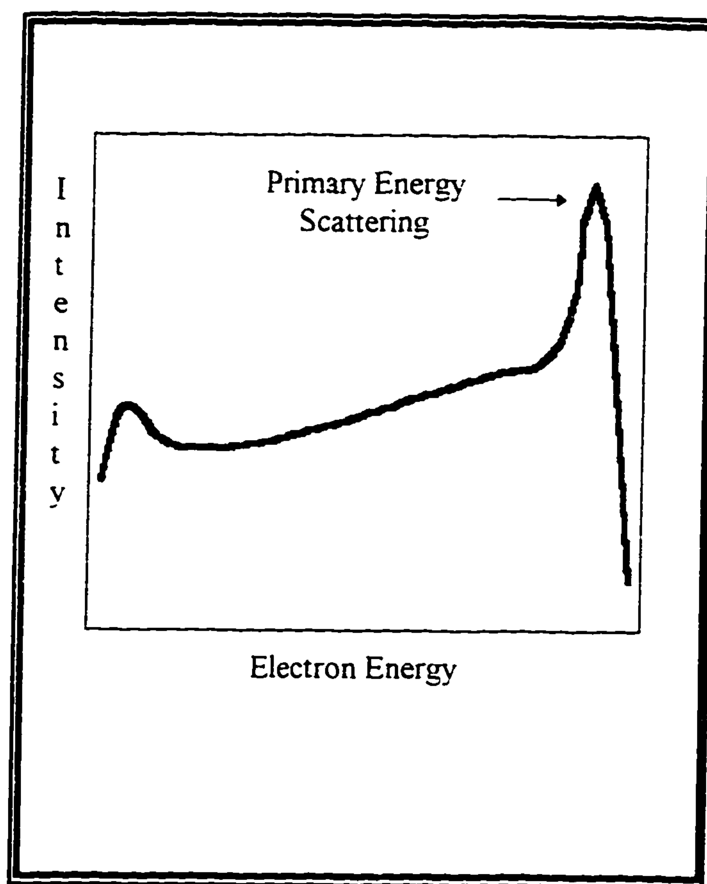

Figure A2.1 Energy Distribution of Primary and Secondary Electron Scattering.

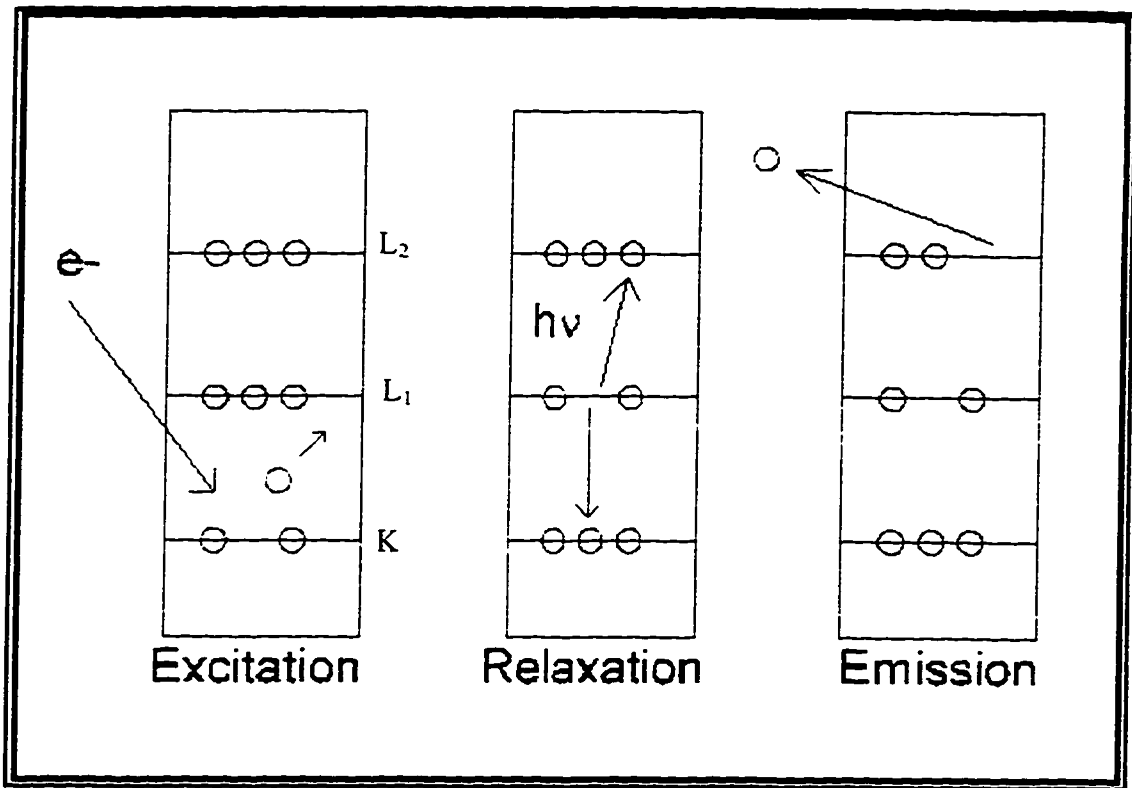

Figure A2.2 Electron Shell Transitions

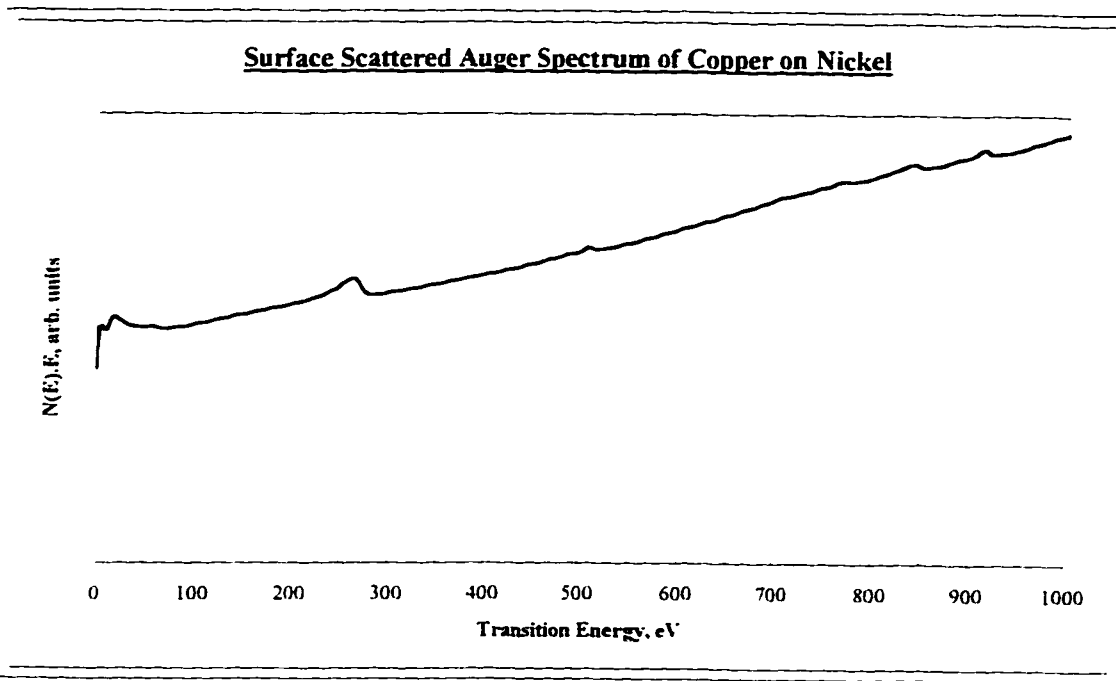

Figure A2.3 Surface Scattered Auger Spectrum of Copper on Nickel

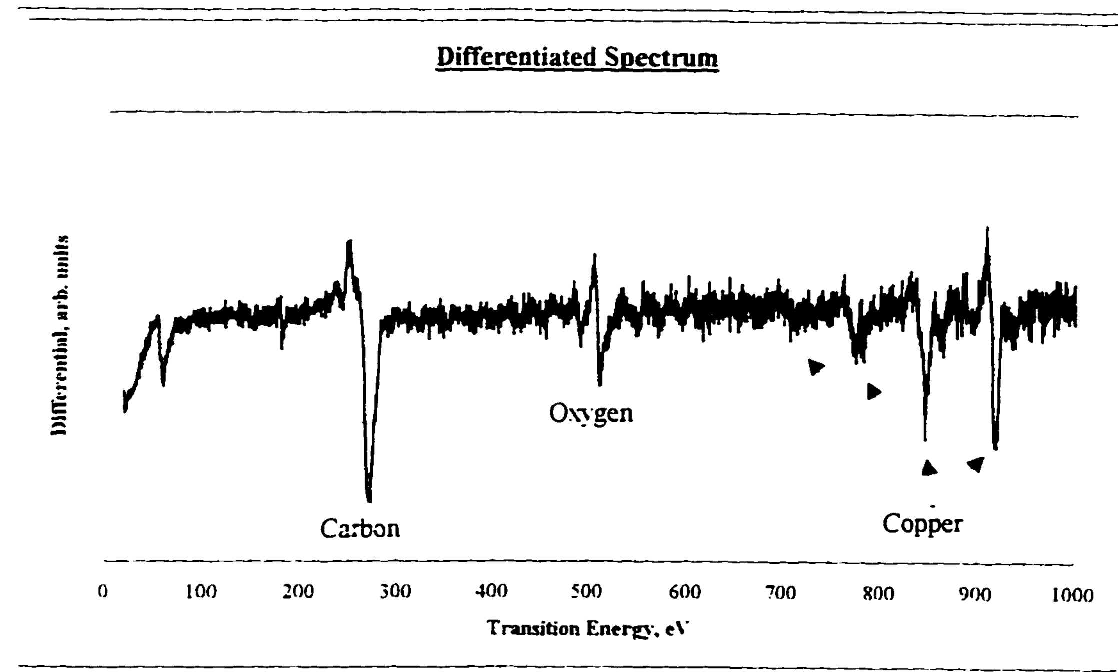

Figure A2.4: Differentiated Spectrum of Figure A2.3

APPENDIX III: X-RAY DIFFRACTION

INTRODUCTION

Constructive interference occurs when an x-ray beam attains the Bragg condition with a crystal [A3.1]. In materials that are single crystals or polycrystalline, diffraction will manifest itself as peaks against a background signal of destructive interference. The peaks and their widths provide information about the crystal structure of the material. There are specific conditions for diffraction to occur with a given crystal structure and lattice parameter.

It is possible to use x-ray diffraction (XRD) to determine a variety of different structure characteristics of materials and thin films. For example, simple diffraction patterns will provide information about the phases present in a material. Using specific measurement conditions, it is also possible to use XRD for chemical analysis, texture determination, and stress measurements.

DIFFRACTION PROCESS

$$n \cdot \lambda = 2 \cdot d \cdot \sin(\theta) \qquad \text{(A3.1)}$$

The equation above is the classical Bragg condition. When a mono-energetic beam of wavelength λ impinges on a crystal with lattice spacing d, constructive interference will take place at the Bragg angle, θ. In Equation A3.1, n represents the diffraction order of different planes. Figure A3.1 illustrates the path difference (AB + BC) for rays scattered by different crystal planes. At the Bragg condition, the path difference results in scattered

rays that are in phase with each other and thus are reinforcing. At other scattering angles, the rays are out of phase and result in partial or complete destructive interference. The composition of a diffracted beam is a large number of x-rays that reinforce each other.

$$\frac{1}{d^2} = \frac{\left(h^2 + k^2 + l^2\right)}{a^2} \qquad \text{(A3.2)}$$

$$\sin^2(\theta) = \frac{\lambda^2}{4 \cdot a^2}\left(h^2 + k^2 + l^2\right) \qquad \text{(A3.3)}$$

For cubic crystals, Equation A3.2 is the relation of the lattice spacing d, to the plane indices (hkl) and the lattice parameter, a. Equation A3.3 is a combination of Equations A3.1 and A3.2, illustrating the diffraction angles for a specific plane (hkl) in a material of lattice parameter, a. Similar equations apply for other crystal systems (hexagonal, tetragonal)

Different diffraction methods use either a fixed or variable x-ray wavelength and a fixed or variable scattering angle. For a normal coupled scan, the wavelength is fixed and the scattering angle varies at twice the incident angle. A detector (scintillation or proportional counter) measures the intensity of x-rays at the scattering angle.

Energetic electrons, decelerated by a target material (for example, copper), produce the monochromatic radiation. The radiation emission is a result of bombarding electrons that knock out inner shell electrons. The excited atom relaxes when an electron from an outer shell drops into the vacant site of a lower energy shell. The radiation wavelength is inversely proportional to the difference in energy of the two shells. For a

copper target, it is normal to use the characteristic radiation line K_α. This line is the result of an electron dropping down from the L to the K shell. The characteristic line only appears when the electron energy is high enough to initially excite the copper atom. The decelerating electrons create the background, or Bremsstrahlung, radiation.

APPLICATION OF XRD

There are many arrangements and applications for x-ray diffraction. Therefore, the discussion here will focus on using the technique to determine grain size within thin films. Figure A3.2 is an example diffraction pattern for a copper nickel thin film structure.

Complete destructive interference in x-ray diffraction occurs in the ideal case for a crystal of infinite size. For a scatter angle that does not produce a path length that is an exact integral of the wavelength, destructive interference is not complete. If the planar spacing is such that the path length difference is a fraction of the wavelength then complete interference will require either a second, third, or deeper plane. Therefore, scattering angles that are near the Bragg condition need deep planes to provide complete destructive interference. If the crystal has a finite size the plane may not appear. Thus, small crystals cause a broadening in the diffraction peak near the Bragg angle. An exact analysis of broadening produces the Scherrer formula (Equation A3.4) that relates particle size (L) to full width at half maximum (W) of the diffraction peak.

$$L = \frac{0.86 \cdot \lambda}{\sin(\theta) \cdot W} \qquad \text{(A3.4)}$$

LIMITATIONS OF XRD

In practical x-ray diffraction, the incident x-rays are neither perfectly monochromatic nor parallel. The x-ray beam is part of the continuous brehmsstralung radiation and contains both convergent and divergent rays. Both of these factors lead to broadening of the diffraction peak; diffraction will occur at angles that do not satisfy the Bragg condition.

Inhomogeneous strain may occur with lattice diffusion due to the differences in atomic size and/or lattice parameter. When a small or larger atom occupies a site within the lattice of another element it can create a strain field. The strain will vary spatially if the atomic concentration of the impurity atom also varies. This situation is likely to occur with diffusion from interfaces and grain boundaries. Re-writing the Bragg condition (Equation A3.5) illustrates how a change in the lattice spacing (Δd) will affect the diffraction angle (Equation A3.6).

$$\sin(\theta) = \frac{n \cdot \lambda}{2 \cdot d} \qquad \text{(A3.5)}$$

$$\Delta[\sin(\theta)] = \frac{1}{\Delta d} \cdot \left(\frac{n \cdot \lambda}{2}\right) \qquad \text{(A3.6)}$$

REFERENCES

A3.1 B.D. Cullity, Introduction to Magnetic Materials, © 1972 Addison-Wesley, p. 113

FIGURES

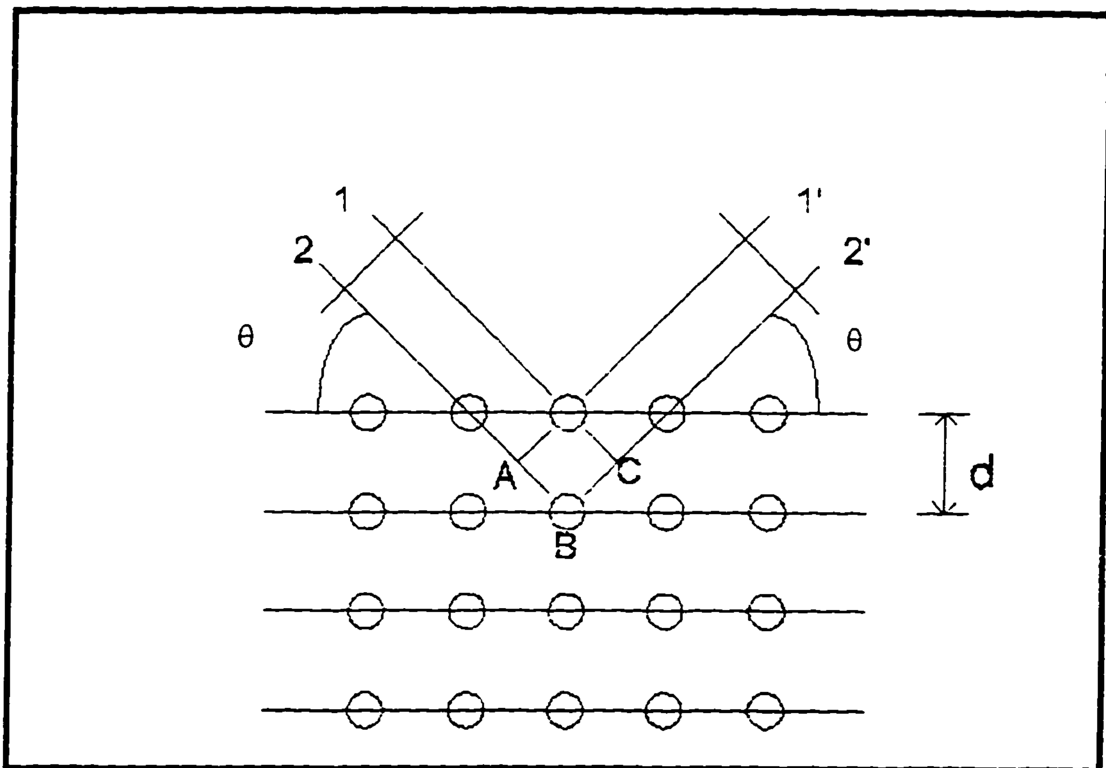

Figure A3.1 X-Ray Diffraction by a Crystal.

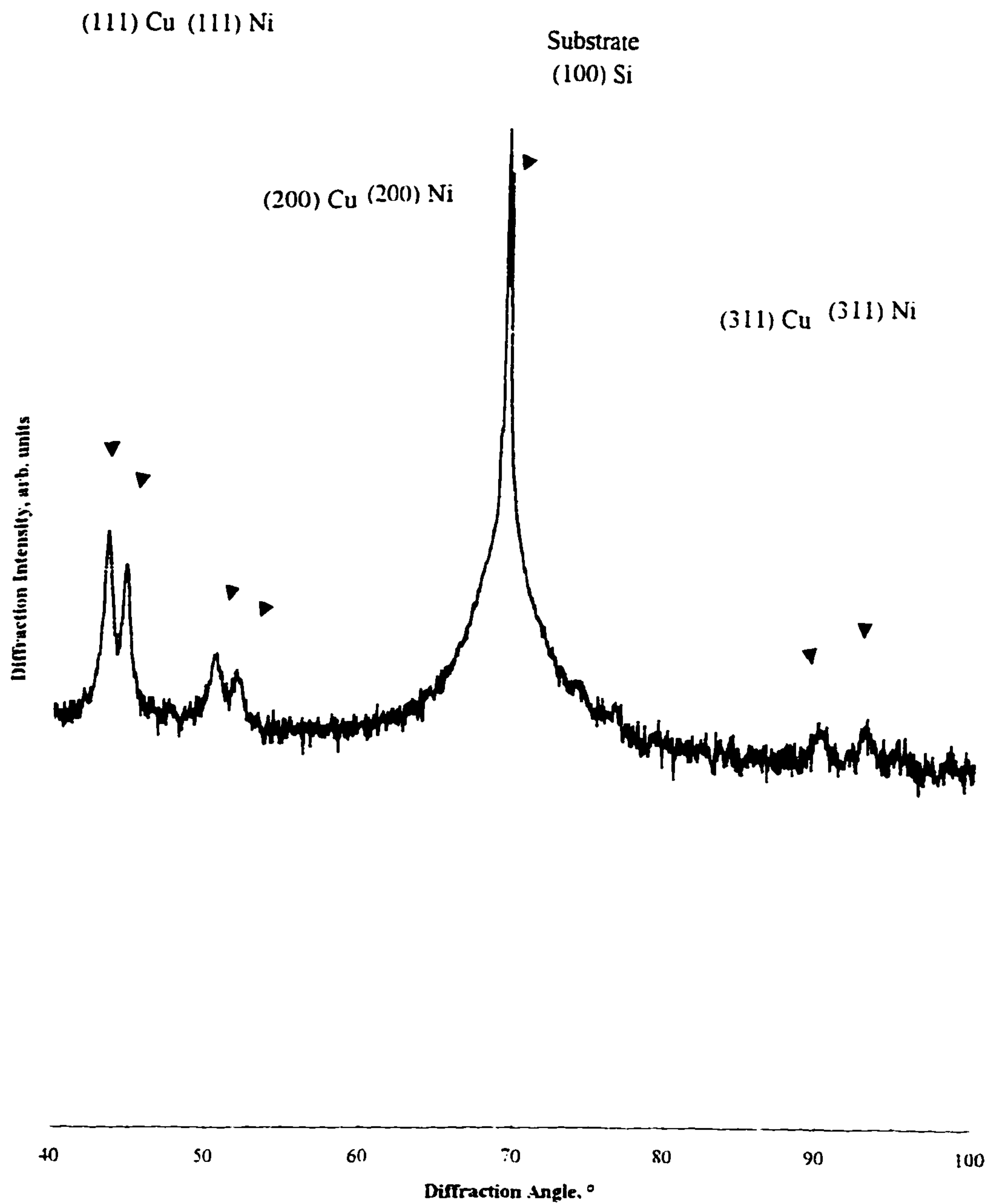

Figure A3.2 X-Ray Diffraction Pattern for a Copper Nickel Thin Film Structure